Neutron-proton elastic scattering spin-spin correlation parameter measurements between 500 and 800 MeV. I. C_{SL} and C_{LL} at backward c.m. angles

W. R. Ditzler,[a] D. Hill, J. Hoftiezer,[b] K. F. Johnson,[c] D. Lopiano, T. Shima,[d]
H. Shimizu,[e] H. Spinka, R. Stanek, D. Underwood, R. G. Wagner, and A. Yokosawa
High Energy Physics Division, Argonne National Laboratory, Argonne, Illinois 60439

G. R. Burleson, J. A. Faucett,[f] C. A. Fontenla,[g] R. W. Garnett,[c] C. Luchini,[h] and M. W. Rawool-Sullivan
New Mexico State University, Las Cruces, New Mexico 88003

T. S. Bhatia,[i] G. Glass, J. C. Hiebert, R. A. Kenefick, S. Nath,[c] and L. C. Northcliffe
Texas A&M University, College Station, Texas 77843

R. Damjanovich, J. J. Jarmer, and J. Vaninetti
Los Alamos National Laboratory, Los Alamos, New Mexico 87545

R. H. Jeppesen
University of Montana, Missoula, Montana 59812

G. E. Tripard
Washington State University, Pullman, Washington 99164
(Received 25 March 1992)

Final results are presented for the spin-spin correlation parameters C_{SL} and C_{LL} for *np* elastic scattering with a polarized neutron beam incident on a polarized proton target. The beam kinetic energies are 484, 634, and 788 MeV, and the c.m. angular range is 80°–180°. These data will contribute significantly to the determination of the isospin-0 amplitudes in the energy range from 500 to 800 MeV.

PACS number(s): 13.75.Cs, 13.88.+e, 14.20.Pt, 21.30.+y

I. INTRODUCTION

Nucleon-nucleon (*NN*) elastic-scattering spin measurements at intermediate energies (up to $T_{\rm lab} \sim 1$ GeV) have been performed for many years at a number of laboratories. A complete determination of the elastic-scattering amplitudes (five isospin-1 or $I=1$ and five isospin-0) requires a large number of different spin-parameter measurements at each angle and energy. While the five $I=1$ nucleon-nucleon amplitudes are now reasonably well determined over most of this energy range, the $I=0$ amplitudes are poorly known above about 500 MeV [1–6].

Some of the reasons for this difference are related to experimental difficulties in measuring *np* elastic scattering compared with *pp* scattering. Polarized proton targets and carbon polarimeters to measure the spin of the outgoing protons are available for both *pp* and *np* experiments. However, the detection of beam neutrons or scattered neutrons is more difficult than that for protons. Also, whereas nearly monoenergetic polarized proton beams of high intensity are available at intermediate energies, free neutron beams typically contain a broad spectrum of energies and the intensity of polarized neutron beams is usually low. The consequence is that *pp* elastic-scattering spin observables have been measured over a wide range of angles and energies to good statistical precision. By comparison, the number and variety of spin data for *np* elastic scattering is significantly less, and the precision is usually worse as well.

Another reason that the $I=0$ amplitudes are poorly determined is that *pp* and *nn* scattering are pure $I=1$ channels, whereas the *np* scattering amplitudes are mixtures of $I=0$ and 1 channels:

$$\mathrm{Amp}(np,\theta,T_{\rm lab}) = \tfrac{1}{2}[\mathrm{Amp}(I=0,\theta,T_{\rm lab}) + \mathrm{Amp}(I=1,\theta,T_{\rm lab})] \ .$$

[a]Present address: Naval Weapons Center, China Lake, CA 93555.
[b]Present address: LeCroy Corporation, 700 Chestnut Ridge Road, Chestnut Ridge, NY 10977.
[c]Present address: AT Divison, Los Alamos National Laboratory, Los Alamos, NM 87545.
[d]Present address: Department of Physics, Texas A&M University, College Station, TX 77843.
[e]Present address: Department of Physics, Yamagata University, 1-4-12 Kojirakawa, Yamagata 990, Japan.
[f]Present address: MP Division, Los Alamos National Laboratory, Los Alamos, NM 87545.
[g]Present address: Engineering Business International, P.O. Box 651, Lenox Hill Station, New York, NY 10021.
[h]Present address: Physics Department, University of Illinois, Urbana, IL 61801.
[i]Present address: ER-224, GTN, U.S. Department of Energy, Washingon, D.C. 20585.

The factor of $\frac{1}{2}$ in the equation above suggests that the $I=0$ amplitudes will generally be more poorly determined from *np* scattering than the $I=1$ amplitudes from *pp* scattering, assuming that the *pp* and *np* spin observables are measured to the same accuracy.

Nucleon-nucleon interactions make an impact on a wide variety of topics in nuclear and particle physics, such as understanding the nuclear force, nucleon and electron scattering from nuclei, and the allowable quark configurations, for example, qqq, $q\bar{q}$, or $6q$ states. These three reasons are the principal motivations for studies of nucleon-nucleon elastic scattering and total-cross-section spin observables.

An important reason for experimental studies of the $I=0$ nucleon-nucleon channel is that *np* elastic scattering is one of the most basic reactions involving the strong interaction. The *NN* reactions are particularly important for the study of spin effects of the nucleon constituents, since such spin effects are somewhat masked in meson-nucleon amplitudes by the zero spin of both the pion and kaon. In the intermediate-energy region, the onset of *NN* inelastic reactions complicates the interpretation of the amplitudes, but at the same time provides the opportunity to compare threshold behavior in both the $I=0$ and 1 channels.

The inelastic channels for the two isospins are considerably different at intermediate energies. For $I=1$, the $NN\rightarrow d\pi$ and $NN\rightarrow NN\pi$ reactions have sizable cross sections at bombarding energies above 400 MeV. The $N\Delta(1232)$ channel dominates the $NN\rightarrow NN\pi$ reaction from about 500 to 1300 MeV [7], peaking at approximately 16 mb. Delta states with mass above 1232 MeV can also contribute to the $I=1$ inelastic cross section via $NN\rightarrow N\Delta$ reactions. On the other hand, neither $NN\rightarrow d\pi$ nor $NN\rightarrow N\Delta$ can contribute to $I=0$ because of isospin conservation. Furthermore, the $I=0$ total inelastic cross section, though poorly known, seems consistent with zero up to approximately 1000 MeV [8,9], where it increases to about 2–7 mb. Therefore it should be quite instructive to compare the behavior of the *NN* $I=0$ and 1 amplitudes from below 500 MeV, where both inelastic cross sections are small, up to 800 MeV, where the $I=1$ inelastic cross section is large and dominated by the $NN\rightarrow N\Delta$ channel and, also, where the $I=0$ inelastic cross section is small.

Over the past several decades, the nucleon-nucleon amplitudes and phase shifts have proven to be a stringent test of theoretical models describing the strong nuclear force at intermediate energies. These models have led to a better understanding of the strong interaction at intermediate energies. One of the most successful of models has been the meson-exchange model. The long-range part of the strong interaction was shown to be due to one-pion exchange [10,11], by comparing the model predictions with *NN* phase shifts. After mesons heavier than the pion were discovered, these mesons and correlated particle exchange, such as that from two pions, were incorporated into theoretical calculations [12–19]. This addition was quite effective in reproducing the intermediate-range attraction of the *NN* interaction. Dispersion relations [20–24] that properly address two- and multiple-pion exchange were included in the model and compared well with the data from the *NN* phase shifts. A very large theoretical effort has led to the development of the Paris [25], Bonn [26], and Argonne [27] potentials or models. These potentials fit the *NN* phase-shift data quite well to energies above the pion-production threshold. Meson-exchange models have been successfully applied to both nucleon-nucleon elastic scattering and pion production; for example, see Refs. [28–36].

A second theoretical approach in understanding the strong nuclear force is the Skyrme model of pions and nucleons (see, for example, Refs. [37–49]). This model has been developed to understand the structure of nucleons and then has been applied to low-energy nucleon-nucleon interactions. A connection occurs between the Skyrmion topological current and the fermion and quark effects found in QCD. Recently, calculations have demonstrated [38,40,45,47,48] the intermediate-range attraction between nucleons in this model that was not seen earlier.

Considerable theoretical effort is presently being devoted to understanding the nuclear force in terms of the quark model and QCD. Once again, the nucleon-nucleon scattering amplitudes and phase shifts provide the critical tests for quark-model calculations. A number of different approaches [50–71] have been applied to the *NN* interaction, including bag models, cloudy bag models, models with one-gluon exchange between quarks or quarks and pions, and models with the addition of virtual quark-antiquark pairs in nucleon wave functions. Frequently, these models concentrate on calculating the short-range *NN* interaction at low energies, using meson exchange for the intermediate- and long-range parts of the interaction. Substantial progress has been made in this field, and further improvements are anticipated in the future. A review of this research is presented in Ref. [72].

A second motivation for $I=0$ nucleon-nucleon studies is to assist in the interpretation of both nucleon-nucleus scattering phenomena and the expected results from the Continuous Electron Beam Accelerator Facility (CEBAF) on electron-nucleus scattering.

The study of nucleon-nucleon interactions is very important in calculating the scattering of nucleons from nuclei. At present, these calculations either directly use the free *NN* amplitudes or use the results from theoretical models, fit to the *NN* amplitudes, to choose constants for effective *NN* amplitudes in nuclei. In the future the goal will be to understand nucleon scattering from nuclei in terms of quark and gluon interactions. The free *NN* amplitudes are again expected to provide a stringent test for these calculations.

Nonrelativistic models were first used to describe nuclear structure and proton-nucleus scattering using the Paris or other *NN* potentials as a starting point. However, the motion of a nucleon in the average or mean field of a nucleus is primarily affected by an attractive scalar and a repulsive vector potential. The magnitudes of these potentials in the nucleus are sizable compared with the nucleon mass, which indicates that relativistic calculations are needed. For example, relativistic Dirac-Hartree mod-

els [73–77] were able to reproduce the spin-orbit splittings between nuclear excited states. These splittings are essential to the nuclear shell model and arise from the scalar and vector *NN* potentials and the relativistic Thomas spin-orbit interaction. The approximately constant central density and the binding energy per nucleon in nuclei (the saturation of the nuclear force) is derived from the *NN* potentials in both the Dirac-Hartree and relativistic Brueckner-Hartree-Fock models [78–80].

In the early 1980s, calculations using a relativistic impulse approximation and the Dirac phenomenology [81,82] were successful in describing proton-nucleus scattering spin observables [83–90], whereas the nonrelativistic models [91–93] had failed to do so. A generalized relativistic impulse approximation [94,95] has also been developed to describe spin observables. Both potentials used in the proton-nucleus scattering calculations are based on the free *NN* amplitudes. A progress report through 1986 on the relativistic mean-field models of the types described above is summarized in Ref. [96]. More recent work has focused on connecting the nonrelativistic and relativistic approaches [97–99] to nucleon-nucleus scattering and on relating the *NN* amplitudes and the potentials used for the scattering calculations [100–102].

In the case of proton scattering from light nuclei, and in particular deuterium, the Glauber multiple-scattering theory [91] has been used for calculations of spin observables [103–111] as well as cross sections. The free nucleon-nucleon amplitudes are also used as inputs for these calculations, and in some cases, the results also are used to constrain the *NN* amplitudes.

The high-intensity electron beam from the CEBAF accelerator will provide the capability for many new nuclear-physics measurements [112]. The higher electron energy, compared with existing electron accelerators such as Bates, will extend the kinematic range for scattering experiments, and the high duty factor and intensity will allow many coincidence measurements that are presently not feasible. Over a large portion of the allowed kinematic range, a knowledge of the *NN* amplitudes will be necessary to interpret the results from some electron-scattering measurements, especially the $(e,e'NN)$ reaction. This also illustrates the well-known complementarity of electron and nucleon scattering in studying nuclear structure.

The third motivation for $I=0$ nucleon-nucleon spin measurements concerns the energy-dependent structures seen in various spin observables at energies up to 1 GeV, from which there has been considerable controversy concerning the interpretation of the resonancelike behavior of the $^1D_2$ and $^3F_3$ partial waves seen in phase-shift analyses [1–4,113–116]. The suggestion of possible dibaryons in the $^1D_2$ and $^3F_3$ partial waves was triggered by early measurements at the ANL Zero Gradient Synchrotron (ZGS) of the total-cross-section difference between antiparallel and parallel longitudinal spin states, $\Delta\sigma_L(pp)$ [117–119]. The peaks near 600 MeV in $\Delta\sigma_L(pp)$ and $\Delta\sigma_T(pp)$ have been confirmed by phase-shift analyses to originate from the resonancelike behavior of the $^1D_2$ partial wave and the dip in $\Delta\sigma_L(pp)$ near 800 MeV from the $^3F_3$ partial wave. Initially, the ZGS $\Delta\sigma_L(pp)$ results were claimed to be in error [120,121], but they were subsequently confirmed at other laboratories [122–124]. Furthermore, structure in $\Delta\sigma_L(pp)$ had been suggested *before* the ZGS measurement on the basis of a Saclay phase-shift analysis [125].

The interpretation of the resonancelike behavior of the $^1D_2$ and $^3F_3$ partial waves, and possibly a similar behavior in the $^3P_2$ wave, has been disputed for over 12 years. One side of the dispute, claims that dibaryon resonances or six-quark states cause the observed partial-wave behavior. The other side interprets this behavior as threshold effects due to the opening of the $NN \rightarrow N\Delta(1232)$ channel. It should be noted that the $^1D_2$ and $^3F_3$ *NN* waves feed the *S*- and *P*-state $N\Delta$ waves, respectively, and that the phase-shift solutions indicate large inelasticities for these two *NN* waves. Thus it is plausible that threshold effects could cause this observed behavior.

A large number of authors have contributed arguments on both sides of this controversy. Recently, measurements of a number of spin observables in the $pp \rightarrow pn\pi^+$ reaction at the ZGS, TRIUMF, and LAMPF have permitted a partial-wave analysis of the data under a number of assumptions and approximations [126–128]. One of the main points of these papers was that a coupled-channel approach including both *NN* and $N\Delta$ was necessary; resonancelike behavior should be apparent in the $N\Delta$ phase if a dibaryon was present. The authors of Ref. [128] asserted that the $^1D_2$ (and probably the $^3F_3$) inelastic phase did not exhibit the expected changes indicating a dibaryon. These conclusions, which differ sharply with analyses of the world's *pp* scattering data [1,2,129–137], have been challenged by several other authors [138–142] on issues relating to the assumptions that were used in Ref. [128]. Since only 6 of the 31 spin observables necessary for a model-independent analysis were used to perform the partial-wave analysis in Ref. [128], there is a possibility that there are other solutions with a different behavior of the partial waves [139]. Furthermore, the consequences of the reported partial-wave solution in Ref. [128] were evaluated independently by Hoshizaki [138] and Hiroshige *et al.* [141]. It was shown that the data in Ref. [128] are consistent *with* the presence of a dibaryon. In Ref. [138] it is claimed that a coupled three-channel analysis should be used with *NN*, $N\Delta$, and nonresonant $NN\pi$ channels. A similar coupled three-channel analysis [141] was performed using the *NN*, $N\Delta$, and πd channels. This dibaryon controversy is clearly a difficult problem and may take some time before a consensus is reached.

Some evidence of structure in the $I=0$ nucleon-nucleon channel is also observed, as well as in $I=1$ interactions. The quantity $\Delta\sigma_L(I=0)$, derived from recent $\Delta\sigma_L(np)$ measurements at LAMPF [143], Saclay [144], and PSI, [145] exhibits a peak near 650 MeV. An analysis of the total-cross-section measurements $(\sigma_{\rm tot},\sigma_{\rm inelastic},\Delta\sigma_L,\Delta\sigma_T)$ for the $I=0$ channel and the *np* differential cross-section data at 180° by Beddo *et al.* [143] suggests that the observed structure in $\Delta\sigma_L(I=0)$ may be caused by a spin-triplet wave, such as $^3S_1$ or $^3D_1$, or a spin-singlet wave, such as $^1P_1$ or $^1F_3$. Data on *np*

elastic-scattering spin observables in the LAMPF energy range will be required to identify uniquely the partial wave(s) producing the observed behavior of $\Delta\sigma_L$ ($I=0$). (There have also been suggestions of $I=0$ dibaryon resonances at somewhat higher energies from the $\gamma d \rightarrow pn$ reaction [146–148].)

It is interesting to note that the shape of $\Delta\sigma_L(pp)$, which some physicists have claimed to be caused primarily by the opening of the inelastic channels with a value of $\sigma_{\text{inelastic}} \approx 20$mb, is nearly identical to that for $\Delta\sigma_L$ ($I=0$), where the inelastic cross section is at most a few mb. In particular, displacing a curve through $\Delta\sigma_L(pp)$ upward by about 12 mb and to higher energies by approximately 140 MeV gives a reasonably good fit to the $\Delta\sigma_L(I=0)$ measurements at PSI, LAMPF, and SATURNE. Thus structure in $\Delta\sigma_L$ at the 10-mb level is seen with a small total inelastic cross section.

Although the interpretation of the resonancelike behavior of the $^1D_2$ and $^3F_3$ partial waves in terms of six-quark states is by no means universally accepted, the existence of six-quark states would have a profound impact on the understanding of nuclear structure. For example, some fraction of the deuteron ground state might be in a six-quark configuration, rather than a loosely bound state of two separate nucleons. In other nuclei, six-quark clusters would presumably be present as well. The existence or lack of existence of six-quark states also affects the fundamental understanding of the strong interaction. At present, three-quark and quark-antiquark states seem sufficient to describe all hadrons. The existence of six-quark states would add a third possible configuration and would probably strengthen the evidence for the presence of still other configurations.

The existing free *np* elastic-scattering database between 400 and 900 MeV consists of many differential cross-section [149–162] and polarization [163–170] measurements, especially at backward c.m. angles. Unfortunately, sizable differences are seen for some of these results. Published data for other spin observables are much less plentiful, including depolarization and spin-transfer results [164–166,171], with carbon polarimeters to measure the outgoing proton spin, and some polarized-beam–polarized-target data from TRIUMF [169], SATURNE [172], and LAMPF [173,174]. A number of quasielastic-scattering experiments on deuterium have also been performed [175–195]. Finally, a high statistics set of *np* spin-transfer experiments at 485–788 MeV [196] have recently been completed at LAMPF using the new high-intensity optically pumped polarized ion source.

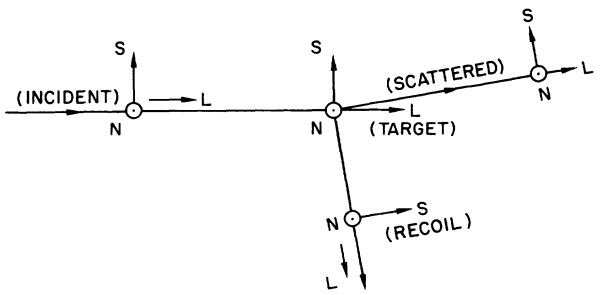

FIG. 1. Definition of spin directions for the beam, target, and forward-scattered and recoil particles for nucleon-nucleon elastic scattering.

This paper describes measurements of two spin-spin correlation parameters for free *np* elastic scattering at 484, 634, and 788 MeV beam kinetic energy. The spin directions are defined as **N** normal to the scattering plane, **L** (longitudinal) along the incident-beam direction, and $\mathbf{S}=\mathbf{N}\times\mathbf{L}$ (see Fig. 1). A polarized **S**- and **L**-type neutron beam was scattered from a polarized **L**-type target. The spin parameters measured were C_{SL} and C_{LL}, respectively, where

$$C_{ij}=\frac{d\sigma/d\Omega(++)+d\sigma/d\Omega(--)-d\sigma/d\Omega(+-)-d\sigma/d\Omega(-+)}{d\sigma/d\Omega(++)+d\sigma/d\Omega(--)+d\sigma/d\Omega(+-)+d\sigma/d\Omega(-+)} .$$

The first subscript i refers to the beam and the second to the target spin directions. The plus and minus refer to spins parallel or antiparallel to the L or S directions, respectively. For positive C_{SL} the neutron is preferentially scattered to the left for the $+S$ beam and $+L$ target spins, in accord with the Basel convention [197]. The recoil proton was detected in a magnetic spectrometer over the angular range $\theta_{\text{lab}} \approx 0°-25°$ or 21°–46°. Interference with the polarized-target magnet coils generally prevented detection of the scattered neutron in coincidence.

The experimental apparatus is described in Sec. II and the data analysis in Sec. III. The results, a comparison to phase-shift predictions, and a cross-check with other data at $\theta_{\text{c.m.}}=90°$ are presented in Sec. IV. Conclusions are given in Sec. V. Preliminary results from this experiment have been presented in a short paper [198]. These measurements were the basis of a Ph.D. thesis [199], where additional details may be found.

II. EXPERIMENTAL APPARATUS

A. Polarized neutron beam

These measurements were performed at the Clinton P. Anderson Meson Physics Facility at Los Alamos (LAMPF). Protons from the Lamb-shift polarized ion source were accelerated by the linac as H^- ions to nominal kinetic energies of 497, 647, and 800 MeV. The electrons were stripped off a fraction of the beam by passage through thin foils or wire mesh (see Fig. 2); these stripped polarized protons were utilized for experiments in line *C*

with the High Resolution Spectrometer (HRS). After additional bending, some of the remaining H^- beam was stripped and was used to produce the neutron beam in line *B*. The unstripped H^- beam went to a third experimental area, the external proton beam (EPB). The relative intensities in the three beam lines was determined by the beam location and size and by the types of strippers used.

The polarized protons in line *B* (after the second stripper LB-ST) passed through bending and steering magnets, a superconducting solenoid, a bending magnet, quadrupoles, the beam-line polarimeter, another bending magnet, and finally struck a liquid-deuterium (LD_2) target. Noninteracting protons were then deflected with dipole magnets and sent to a beam dump far from the LD_2 target. At the center of the 25-cm-long LD_2 target, the proton energies were computed to be 491±3, 641±3, and 795±4 MeV from the known material in the beam line. Errors on these energies are primarily from the uncertainty in the average incident-beam energy.

The neutrons were produced in the reactions $p+d \rightarrow n+p+p$ or $n+p+\pi+N$ at 0°. The first reac-

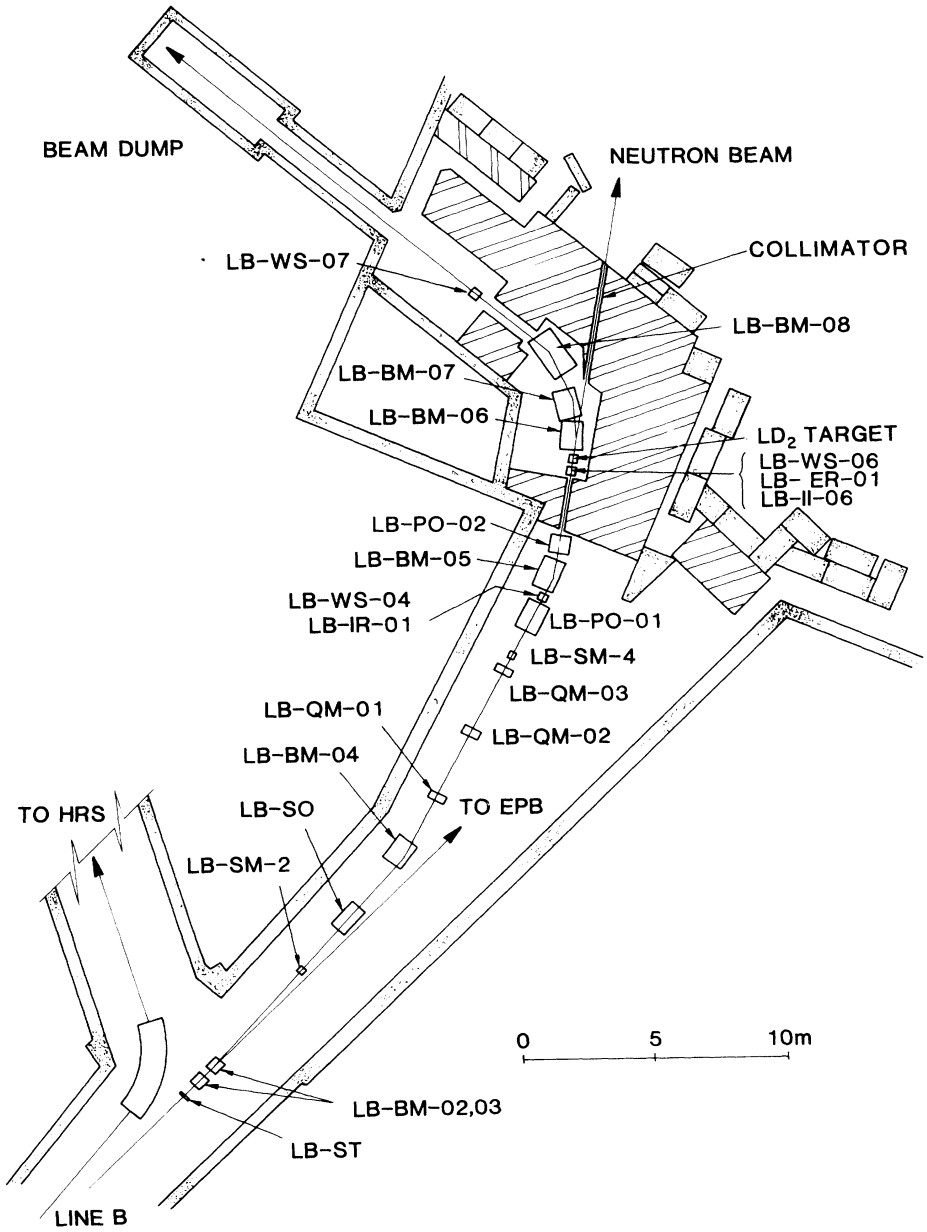

FIG. 2. Schematic view of the magnets and instrumentation in line *B* at LAMPF used in this experiment. H^- ions entered from the lower left. An electron stripper (LB-ST) gave H^- in EPB and stripped polarized protons in line *B*. Various dipole and quadrupole magnets (LB-BM-02 to -08; LB-QM-01 to -03, respectively) and steering magnets (LB-SM-2 and 4) are shown. The superconducting solenoid LB-SO and the SEM (LB-ER-01) are also given. The line-*B* polarimeter is designated LB-PO-01. The neutron beam is formed at 0° with respect to the incident proton beam.

tion gives a narrow peak in the neutron momentum spectrum near the incoming proton-beam momentum (the centroid of the peak was roughly $P_n = 1069 \pm 4$, 1262 ± 4, and 1450 ± 4 MeV/c or $T_n = 484 \pm 5$, 634 ± 5, and 788 ± 5 MeV). The second reaction produces a broad range of neutron energies, which was a source of background for this experiment. The measured neutron momentum spectra, taken under conditions similar to those in this experiment, are given in Refs. [200,201]. The average neutron-beam intensity was estimated to be a few thousand neutrons per second at the peak energy with a proton intensity of several nA.

In order to produce a beam of polarized neutrons, the incident proton beam had to be polarized, since a spin-transfer mechanism at 0° neutron production was used. The spin-transfer parameters for transversely and longitudinally polarized protons were measured in previous experiments [184,190] at the same energies used in this experiment. At these energies a longitudinally polarized proton beam with 80% polarization gives a neutron beam with 40–50 % (longitudinal) polarization, but a transversely polarized proton beam gives a neutron beam with much smaller polarization. As a consequence, the measurements reported in this paper were made when the polarized proton beam had a large longitudinal (L-type) spin component. When other beam polarizations existed, background measurements or tests of systematic errors were performed.

The beam-spin direction in line C was determined by the spin direction at the ion source and by the beam energy. Although the beam spin in the EPB could be adjusted to almost any direction, independent of the ion-source direction, the spins in lines B and C were partially coupled. Some flexibility was afforded by the superconducting solenoid in line B (LB-SO in Fig. 2) that could precess a transverse proton spin by up to 90° about the beam direction at 800 MeV. Thus, when the protons at the HRS target were purely $N(L,S)$ type, the proton beam at the LD_2 target could be nearly $L(S,L)$ type. Since the three spin directions were run for roughly equal times at the HRS target, (nearly) longitudinal beam could be achieved only about $\frac{2}{3}$ of the running time at the LD_2 target. The remainder of the time corresponded to a neutron beam with quite low polarization.

A standard LAMPF beam-line polarimeter [202–204] (LB-PO-01 in Fig. 2) was installed in line B to monitor the two transverse components of the beam polarization at that point. This polarimeter was continuously operational during data taking. The third beam-spin component was determined [203] using information on the total magnitude of the beam polarization from the "quenched" mode of operation of the polarized ion source. Normally, there was 107 sec of polarized beam, 5 sec of quenched beam, 107 sec of polarized beam with the spin direction reversed, and 5 sec of quenched beam. The cycle was then repeated. A full cycle took 240 sec, allowing for times to change from one condition to the next. (During some of the 788-MeV experimental runs, a more rapid spin-reversing cycle, without the quenched beam periods, was used; see Sec. II E). Note that the proton beam passed through a bending magnet between the polarimeter and LD_2 target. This caused a rotation in the horizontal component of the beam-spin direction by about 48°. Additional information on the beam spin was available from beam-line polarimeters located in line C and the EPB. The uncertainty of the proton-spin direction at the LD_2 target is estimated to be roughly ±1° and that of the beam polarization to be about ±2% of its magnitude on the average [205]. Table I contains the average proton-beam polarization for each set of measurements.

After the LD_2 target, the neutrons passed through the field of magnets LB-BM-06 and LB-BM-07 that deflected the noninteracting beam into the beam dump and swept charged reaction products away from the 0° line used for the neutron beam. This caused the neutron-spin direc-

TABLE I. Average proton- and neutron-beam polarizations $\langle P_{B,p} \rangle$ and $\langle P_{B,n} \rangle$ and the average target polarization $\langle P_T \rangle$. The neutron-beam kinetic energy is T_n, and the laboratory spectrometer angle is θ_{sp}. Also included are the number of polarized and background runs and the number of target reversals.

T_n	θ_{sp}	Parameter	$\langle P_{B,p} \rangle$	$\langle P_{B,n} \rangle$	$\langle P_T \rangle$	Polarized runs	Target reversals	Background
484 MeV	10°	C_{LL}	0.794	0.396	0.763	20	4	16
	10°	C_{SL}	0.786	0.392	0.760	13	3	
	35°	C_{LL}	0.810	0.404	0.765	27	5	27
	35°	C_{SL}	0.845	0.388	0.760	31	6	
634 MeV	10°	C_{LL}	0.849	0.541	0.772	20	5	48
	10°	C_{SL}	0.818	0.511	0.771	28	7	
	35°	C_{LL}	0.782	0.488	0.766	70	19	0
	35°	C_{SL}	0.812	0.507	0.779	35	6	
788 MeV	10°	C_{LL}	0.648	0.368	0.728	67	10	18
	10°	C_{SL}	0.732	0.414	0.758	64	9	
	35°	C_{LL}	0.745	0.421	0.758	81	22	23
	35°	C_{SL}	0.775	0.431	0.760	75	19	

tion to precess. The neutrons then passed through a circular aperture of diameter 2.54 cm in a lead and steel collimator of length 335 cm. The exit was about 729 cm from the center of the LD_2 target.

The neutron beam entered the experimental area (Fig. 3) through the collimator and a 3.8-cm-thick lead plug, which was used to convert γ rays in the beam. It passed through an intensity monitor, two spin precessing magnets with vertical fields (Lorraine and Castor), a relative neutron polarimeter (JPAN, identical to NPAN in Refs. [170,173]), and finally the polarized proton target. After a change in beam conditions (energy or spin direction), the magnet currents were first adjusted using JPAN to give a nearly pure spin direction before the L-type polarized target. After the magnet currents were determined, the JPAN target and counter were removed from the beam before data taking, leaving only about 7 m of air between the intensity monitor and the polarized target.

The main purpose of JPAN was to measure the spin direction of the peak-energy neutrons (near the proton-beam energy) in order to determine the proper magnet currents. In particular, contamination of the JPAN signals by low-energy neutron events could conceivably lead to inaccurate magnet settings. Therefore the design criteria included good rejection of interactions from low-energy neutrons, as well as a good figure of merit (analyzing power squared times differential cross section). It was decided to detect protons from $n+p$ elastic scattering or $n+C$ quasielastic scattering. Absorbers were used to range out protons from low-energy neutron interactions and pions. Previous measurements of $n+p$ elastic cross sections and polarizations indicated an optimum figure of merit for a recoil proton laboratory angle near 30° ($\theta_{\text{c.m.}} \cong 110°$).

The final JPAN design, shown schematically in Fig. 4, was similar to that of an earlier rapid neutron polarimeter [206]. It consisted of a CH_2 target, a plastic scintillation counter ($N1$) to detect charged particles emitted from the neutron interactions in the CH_2, brass absorbers, and four identical plastic scintillation counters (NL, NR, NU, ND—left, right, up, down) located at 30° to the beam. The CH_2 target was a right circular cylinder (10.2 cm in diameter, 10.5 cm in length) with its axis along the nominal beam line. The CH_2 target fit snugly in a brass absorber 20.3 cm wide, 20.3 cm high, and 10.2 cm along the beam. There were additional absorbers downstream of the CH_2 target of 10.2 cm width and 22.9 cm length along the beam. The thicknesses of these brass plates were 2.54, 3.81, and 6.35 cm at $T_n = 484$, 634, and 788 MeV, respectively. The plastic scintillators were of thickness 0.64 cm and areas 17.8×17.8 cm^2, in the case of $N1$ and 10.2×10.2 cm^2, for the other four counters. Coincidences between $N1$ and each of the other counters ($N1 \cdot NL, N1 \cdot NR, \ldots$) were recorded with the on-line computer. The widths of all discriminator outputs were 20 nsec. Left-right and up-down asymmetries were computed. One example of a magnet sweep is shown in Fig. 5, which took roughly 8 h

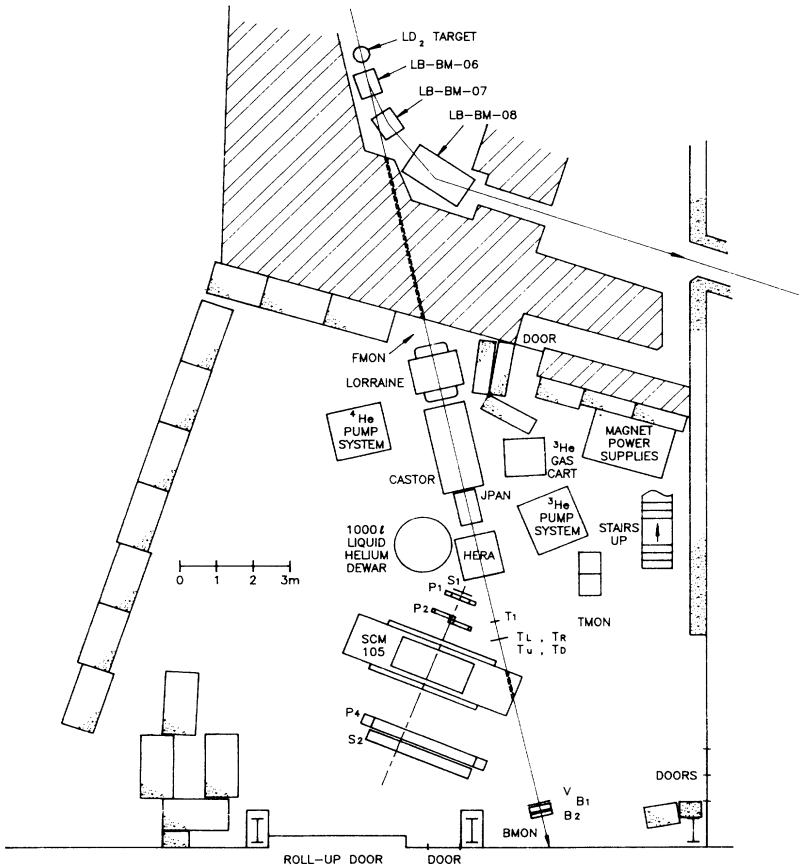

FIG. 3. Layout of the experimental area. The neutron beam entered from the top of the figure through a collimator and then passed through the front beam-intensity monitor (FMON), spin-precession magnets (Lorraine and Castor), a relative neutron polarimeter (JPAN), and the polarized target (HERA). The magnetic spectrometer consisted of scintillation counters (S_1,S_2), multiwire proportional chambers (P_2), and drift chambers (P_1,P_4) attached to a large-aperture magnet (SCM105). Two other beam-intensity monitors (TMON, BMON) are also shown, as well as various equipment associated with the polarized target and magnets.

of beam time.

The JPAN analyzing power was estimated from maximum measured asymmetries from magnet sweeps, from the proton-beam polarization and from the spin-transfer parameters in Refs. [184,190]. It decreased from about 0.16 at 484 MeV to 0.09 at 788 MeV. Over this same range of energies and laboratory angles, the *np* elastic-scattering polarization varied between 0.25 and 0.40. However, JPAN detected particles from the interactions of neutrons with both hydrogen and carbon in the CH_2 target, which accounts for the lower effective analyzing power than for scattering from pure hydrogen.

An extensive analysis of magnet results from this experiment and others was performed to obtain the best estimates of the beam spin at JPAN [207]. Results from 54 magnet sweeps with various proton-beam spins and energies over a six-year period were included. Calibration constants relating spin precession to the beam energy and magnet currents were derived for Lorraine, Castor, and the magnets immediately downstream of the LD_2 target (LB-BM-06 and LB-BM-07). A number of simplifying assumptions were made which appear to be reasonably consistent with the data. For example, nonlinearities in two of the magnets, hysteresis effects, and possible small deviations from the nominal proton-beam spin direction were all ignored, assuming these were all negligible. The results indicate that the neutron-beam spin direction at JPAN was known to about $\pm 3°$.

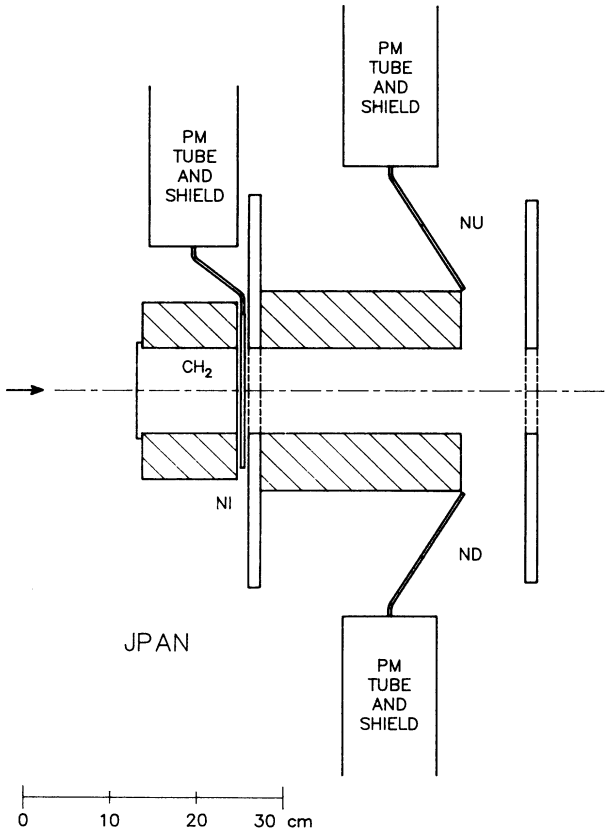

FIG. 4. Side view of the relative neutron polarimeter JPAN. Scintillation counters *N*1, *NU*, and *ND* are shown; counters *NL* and *NR* were symmetrically located to the left and right of the nominal beam center line. The CH_2 target and counter *N*1 were centered on the beam line. The other four counters were centered on lines from the middle of the CH_2 target at 30° to the beam line. The brass absorbers and a portion of the aluminum support structure are also shown.

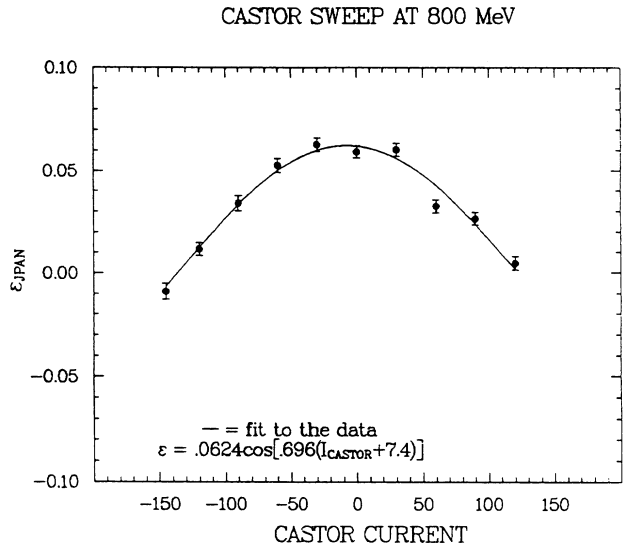

FIG. 5. Example of a magnet sweep for Castor. The observed left-right asymmetries in JPAN as a function of the Castor current (in amps) are plotted along with a cosine curve fit to these data. These measurements were made in roughly 8 h of beam time. The maximum asymmetry corresponds to *S*-type polarized neutrons, and a zero asymmetry corresponds to *L*-type neutrons.

The effects of low-energy beam neutrons in JPAN are of concern, since they could lead to inaccurate settings for Lorraine and Castor by providing a background asymmetry. The number of such neutrons was comparable to the number of peak-energy neutrons [200]. Their effects were reduced by the presence of the brass absorbers. These absorbers were chosen to have a length along the CH_2-to-scintillator path corresponding to the range of protons with a momentum P_p. The value of P_p was chosen to be $\sim 80\%$ of the momentum of an *np* elastic proton (from peak-energy neutrons) at the same laboratory angle. Therefore most of the low-energy beam neutrons were not able to cause coincidences in JPAN. Furthermore, at 800 MeV, the spin-transfer parameters K_{NN} and K_{LL} for producing these neutrons were measured to be smaller in magnitude than K_{LL} for the $pd \rightarrow npp$ reaction [184].

Evidence from the analysis of the many magnet sweeps [207] also suggests small effects on the knowledge of the peak-energy neutron-spin direction. In the range of energies that could cause coincidences in JPAN, the magnitude of K_{NN} is small compared to K_{LL} [184,190]. Therefore, to a good approximation, all these neutrons were *L* type after the LD_2 target, even though the proton-beam spin deviated by up to 30° from pure *L* type going into the LD_2 target. One large class of sweeps had essentially no net change of the neutron spin between the LD_2 target and JPAN. For this class the presence of lower-energy beam neutrons would not affect the desired magnet

currents since they would all be L type again, just as at the LD_2 target. For another class a 90° or 180° net spin change occurred for the peak-energy neutrons. Lower-energy neutrons would have been precessed more, potentially biasing the derived magnet currents. However, there was no evidence of differences with net spin change in the calibration constants.

Two improvements were made to the fit in Ref. [207]. One was to take into account the small deviation of the proton-spin direction from the nominal, which was typically less than 5°. This caused a change in the computed neutron-spin direction at JPAN of up to 1.5°, depending on beam energy. The second correction resulted in a change of about 3° in the neutron-spin direction at 788 MeV. The many magnet sweeps suggested consistency between the predicted [207] and observed magnet currents at the other energies, but not at 800 MeV. The systematic difference at the highest energy corresponded to $2.6°\pm0.5°$ and may have been caused by nonlinearities in the fringe fields of LB-BM-06 and LB-BM-07 at the highest beam energies and magnet currents.

B. Beam-intensity monitors

Several independent measurements of the relative neutron- and proton-beam intensities were recorded during the experimental runs. These included a secondary emission monitor (SEM) and the line-B polarimeter signals for the proton beam, and the front, target, and back monitors (FMON, TMON, and BMON, respectively) for the neutron beam; see Figs. 2 and 3. A number of these monitors were sensitive to beam position as well as the intensity.

The SEM [208] (denoted LB-ER-01 in Fig. 2) consisted of three foils (one emitter and two 100-V bias foils) in the beam-line vacuum. The emitter current was integrated and digitized. Dark currents were not monitored directly during the experiment. Instead, they were estimated from a comparison of SEM and of other monitor counts during polarized and quenched beam periods, corresponding to a factor of about 4–5 difference in beam intensity. The SEM was assumed to be linear over this range of intensity. These estimated dark currents were subtracted from the raw SEM counts on a run-by-run basis. This correction was generally less than 18%.

FMON, located immediately downstream of the collimator, was eventually selected as the primary beam-intensity monitor. It is shown schematically in Fig. 6. The first four counters of FMON consisted of the charged veto A and the detectors $M1$, $M2L$, and $M2R$, which were all constructed of 0.32-cm-thick plastic scintillator with an area of 10.2×10.2 cm^2. Each was viewed by a single photomultiplier that was well shielded from the magnetic field of Lorraine. The CH_2 target was 2.54 cm thick, 6.4 cm wide, and 8.9 cm high. The final detector $M3$ was 0.64 cm thick with an area 22.9×22.9 cm^2 and had a 8.3-cm-diam hole that was centered on the nominal beam line. It followed a 2.54-cm-thick brass absorber, 22.9 cm wide and 24.1 cm high, with a 7.6-cm-diam hole, also centered on the beam line. The brass absorber stopped low-energy charged particles, created in the CH_2 target, preventing them from reaching $M3$. All elements of FMON were optically surveyed before the start of the experiment.

Left and right coincidences and other signals were formed with commercial NIM electronic modules and were scaled at the end of each polarized and quenched beam period. These signals were $M13=\bar{A}\cdot M1\cdot M3$, $MLT=\bar{A}\cdot M1\cdot M2L\cdot M3$, $MRT=\bar{A}\cdot M1\cdot M2R\cdot M3$, and $MTOT=MLT+MRT$. Corresponding accidental coincidences were determined by measurements made with $M1$ delayed by 60 nsec with respect to the other signals. Rates were generally low, corresponding to roughly 100 $MTOT$ per second average. Including the 9% (at $T_p=800$ MeV) or 3% (at the other energies) duty factor

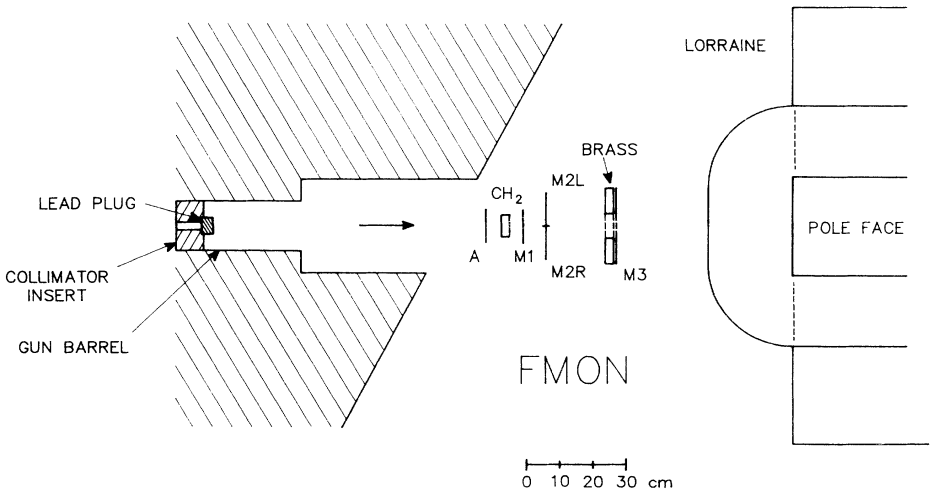

FIG. 6. Schematic view of the front monitor FMON (top view). The neutron beam entered from the left, through the collimator and lead plug (to reduce γ-ray contamination in the beam). The CH_2 target, scintillation counters A, $M1$, $M2L$, $M2R$, and $M3$, and the brass absorber are shown. After FMON, the beam entered the spin-precession magnet, Lorraine.

for the LAMPF polarized beam gave instantaneous rates of about 1000–4000 MTOT per second. The accidental coincidences were typically less than 0.1% of the true coincidences. Widths of the discriminator output signals from $M1$, $M2L$, $M2R$, and $M3$ were 10 nsec and from A were 30 nsec.

The target monitor TMON was located downstream of the polarized target along the nominal beam line. It measured the flux of charged particles produced in the target at small angles to the beam. Five plastic scintillation counters comprised TMON. A single counter ($T1$—20.3 cm wide, 43.2 cm high, 0.64 cm thick) was located in the beam line 190 cm downstream of the polarized target and 56 cm upstream of the plane containing the other four counters (TL, TR, TU, and TD, each 10.5 cm wide, 26.0 cm high, and 0.64 cm thick). These four counters were arranged so that there was a 10.5 cm$\times$10.5 cm hole approximately centered on the beam line. Signals from the single photomultiplier on each counter were discriminated, and coincidences of $T1$ with each of the other four counters were scaled. An electronic OR was formed ($TTOT$), as well as various accidental coincidences. This monitor was removed when the magnetic spectrometer was centered at $\theta_{\rm lab}\simeq 10°$ because of spatial limitations.

Unlike the other two neutron-beam intensity monitors in the experimental area, which measured secondary-particle fluxes, the back monitor BMON measured the relative neutron flux directly. It consisted of a thin charged-particle veto (V—61.0 cm wide, 24.1 cm high, and 0.64 cm along the beam) and two 61.0-cm-wide, 25.4-cm-high, and 11.4-cm-thick plastic scintillation counters ($B1$,$B2$) each viewed by two 12.7-cm-diam photomultipliers. These three counters were all approximately centered on the nominal beam line. The beam intensity was monitored by the quantity $BLR=(\bar{V}\cdot B1L\cdot B1R)\cdot(\bar{V}\cdot B2L\cdot B2R)$. Accidentals were monitored by

$$BLR\,ACC=(\bar{V}\cdot B1L\cdot B1R)_{\rm del}\cdot(\bar{V}\cdot B2L\cdot B2R)\ .$$

Various studies of the stability of intensity monitor ratios were performed at the 497 MeV proton-beam energy. All monitor coincidence counts were corrected for accidentals, and the SEM counts were corrected for dark current as noted before. The line-B polarimeter counts were combined as follows: If L_+ (R_+) and L_- (R_-) denote the coincidences for the protons scattered left (right) in the polarimeter for normal and reverse beam polarization, respectively, then it can be shown that, to a good approximation,

$$AP=\frac{\sqrt{L_+R_-}-\sqrt{L_-R_+}}{\sqrt{L_+R_-}+\sqrt{L_-R_+}}\ .$$

In this formula, A is the average analyzing power for protons scattered both left and right and P is the average N-type (up-down) beam polarization for both normal and reverse spin directions. Defining

$$\varepsilon_\Omega=\frac{\sqrt{L_+L_-}-\sqrt{R_+R_-}}{\sqrt{L_+L_-}+\sqrt{R_+R_-}}\ ,$$

which is approximately the asymmetry in solid angle times efficiency for protons scattered left and right, then, to a good approximation, the ratio of beam intensities for normal and reverse spin directions is given by [205]

$$\frac{I_+}{I_-}\cong\frac{(L_++R_+)}{(L_-+R_-)}\frac{(1-AP\varepsilon_\Omega)}{(1+AP\varepsilon_\Omega)}\ .$$

In this expression, differences in left-right analyzing powers or normal-reverse beam polarizations have been ignored. Similar formulas hold for the up and down polarimeter counts. The target monitor counts and the quantities MLT and MRT for the front monitor were treated in the same way as for the polarimeter.

Studies of the monitors indicated that the measured intensities $MTOT$, BLR, and SEM tracked each other better than 1% from run to run. (Much larger variations were experienced at times when significant retuning of the beam occurred, such as after spin-direction changes or changes to the polarized ion source.) The line-B polarimeter and target monitor showed 8.5% and 1.5% variations compared with the other monitors. Some of the variation may have been caused by changes in the proton-beam position and width at the polarimeter and LD_2 targets and, also, the neutron-beam position at the polarized target. In turn, these were caused by many factors, including variations in the polarized ion source and accelerator operating conditions, and also changes in strippers and beam tune required for other beam lines. Small spin-correlated beam motion probably also contributed to the intensity variations.

The quantity $MTOT$ from the front monitor was chosen as the primary measure of the relative neutron-beam intensity for a number of reasons. It was demonstrated that variations in the proton-beam position and size would lead to differences in the number of neutrons transmitted through the collimator per incident proton. This suggests that either BLR or $MTOT$ is more reliable than SEM or the line-B polarimeter. Changes in the beam position might also result in a difference in SEM counts due to variations in the characteristics of the foil surfaces (secondary emission coefficients). Likewise, changes in the neutron-beam position at the polarized target could cause different fractions of the neutrons to be scattered or absorbed. In this case, $MTOT$ is favored over BLR or $TTOT$. Possible problems with changes in the $B1$ and $B2$ counter gains with time (and hence neutron detection efficiency) also contributed to the choice of FMON for the primary beam-intensity monitor. Nevertheless, the ratio of total beam for normal and reverse spin directions as computed by SEM, BLR, and MTOT agreed to better than $\pm 0.5\%$ in all cases. An error in the ratio of that magnitude would lead to an uncertainty in C_{LL} or C_{SL} of less than ± 0.017, much less than the statistical errors.

C. Polarized target

The polarized proton target (PPT) was continuously polarizing, utilizing the technique of dynamic nuclear polarization [209]. The apparatus consisted of a magnet, a ^{3}He refrigerator, a microwave system, and a nuclear-

magnetic-resonance (NMR) system. The superconducting magnet (HERA) and refrigerator were constructed at CEN Saclay [210,211] and were modified at LAMPF as described in Ref. [122].

The magnet was iron-free and consisted of a split pair of Helmholtz coils that produced a 2.5-T central field, uniform to within 0.45 mT in a sphere 5.0 cm in diameter. These coils were cooled in a liquid-^{4}He bath, which also served as the ^{4}He reservoir for the refrigerator. A 1000 l Dewar and rigid transfer line were used to feed the magnet continuously with liquid ^{4}He. In addition, liquid-nitrogen-cooled radiation shields surrounded the coils and were thermally insulated by a cryopumped vacuum. The magnet provided an unobstructed conical aperture of 45° half angle, from the magnet center, about the field direction. It was optically surveyed to have the magnetic axis along the nominal beam line. Corrections to the incident-neutron-beam spin and the outgoing proton trajectories for the influence of the PPT magnetic field are described in Sec. II D.

The target cryostat phase separator received liquid ^{4}He directly from the magnet reservoir. The gas phase was used to cool two radiation shields and the incoming ^{3}He gas to about 10, 50, and 100 K, respectively. The liquid phase was evaporatively cooled using a rotary vane pump and was used to further cool the ^{3}He to roughly 2 K in a heat exchanger. After the ^{4}He pump, the gas was filtered; some was then recovered and reliquified, and the rest was used for filling the magnetic spectrometer gas bags. The liquid-^{3}He bath, surrounding the target material, was further cooled to below 0.5 K by evaporation. The ^{3}He pump system consisted of three stages of Roots blowers and a double-stage rotary vane fore pump. The compressed gas was passed through oil filters and a liquid-nitrogen-cooled activated-charcoal trap before returning to the ^{3}He refrigerator in a closed loop. The ^{3}He was circulated at a rate of roughly 4 mmol/sec. The vapor pressure of the ^{3}He at the target material was measured by a remote sensing manometer.

The target holder consisted of a cylindrical microwave cavity made of copper of 0.15 mm thickness, containing an inner Teflon cell (wall thickness 0.25 mm), which held the target material. Materials outside the target holder included a total of 2.5 mm aluminum, 0.64 mm stainless steel, and 0.13 mm aluminized Mylar. The inner cell was 3.7 cm in diameter and 5.7 cm long ($\sim$61 cm^3). It was surrounded by a saddle-shaped NMR coil near its center and by two series-connected "hairpin"-shaped coils that sensed the polarization at the target ends. A third NMR coil ran down the target center along its axis. The axis of the target cell was aligned along the nominal beam line with x rays. Attempts to use the neutron beam to obtain a radiograph of the target (see Ref. [212]) were unsuccessful. The target material was 1,2-propanediol doped with a Cr(V) paramagnetic complex. It was prepared in the form of beads about 1 mm in diameter by freezing liquid propanediol drops in liquid nitrogen. The beam form was used to improve thermal contact with the liquid ^{3}He and to dissipate the heat load of the absorbed microwave radiation. The packing fraction of the beads was roughly $\frac{2}{3}$. The distance between the centers of the LD_2 and polarized target was 15.2 m.

The target material was irradiated with 69-GHz microwaves to polarize the protons to about 76%. The microwave source was a 5-W carcinotron. The frequency was measured by either of two adjustable resonant cavity wavemeters. A microwave attenuator regulated the power delivered to the target to be on the order of 100 mW. The PPT magnetic-field direction remained fixed during the experiment. The polarization direction was reversed by changing the microwave frequency (see Ref. [209]). During the experiment, these reversals occurred about once every 6–8 h, on the average, when the beam was on.

The NMR system was used to measure the target polarization. A rf oscillator drove a serial-tuned Q-meter circuit similar to that of Court [213], with high intrinsic linearity. The rf frequency was swept over a range of 460 kHz about a central frequency of 106.45 MHz. The Q-meter output was digitized and recorded with a PDP 11/23 computer as a function of frequency. Typically, 1000 sweeps were averaged to obtain a good signal-to-noise ratio. The area of the NMR signal was numerically evaluated after subtraction of an off-resonance response corresponding to a shift in the central magnetic field of 14 mT.

Data acquisition for the experiment took place over a period of 4.5 months. During that time, 16 calibrations of the absolute target polarization were performed. For these, the NMR signal was recorded with the microwaves turned off and the protons in the target material in thermal equilibrium with the liquid ^{3}He at a temperature of about 1 K. This temperature was deduced to an accuracy of 1% from the ^{3}He-vapor pressure measured by the capacitive manometer. Under these conditions the nuclear polarization ($\sim$0.0025) is calculable. Comparing the area of the thermal equilibrium signal with the enhanced signal when the target was dynamically polarized gave the absolute polarization. The accuracy of the absolute calibration is estimated to be $\pm$3.3%. Measurements were performed with all three NMR coils, and these agreed to within $\pm$2.4%. The maximum positive and negative target polarizations were $+0.80$ and -0.78, respectively. Table I contains the average target polarization for each spin parameter and energy, as well as the number of target reversals.

Background measurements at most spectrometer settings and beam energies were performed by replacing the normal target material with graphite beads of approximately the same diameter as the polarized beads. At times, liquid ^{3}He was also introduced into the target holder or empty target runs were taken.

D. Magnetic spectrometer

Charged particles were detected in a large acceptance ($\sim$100 msr) magnetic spectrometer (see Fig. 3) that measured both their momentum and time of flight. The spectrometer detectors and components included a scintillation counter S_1, a drift chamber P_1, a pair of multiwire proportional chambers (MWPC's) P_{2L} and P_{2R}, a large-aperture dipole magnet (with designation SCM105), a

large-area drift chamber P_4, a 25-element scintillation counter hodoscope S_2, various helium-filled gas bags, and mechanical supports. All detectors were roughly perpendicular to the SCM105 center line and were optically surveyed with an accuracy of ± 0.25 mm at the start of the experiment. The spectrometer moved as a unit on large air pads and was located with the magnet center at about 10° and 35° with respect to the nominal beam line. At the smaller angle, the beam passed through the magnet gap, whereas at the larger angle it went through a hole in the magnet yoke. The detected particles were primarily protons and deuterons with a laboratory scattering-angle acceptance of approximately 27°. Very few pions or electrons were recorded because their low momenta or fast flight times caused them to be rejected by the trigger. Since all spectrometer elements were rigidly attached to the magnet, the locations of the detectors will be specified in the coordinate system centered on the SCM105 center (Z—the magnet center line along the incident particle direction, Y—up, and X—beam left).

The S_1 counter consisted of a single scintillator (51 cm wide, 28 cm high, and 0.64 cm thick), viewed by a single photomultiplier during a portion of the 35°, 634-MeV C_{LL} and most of the 788-MeV data. Timing corrections for the location of the interaction were made as described in Sec. III B. This counter was replaced part way through the experiment by a pair of scintillators $25.5\times 28\times 0.64$ cm^3 located side by side. In this case each scintillator was viewed by two photomultipliers mounted vertically to improve the timing accuracy. In addition, a more restrictive trigger was implemented to reduce the trigger rate at small angles (see Sec. II E). The distances between S_1 and the SCM105 center plane were 238.2 and 257.3 cm for the single- and double-scintillator cases, respectively.

The small drift chamber P_1 had an active area of 61×61 cm^2 and was located 219.2 cm upstream of the SCM105 center. During the running period when the single S_1 counter was used, P_1 consisted of three detector planes, two with vertical and one with horizontal (X, X', and Y, respectively) sense wires. When the pair of S_1 counters was installed, a Y' detector plane was added 21.1 cm upstream of the other planes in order to increase the vertical detection efficiency.

Each detector plane consisted of 76 sense wires of 20-μm-diam gold-plated tungsten, each spaced at 8 mm. Halfway between each adjacent pair of sense wires was a field-shaping wire of 25-μm-diam gold-plated tungsten. The X and X' planes were offset by about 2.5 mm to assist in the determination of whether the particle passed to the left or right of the sense wire (left-right ambiguity problem). Aluminized-Mylar cathode planes of thickness 76 μm were located in front and back of the sense-wire planes at a distance of 4.76 mm. The outer windows were made of 0.25 mm Mylar. The gas mixture used in the chamber was 85.3% argon, 14.3% isobutane, 0.36% freon 13-B1 ($CBrF_3$), and ethanol at 0 °C vapor pressure. The gas pressure was slightly above local atmospheric pressure. The operating voltage was different for each detector plane and averaged about 2100 V. The readout system was based on a delay-line technique [214], where the sense wire with a signal was determined by measuring differences of propagation time. The delay-line construction was similar to that in Ref. [214]. Preamplifiers on the ends of the delay lines had a gain of roughly 40. The preamplifier output signals were sent via coaxial cable to constant-fraction discriminators (Phillips model 715) and then to CAMAC time-to-digital converters (TDC's) (LeCroy model 2228A).

The two MWPC's that made up P_2 (P_{2L},P_{2R}) had active areas of 51.2×51.2 cm^2. Each consisted of three detector planes X, X', and Y, similar to those of P_1. Detector P_{2R} was located upstream of P_{2L}, their distances from the center plane of the SCM 105 being 146.9 and 136.8 cm, respectively. All three detectors S_1, P_1, and P_2 were centered approximately on the SCM105 center line. The G10 fiberglass-epoxy frames of the P_2 chambers overlapped, thus minimizing material along particle paths that passed through the active areas of P_{2L} and P_{2R}. As a result, the portion of the angular acceptance of the spectrometer corresponding to the P_2 chamber frames was missing. The anode (sense) wires were 20-μm-diam gold-plated tungsten with a spacing of 2.0 mm and a tension of roughly 45–55 g. Near the edge of each detector plane, three additional wires of increasing diameter were located parallel to the sense wires to prevent electrical breakdown to the frames. Cathode planes of 51 μm aluminized Mylar were located in front and back of the anode planes at a distance of 6.35 mm. The outer gas windows were 51 μm Mylar covered with opaque 51-μm Mylar tape. The individual G10 frames were bolted together with threaded nylon rods and nuts. The gas seal was formed with silicon-rubber adhesive (RTV). The gas mixture was 64.5% argon, 35.0% CO_2, and 0.4–0.5% freon 13-B1, to reduce electrical breakdown in the chamber. The chambers were operated slightly above local atmospheric pressure at a voltage of $\sim$4050 V. Preamplifiers for each sense wire were mounted directly on the chambers. Signals from the preamplifiers were transmitted 61 m on twisted-pair flat cable to amplifiers and discriminators. The discriminator outputs were sent to latches that were read through CAMAC. The logical OR of all discriminator outputs (FAST-OR) was formed by a combination of the home-built chamber electronics and commercial NIM modules and was used in the trigger (see Sec. II E). Additional details on these chambers can be found in Refs. [215–217].

A large-aperture magnet (213×84 cm^2) was used to analyze the momentum of charged particles produced by interactions in the polarized target. The magnet was operated at 2000 A for measurements at all three beam energies and both spectrometer angles. This gave a field integral in the magnet center of $\int B\,dl \cong 770$ kG cm. The magnet was mapped twice at currents of 1200 and 2000 A. The first measurements were performed with the Fermilab ZIPTRACK [218] before the actual experiment. Analysis of these results indicated relatively large point-to-point variations in the field values and the need for more extensive spatial coverage. The second measurements were performed by the LAMPF magnet group using their "rapid mapper" after the completion of the ex-

periments. All three magnetic-field components were measured simultaneously on a grid with uniform spacing of 5.08 cm in X (left-right, from -101.6 to $+101.6$ cm), 5.08 cm in Y (vertically, from -30.5 to $+30.5$ cm), and 2.54 cm in Z (along the direction of the SCM105 center line) for a distance of 304.8 cm. Additional points were measured downstream of the SCM105 in the direction in which the protons were deflected (beam-left). These data were checked for consistency with Maxwell's equations. In order to evaluate the magnetic field at an arbitrary point in the measured field volume, each of the SCM105 magnetic-field components was expressed as a second-order polynomial in position about each point in the measured field grid. This interpolation procedure was necessary for the numerical integration process and is described in more detail in Ref. [219].

A Monte Carlo program was written to integrate numerically the proton trajectories through the HERA and SCM105 magnetic fields. The beam was modeled to have a finite beam-spot size, divergence, and energy spread based on the diameter and location of the collimator and PPT, and measurements reported in Refs. [200,201]. The interaction point within the polarized target was not varied. A range of scattering angles was generated to fill the spectrometer acceptance, and corrections for energy loss in the target were made. The locations of the trajectories in the scintillators and chambers, as well as the scattering angles and time of flight from S_1 to S_2, were recorded. From this information corrections to the particle angles and a look-up table for $\int B\,dl$ in the SCM105 were obtained. In an alternate scheme, the ZIPTRACK data were used to develop a semiphenomenological expression for $\int B\,dz$ in terms of the values of X and Y at the center of the SCM105, obtained by projection of a straight-line fit to P_1 and P_2. Detailed comparisons of the results from the look-up table and the phenomenological parametrization gave similar missing-mass resolutions and signal-to-background ratios. The look-up table was adopted for all results presented in this paper.

The drift chamber P_4 consisted of two planes with 160 vertical sense wires (X and X'), two planes with 176 sense wires rotated 17.63° from the vertical (U and V), five high-voltage planes of closely spaced wires, and two ground planes. The sense wire was 25-μm-diam gold-plated tungsten and the wire spacing was 19.06 mm for X and X' and 18.16 mm for U and V. The distance between the sense wires and high-voltage cathode wires was 9.50 mm. The chamber gas was a mixture of 50% argon and 50% ethane, and the operating voltage was approximately 2200 V. Groups of 16 adjacent sense wires were read using a delay line. Amplified signals from each delay-line end were discriminated with LeCroy 623B, 620AL, or 620CL NIM modules, and the outputs were fed to LeCroy 2228A CAMAC TDC's. Furthermore, the discriminator output from one end of each delay line was fed to a CAMAC coincidence register that was strobed by the trigger signal. Only those left-right TDC pairs that were flagged by the coincidence registers were read into the computer to minimize the number of data words transferred. The active area of the chamber was 305×102 cm^2. It was located 220 cm downstream of the SCM105 center and was offset beam-left of the magnet center line by 55.5 cm. Additional details are given in Ref. [220].

The scintillation counter hodoscope S_2 consisted of 25 elements with scintillator dimensions 111.8 cm high, 14.0 cm wide, and 1.27 cm thick. There was an overlap of approximately 0.6 cm with the two neighboring counters. The hodoscope center was displaced beam-left of the SCM105 center line by 56.2 cm to take into account the deflection of the positively charged particles by the magnet. It was also roughly centered at beam elevation and was located 267 cm downstream of the SCM105 center. Each scintillator was viewed from above and below through Lucite light guides by a pair of photomultiplier tubes. Information from this hodoscope allowed corrections to the P_4 drift time for the flight time of the particles through the spectrometer and permitted calculation of the particle mass.

In order to minimize multiple scattering, helium-filled gas bags were installed between P_1 and P_2 and between P_2 and P_4 (through the SCM105). Entrance and exit windows were each 51 μm Mylar. Some of this helium gas was recycled from the boil-off of the polarized target.

The spectrometer was moved a number of times during the experiment. The location of the SCM105 center and axis relative to the polarized-target center and to the 10° or 35° lines surveyed on the floor of the experimental area were recorded. Corrections to scattering angles and target projections were applied during the analysis using these data.

E. Electronic logic and data acquisition

A good event trigger was defined as the simultaneous detection of a charged particle in S_1, S_2, and at least one plane of P_2 (see Fig. 3). The scintillator S_1 defined the timings of the good event trigger, the starts of all TDC's, and the analogue-to-digital converters (ADC's), and latch gates. A schematic diagram for the logic with two S_1 counters is shown in Fig. 7. Most of the trigger electronics involved commercial NIM modules.

Raw signals from the photomultipliers of the S_1 and S_2 counters were sent to constant-fraction discriminators. The discriminator outputs from the two photomultipliers of S_{1L} and S_{1R} were then sent to home-built time averagers [221]. The discriminator outputs for the two photomultipliers on each S_2 counter were sent to dual-coincidence modules and then to logical fan-in modules to form the quantities HL and HR. Typically, HL consisted of the OR of the S_2 counters H_1-H_{14} and HR consisted of $H_{12}-H_{25}$, so that a few counters were in both HL and HR. Depending on the beam energy and spectrometer angle, the inputs to HL and HR were changed by one or two counters. A fast trigger signal (FTRG) was produced by the coincidence of S_{1L} (S_{1R}) and HL (HR). This trigger was inhibited when the beam was undergoing a spin change or when the source was in the quench mode (see the description of the slow gating logic below). When the S_1 counter with a single photomultiplier was used, its discriminator output was put in coincidence with $H=HL+HR$.

The fast trigger signal was used for TDC starts for P_1, P_4, and the S_2 counters and for the latch and ADC gates for the hodoscope counters. It was also sent to a latch circuit to prevent additional triggers until the computer had processed the event or until the CAMAC information had been cleared. The CLEAR was initiated if no P_2 FAST-OR was present, indicating that there was no particle detected in any plane of either P_{2L} or P_{2R}. If a P_2 FAST-OR occurred in coincidence with the fast trigger latch signal, the MWPC information was stored and the computer reading of the event was started as a Master Trigger (MTRG). Average MTRG rates ranged from about two per second to 100 per second, depending on the beam energy, spectrometer angle, and beam intensity. Computer dead time was generally less than 50% at 10° and less than 20% at 35° laboratory spectrometer angle.

A typical computer event record consisted partly of 51 words corresponding to the P_4 and S_2 latches and the P_1 ADC's and TDC's. These were followed by a variable number of words containing P_4 delay-line TDC's, hodoscope counter ADC's and TDC's, and P_2 wire information. (The P_4 and S_2 latches determined which ADC and TDC words to read into the computer.) These words were read via CAMAC into a PDP 11/60 computer with a microprogrammable branch driver (MBD) [222] and then recorded on magnetic tape. The data-acquisition software was the LAMPF "Q system" [223] with experimenter-written subroutines.

A total of 276 scalars were read into the computer and stored on magnetic tape during each polarized beam-spin reversal. These scalers recorded rates from beam-intensity and beam-polarization monitors and from various modules in the good event logic, as well as singles rates in some scintillation counters. Information from the polarized target was also recorded each time the scalers were read. Beam and target polarizations, chamber efficiencies, and ratios of various beam monitors and of FTRG and MTRG to beam monitors were all computed on line to check the behavior of the experimental apparatus.

Various slow gating signals were generated for use by the good event logic and the scalers. The run gate (RG) was set true at the start of a run and set false at the end. The beam gate (BG), sent from the LAMPF Central Control Room, was true for the duration of each accelerator macropulse and false otherwise. The polarized-beam gate (POL) was true when the beam was polarized and false during periods when the source was in the quench mode. The two beam-polarization states (N, R —normal,reverse) were also sent from the ion source. A spin-change (SC) signal was generated as $\underline{\mathrm{SC}} = \overline{N} \cdot \overline{R} \cdot \mathrm{POL}$. Scalar reads were initiated with $\mathrm{RG} \cdot \overline{\mathrm{SC}}$. Scalers were gated with either P, Q, or I signals, where $P = \mathrm{POL} \cdot \mathrm{BG} \cdot \mathrm{RG} \cdot \overline{\mathrm{SC}}$ corresponded to polarized beam and $Q = \mathrm{POL} \cdot \mathrm{BG} \cdot \mathrm{RG} \cdot \overline{\mathrm{SC}}$ to

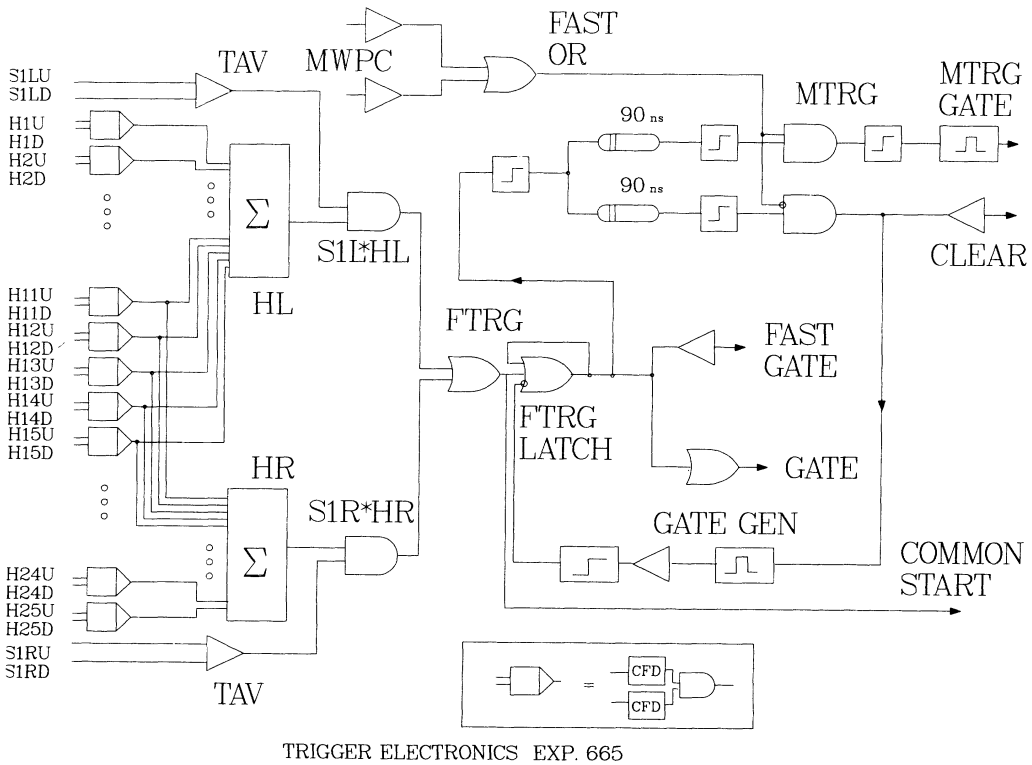

FIG. 7. Schematic view of the trigger logic for the magnetic spectrometer. The fast trigger (FTRG) was an OR of the left half of S_1 in coincidence with the left hodoscope counters and the right half of S_1 in coincidence with the right hodoscope counters. Some overlap of S_2 counters was used to ensure good acceptance for the elastic events. In addition, the master trigger (MTRG) required a signal from P_2. Constant-fraction discriminators (CFD) were used for the hodoscope counters.

quenched beam. The I signal was P in coincidence with a signal, indicating the computer was not busy, and was used to control data taking. Finally, the N and R signals were put in coincidence with a 10-kHz clock and scaled with both P and Q gates in order to permit the calculation of beam polarization via the quench method. The N- and R-gated clock scalers were also used to provide a check on the spin assignment for each of the scaler reads.

During a portion of the 788-MeV data collection, a rapid beam-spin reversal occurred at the rate of 30 Hz. There were no quenched beam periods, only polarized beams with opposite spin directions. Modifications to the gating and scaler logic were made in order to record beam-intensity monitors and other signals in separate scalers for the two beam states. In this case the scalers were read at approximately 2-min intervals.

III. DATA ANALYSIS

A. General

The data analysis was carried out in two stages because of the large number of events and computer time needed to reconstruct the trajectories. The first stage involved the conversion of the chamber information to spatial coordinates in the spectrometer system (see Secs. III B and III C). Events with too little information to compute the momentum and scattering angles were removed. Cuts on the quality of the chamber data were imposed as described in Sec. III C, but no restrictions were applied to the kinematical quantities. The good events were written to data summary tapes (DST's). The second stage of the analysis (Secs. III D and III E) involved calculation of kinematical quantities from the chamber coordinates. Final cuts were placed on the particle mass and the target projections. The data were binned in c.m. angle, and the elastic signal was extracted from missing-mass spectra in each bin.

B. Scintillators

The scintillation counter data were handled first in the process of making DST's. As noted above, the S_1 scintillator defined the timing of the trigger and TDC starts. In the case of the two S_1 scintillators with two photomultipliers each, the timing was approximately independent of position because of the time averagers. Furthermore, during the setup for the experiment, the timing of S_{1L} and S_{1R} was adjusted to be the same to within 0.5 nsec. This was done by comparing their timing to a third counter that overlapped S_{1L} and S_{1R} and that was located immediately upstream of them. When only a single $S1$ scintillator with a single photomultiplier was present, various times had to be corrected for the transit time of the light in S_1. A correction that was linear in the wire number in chamber P_1 was applied to all drift times in P_1 and P_4 and to the time of flight to the S_2 hodoscope counters. The maximum correction corresponded to distances that were slightly smaller than the chamber resolutions.

Timing and position information from S_2 were analyzed next. The event was rejected if there were four or more hodoscope counters hit or if there were hits in nonadjacent counters. For events with a single counter, the X coordinate was assigned to be the center of the counter. The TDC counts were converted to times using calibration constants. The gain for each TDC was calibrated before the experiment and was roughly 0.25 nsec/channel. The offsets were chosen to center the time difference distribution about zero and to give the proper proton mass. (An iterative procedure was required; the proton mass depended on tracking information and time of flight. However, the timing was needed to correct the P_4 drift times.) Changes in the offsets were quite infrequent. The Y coordinate in the counter was taken to be a constant multiplied by the time difference and the flight time from S_1 to S_2 to be the average of the up and down photomultiplier times plus a constant.

Two hodoscope counters were considered adjacent only if they were next to each other, if the difference in Y positions was less than 20 cm, and if the flight-time difference was less than 5.0 nsec. Then the X and Y coordinates and flight time were the average of the values from the two counters. The fraction of events with adjacent hodoscope counters was only about 7–9 % because of the small overlap of the counters.

At 788 MeV, the hodoscope latch gate was timed too late for some hodoscope counters. As a result, the fastest particles for these counters had no timing information. All other data for these events appeared normal. Therefore a flight time was assigned that approximately corresponded to forward elastically scattered protons (21 nsec) for these events. Separate studies of these events showed agreement of the derived asymmetries with the other events within statistical errors.

A histogram of the number of times each hodoscope counter was latched was generated on line. This permitted rapid location of problems with the hodoscope and associated electronic logic. Two-dimensional histograms of hodoscope Y position versus X position and particle mass versus X position made drifts of the offset constants visible.

C. Wire chambers

In order to reconstruct the momentum of a track, X information was needed from P_1, P_2, and P_4 and Y information from at least two of these chambers. An event was rejected as soon as it was determined that these criteria were not met. Likewise, only one track should have been present. If more than one good hit was found in a chamber, then the event was also rejected.

In the data-analysis program, the P_2 information was evaluated first. These MWPC's did not have the problems of the left-right ambiguities associated with the drift chambers P_1 and P_4. After decoding the data words into individual wires identified with the appropriate plane of P_{2L} and P_{2R}, adjacent wires were then grouped together. A maximum of six wires per plane were retained, and gaps of one wire were allowed within a group. The center of the group was chosen as the position of the particle track in the plane. Histograms of the number of times each wire in a plane had been latched were made for di-

agnostic purposes. In addition, there were histograms for the number of wires and of groups per plane. These were used to monitor the chamber performance during data-taking periods and were especially useful for determining the proper operating voltage for the chambers.

Chambers P_{2L} and P_{2R} were first handled separately. If neither the X nor X' plane had a group, then the other chamber was tested. If one plane contained a group of wires but the other did not, then the particle was assumed to have passed through the chamber at that point. The event was rejected in this case if the plane had more than one group present. The Y planes were also treated in this fashion.

If at least one group of wires was found in both X and X' planes, a test was made on the distance $\Delta X_2'$ between the observed position of the group in X' and the calculated position based on the X plane. The calculated position was corrected for the incident angle of the particle in the chamber, assuming the track originated at the center of the PPT. Histograms of $\Delta X_2'$ for P_{2L} and P_{2R} are given in Fig. 8. If the magnitude of $\Delta X_2'$ was more than 4 mm, it was assumed that the groups did not match. The event was rejected if no matches or if more than one match was found. In the case of a unique match, the average X position from the X and X' planes and the average Z for the two planes were used to give the point where the particle passed through the chamber. The final requirement was a unique X and Y position calculated for the same half of P_2.

The data in Figs. 8(a) and 8(b) permit an estimate of the resolution of P_2. The widths of the distributions indicate a spatial resolution of ± 0.69 mm per plane, compared with an expected value of ± 2 mm$/\sqrt{12} = \pm 0.58$ mm, where 2 mm is the wire spacing and a flat distribution of events is assumed. The finite target size, effects of the target magnetic field on the trajectories, multiple scattering, and the presence of δ rays all contributed to a larger than expected spatial resolution. However, events with adjacent double wires improved the resolution. Furthermore, since greater than 90% of all events had both X and X' groups, the overall P_2 spatial resolution improved by a factor of $\sqrt{2}$ and was about ± 0.49 mm in the horizontal direction.

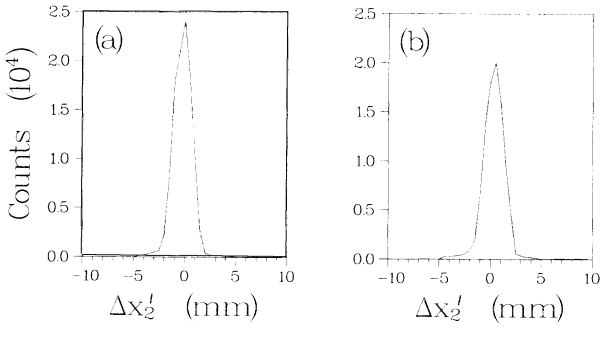

FIG. 8. Histogram of the difference ($\Delta X_2'$) between observed and predicted X' values for (a) P_{2L} and (b) P_{2R}. The predicted value was obtained from the observed X position, assuming the particle trajectory was a straight line from the target center. The widths were approximately ± 0.97 mm.

The reconstruction efficiency was roughly 92%, with an about 3–5% loss from inefficiency of the Y plane. Most of the rest of the inefficiency ($\sim 4\%$ at a 35° spectrometer angle) resulted from mismatches in the X planes. The fraction of mismatches was considerably larger at a spectrometer angle of 10°. This was caused by interactions in S_1, which was in the direct beam at 10°, but not at 35°. Such events often had large slopes at P_2. The computed $\Delta X_2'$ was correspondingly large, especially in P_{2R}. Thus, in some indirect sense, the cut on $\Delta X_2'$ was also a coarse cut on the Z position of the interaction.

Data from the delay-line chamber P_1 consisted of timing from TDC's connected to the ends of the delay lines. Since this chamber was close to S_1 and since the master trigger and TDC start signals had their timing defined by S_1, no corrections were applied to the delay-line timing for the flight time of the particles. The case of S_1 with a single photomultiplier is described in Sec. III B. The TDC words for the delay lines were first tested for the presence of zeros (no start signal or a stop too early compared with the start) or overflows (no stop signal). A flag was set for each plane that contained a zero or overflow in a TDC. The event was rejected if both the X and X' planes had a zero or overflow in their corresponding TDC's.

Next, the time difference and sum were formed (see Fig. 9). The wire number was found from the time difference and a look-up table. This table was created in a separate program that found valley positions from

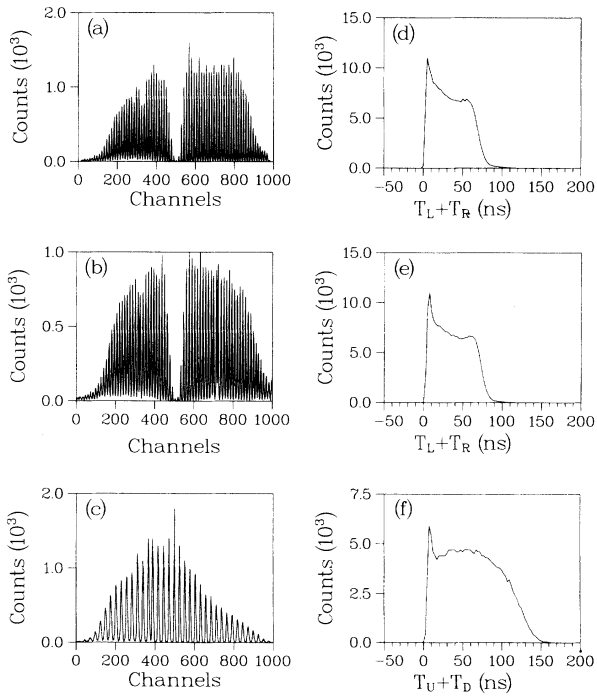

FIG. 9. Histograms of the (a)–(c) time differences and (d)–(f) sums from the delay-line ends of the X, X', and Y planes of P_1, respectively. The time differences were related to the wire number and the sums to drift time using look-up tables.

time-difference distributions for each delay line and assigned the boundary between adjacent wires to each valley. Some interaction with the calibration program was allowed in order to correct for situations where the software did not properly assign wire numbers. Such problems typically occurred where few events were available, such as at the delay-line ends, in the shadow of the P_{2L}-P_{2R} gap, or where the peaks from two wires were unusually close together from a defect in the delay line. An error flag was set if the time difference fell outside the proper range for each delay line. After determining the wire number, the position of the wire in the plane was computed. In a similar way, the time sum was converted to a drift distance using a look-up table. This second table was also created in the calibration program and was constructed so that the drift-distance distribution was approximately flat.

For those events with good X and X' information, the next step was to determine whether the drift distance was to the left or right of the wire in each plane. The event was rejected if the difference in wire positions was greater than 12 mm, which was not allowed if the track originated in the vicinity of the target center. The difference $\Delta X_1'$ between the observed and predicted X' position was then computed for the four distance combinations (two planes, left or right side of the wire). The observed X position was corrected for the angle to the observed location in P_2 to give the predicted X' position. The minimum magnitude of $\Delta X_1'$ defined the proper combination, unless $|\Delta X_1'|$ exceeded 2.0 mm, in which case the event was rejected. For events where the drift distances were both to the left or both to the right of the wires, the angle between the X and X' positions was also required to be less than 15.2°. The track was assumed to have passed through P_1 at the average of the X and X' positions and at the average Z of these two planes. A histogram of the final $\Delta X_1'$ distribution is given in Fig. 10.

In order to improve the efficiency of the P_1 chamber, two other classes of events were accepted. If either the X or X' plane had a bad TDC value (zero or overflow) and the other plane had a drift distance less than 1.0 mm, then the P_1 position was taken to be at the wire. Otherwise, information from a good X or X' plane and a good TDC on the other plane was used to reconstruct the value of the bad TDC word. This could be done primarily for events with a large drift distance in the good plane, so that the drift time was small in the bad plane, and it was relatively easy to select which wire had detected the particle. These two classes of events generally accounted for a few percent of all good events.

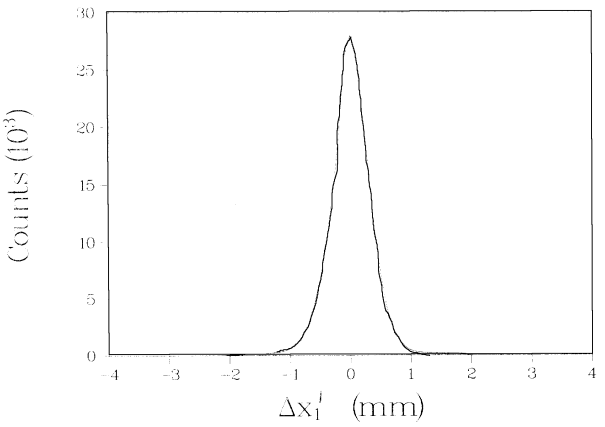

FIG. 10. Histogram of the difference ($\Delta X_1'$) between observed and predicted X' values for P_1. The predicted value corrected the observed X position for angle, assuming the particle trajectory was a straight line from the measured X in P_2. The width of the distribution was ±0.41 mm.

The event was not rejected if both the Y and Y' planes had bad TDC information. Instead, the Y was reconstructed using the Y position in P_2 and the center of the polarized target. If only one of these P_1 planes was good, the track was taken to have the position at the wire, ignoring the drift distance. If both planes were good, Y' was used to resolve the up-down ambiguity in the Y plane using a procedure similar to that described above for the X planes. Since the Y and Y' planes were separated by 211 mm, which is much larger than the 9.53 mm between the X and X' planes, changes in the tests were made. The wire separation distance was required to be less than 25 mm and the $|\Delta Y_1'|$ distance to be less than 15 mm. The track was taken to have passed through the position in the Y plane.

The width of the $\Delta X_1'$ distribution in Fig. 10 indicates a spatial resolution of ±0.29 mm per plane for X and X'. Since most of the reconstructed events had good information in both X and X' planes, the overall P_1 spatial resolution in X was about ±0.21 mm. The resolution in Y was considerably worse. The P_1 reconstruction efficiency was roughly 69–88 % and included only a requirement on the X planes. The probability of good information in both TDC's for the Y plane was often quite low (46–87 %). A number of diagnostic histograms for the four P_1 planes were generated both online and offline to monitor the performance of this chamber.

Using the P_1 and P_2 positions for the events, the target X and Y projections could be calculated. These are shown for spectrometer angles of 10° and 35° in Fig. 11. The laboratory angle distribution is also shown; the "hole" arose from the P_{2L}-P_{2R} gap. For these plots the corrections to positions because of slight misalignment of the spectrometer have been applied. Corrections to the target projections and angles were also made for the effect of the HERA magnetic field on the trajectories using the Monte Carlo program results (see Sec. II D). In the later stages of the data analysis, cuts were applied to the target projections and the data were binned according to c.m. angle. Finally, a straight line was fitted between the P_1 and P_2 positions. The intersection of this line and the vertical center plane of the SCM105 magnet ($Z=0$) was determined. This information was used to assist in the calculation of the P_4 position of the events.

The first major step in the analysis of the P_4 data was to determine the wire location and drift time for each good delay line in the chamber. The P_4 coincidence register bits were used to reconstruct which delay lines corresponded to the TDC words. (No TDC information was

read into the computer for any plane with either more than four coincidence register bits latched or with no bits latched.) Next, the time of arrival at the two ends of each delay line with TDC data was computed using the corresponding calibration constants (see below). Timing corrections for the flight time of the particle through the spectrometer were made by scaling the time from S_1 to S_2 by the ratio of Z distances from S_1 to P_4 and to S_2. A delay line was considered to have bad data and was rejected from further analysis if either time was less than 1 nsec or if a TDC overflow occurred. The difference and sum of the times from the two delay-line ends were then computed. A constant linear relation was used to convert the difference to a wire number within the delay line. Likewise, the time sum was multiplied by a constant to determine the drift distance. The delay-line information was considered bad if the computed wire number was more than one wire spacing below the first or above the 16th wire or if the drift distance was more than half the sense-wire spacing plus 1 mm. The wire number, expressed as an integer, was constrained to fall within the range from 1 to 16 and the drift distance to be between 0 and half the wire spacing. Finally, the wire location was computed from the wire and delay-line numbers plus survey constants.

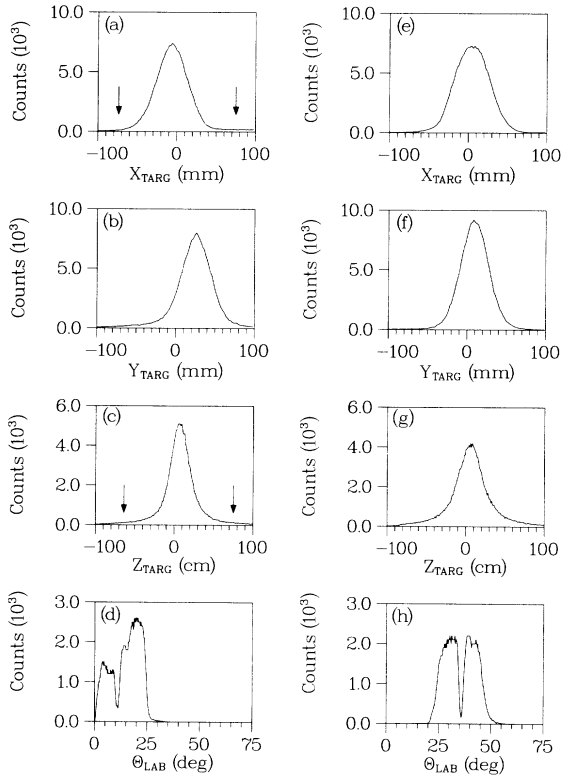

FIG. 11. Histograms of the X, Y, and Z target projections (X_{TARG}, Y_{TARG}, and Z_{TARG}) in the spectrometer coordinate system and the laboratory scattering angle (θ_{lab}). These events were taken at 634 MeV neutron-beam kinetic energy and spectrometer angles of (a)–(d) 10° and (e)–(h) 35°. Small corrections for slight misalignments of the spectrometer have been applied to these histograms, and corrections for the HERA magnetic field have been made to θ_{lab}. Information from chambers P_1 and P_2 was used to compute these quantities. Typical cuts are shown.

The calibration constants to convert TDC channels to times were evaluated with a separate program, assuming a linear relationship. The TDC gains were determined by the conditions that the peak-to-valley ratio in the time-difference histogram were maximized and that the time difference between the 1st and 16th wire be the same for all delay lines. In only one case out of 84 delay-line ends did these gains change during the three years of operation of the magnetic spectrometer. The offset constants were chosen to properly locate the boundaries of each wire number in a valley in the time-difference distribution and to make the time-sum distribution start at about zero. The offsets on about 20% of the TDC channels required infrequent adjustment during the run, although isolated cases of rapid changes were noted in a few instances. The formula to relate time sum to drift distance and additional information on the calibration may be found in Ref. [220].

The second major step in the P_4 analysis involved the determination of the proper wire in each plane. A minimum of three planes with at least one good delay line was required to reconstruct the P_4 position. This requirement guaranteed that at least two independent X and one Y determinations were available. (In the case of only three good planes, with either the U or V plane bad, an ambiguity in the Y coordinate resulted. Except at small scattering angles, this did not affect the scattering angles, since these were computed from P_1 and P_2 as described above.) The proper combination of wires, one in each good plane, was found by minimizing the rms deviation χ_{wire} from a straight line through the point at the center plane of the SCM105 magnet computed from P_1 and P_2. The event was rejected if χ_{wire} was greater than 25 mm for all allowed four- and three-plane wire combinations. Three planes were used only if one plane did not contain a good delay-line signal or if none of the four plane-wire combinations satisfied the constraint on χ_{wire}.

The final major step for the determination of the P_4 position was the resolution of the left-right ambiguities in each plane. First, corrections to the drift distance were applied using the incident particle angle as determined from the previous step. A line was then fit from the point at the SCM105 center plane to each of the 8 (for 3 good planes) or 16 (for 4 good planes) possibilities for the drift distances to the left or right of the sense wires. The fit with the minimum rms deviation χ_{drift} was chosen to give the P_4 position. As before, the event was rejected if χ_{drift} was greater than 5 mm for all allowed three- and four-plane drift combinations. Only if three planes were used to pass the cut on χ_{wire} or if none of the four plane possibilities satisfied the cut on χ_{drift} were three planes used in the fit. Typical plots of χ_{wire} and χ_{drift} are given in Ref. [220]. In the special case that the last wire in one delay line and the adjacent first wire in the next delay line were both present, the drift distances were constrained to be between the two wires.

An estimate of the P_4 spatial resolution can be ob-

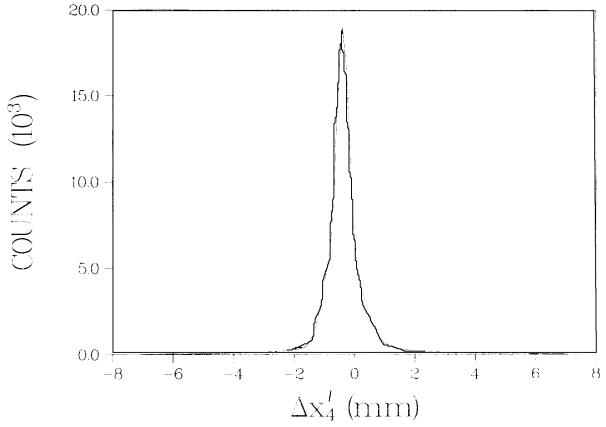

FIG. 12. Histogram of the difference ($\Delta X_4'$) between observed and predicted X' values for P_4. The predicted value corrected the observed X position for angle, assuming the particle trajectory was a straight line from the point at the SCM105 center plane ($Z=0$). This latter point was computed from a straight-line fit to the measured X positions in P_1 and P_2. The width of the distribution was ± 0.82 mm.

tained by computing the difference $\Delta X_4'$ between the observed X' position and the value predicted from X and the slope of the line from the SCM105 center. A histogram of $\Delta X_4'$ is shown in Fig. 12. The width of this histogram indicates a resolution of ± 0.58 mm per plane or an overall P_4 spatial resolution in X of better than ± 0.41 mm, depending on the fraction of three- and four-plane events. The contribution to the spatial resolution from the use of a straight line to the point at the center plane of the SCM105 was estimated to be negligible. The overall reconstruction efficiency for P_4 was approximately 86%, with a loss of about 6% in the first major step in the P_4 analysis. A variety of diagnostic histograms, including time sums and differences, wire numbers, TDC zeros, and TDC overflows, was generated on line and off line to check the P_4 performance. Changes in delay-line calibration constants in particular were easily seen by abrupt changes in the wire-number distributions.

At each spectrometer setting, data were taken with both the SCM105 and HERA magnetic fields turned off. These straight-through runs allowed the chambers to be aligned relative to each other. The P_2 and P_4 positions were taken to be fixed at the survey values, and P_1 offsets for X and Y positions were changed to give the best straight-line fits to these events. Comparison of straight-through data at different spectrometer settings indicated changes of less than 0.4 mm in the P_1 position.

Events that passed the various requirements for chambers P_1, P_2, and P_4, as well as the hodoscope, were written to DST's. The reconstruction efficiency, defined as the number of events on the DST's to the number on the raw tapes, ranged from 31 to 72 %.

D. Kinematical quantities

Once the tracking was completed, the momentum of the particle in the horizontal plane could be computed

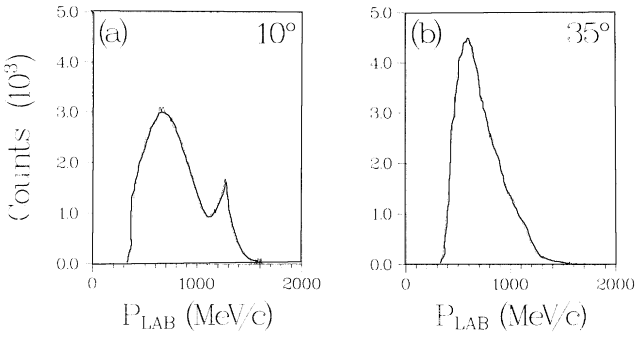

FIG. 13. Histograms of momentum measured in the magnetic spectrometer for a neutron-beam peak energy of 634 MeV at spectrometer angles of $\theta_{lab}=$ (a) 10° and (b) 35°.

from the bend angle in the SCM105 and the magnetic-field integral (see Sec. II D). The total momentum was found by correcting for the Y slope of the trajectory at the entrance to the SCM105. Histograms of momentum for data with a 634-MeV peak-energy neutron beam at spectrometer angles of 10° and 35° are shown in Fig. 13. The low-momentum cutoff was the result of the spectrometer acceptance.

The particle mass could then be computed from the momentum and time of flight from S_1 to S_2; see Fig. 14. Protons and deuterons were always well separated. Generous cuts, as shown in Fig. 14, were typically applied to select protons. Cuts on the target projections were also made to reject events that originated far from the beam center as described in Sec. III C and shown in Fig. 11. Variations in the cuts were studied for their influence on the asymmetries and the signal-to-noise ratio. Negligible effects were observed for variations about the chosen cuts. Only events that passed the cuts were analyzed further.

From the calculated momentum and scattering angle

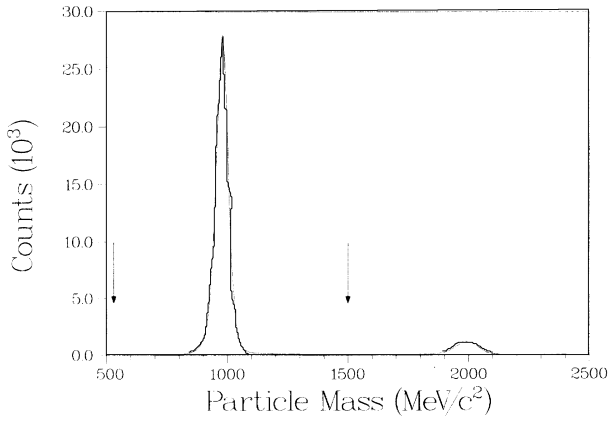

FIG. 14. Histogram of particle mass for a neutron-beam peak energy of 634 MeV at $\theta_{lab}=35°$ as computed from the momentum and time of flight in the spectrometer. Slight errors in the offset timing gave incorrect values for the proton and deuteron masses. The width of the proton peak was ± 38 MeV/c^2. Typical cuts are shown.

in the laboratory, $P_{\rm lab}$ and $\theta_{\rm lab}$, the total recoil-proton energy ($E_{\rm lab}$), and the missing mass (MM) were computed next, where

$$(\mathrm{MM})^2=(\mathbf{P}_{n,\rm in}+\mathbf{P}_{p,\rm in}-\mathbf{P}_{p,\rm out})^2$$
$$=M_n^2-2(E_{\rm lab}-M_p)(E_{n,\rm in}+M_p)$$
$$+2P_{n,\rm in}P_{\rm lab}\cos\theta_{\rm lab}\ ,$$

and $\mathbf{P}$ are four-vectors. In the missing-mass equation, the target was assumed to be a free proton and the incident neutron energy was taken to be the peak energy. The desired elastically scattered events had a missing mass distributed about the neutron mass. Low-energy beam-neutron elastic-scattering events were improperly handled, resulting in missing masses that were too large. Inelastic reactions also gave missing-mass values above the neutron mass. Another source of background resulted from quasielastic scattering and reactions off various nuclei other than hydrogen in the polarized target. Some of these events gave missing-mass values at the neutron mass, as part of a broad continuum.

The laboratory angle was then converted to a c.m. angle $\theta_{\rm c.m.}$ using the peak neutron energy. The events were placed in 5°-wide $\theta_{\rm c.m.}$ bins. Histograms of missing mass for two bins at 484- and 788-MeV peak-energy neutron beams are shown in Figs. 15(a) and 15(c). Background data collected with graphite target beads instead of polarized beads were analyzed in the same way. Missing-mass spectra for the same $\theta_{\rm c.m.}$ bins and beam energy are shown in Figs. 15(b) and 15(d). The elastic signal is clearly visible in the polarized-target data.

The elastic signal in the missing-mass distribution can be used to estimate the spectrometer momentum resolution $\delta P/P$. Typical peak widths were 23, 44, and 40 MeV/c^2 full width at half maximum (FWHM) for proton momenta of 900, 1060, and 1210 MeV/c. Ignoring other contributions, these peak widths correspond to upper limits on the momentum resolution of $\delta P/P \lesssim \pm 1.6\%$, 2.3%, and 1.7%, respectively. (Somewhat poorer missing-mass resolutions were seen at the angles farthest from the SCM105 magnet center.) Sizable contributions to the elastic peak widths also arose from deviations in the measured laboratory scattering angle caused by multiple scattering in the polarized target and S_1 and from slight variations in the SCM105 magnet current during the data taking. However, the estimated [205] width of the peak in the neutron-beam momentum distribution (± 3 MeV) contributed little to the missing-mass peak resolution. Upper limits to $\delta P/P$ can also be derived from the particle-mass widths, ignoring the timing resolution, and give $\delta P/P \lesssim \pm 3\%$ using the measurements described below. Calculated values for $\delta P/P$, based on the measured chamber spatial resolutions in Sec. III C, are $\delta P/P \sim \pm 0.5$–0.7%. Multiple scattering in wire chamber P_2, helium gas, and gas bag windows added significantly to $\delta P/P$ at all angles and beam momenta.

The particle-mass distribution and the estimated momentum resolution can be combined to find the time-of-flight resolution in the spectrometer. Typical proton-mass peak widths were ± 32–44 MeV/c^2. These correspond to timing resolutions $\delta T \lesssim \pm 0.4$ nsec. Such uncertainties are much smaller than required for good spatial resolution in the P_4 drift chamber.

While kinematical quantities could be computed in the first phase of the data analysis, during the production of the DST's, as well as in the second phase, the final cuts and missing-mass histograms discussed in this section

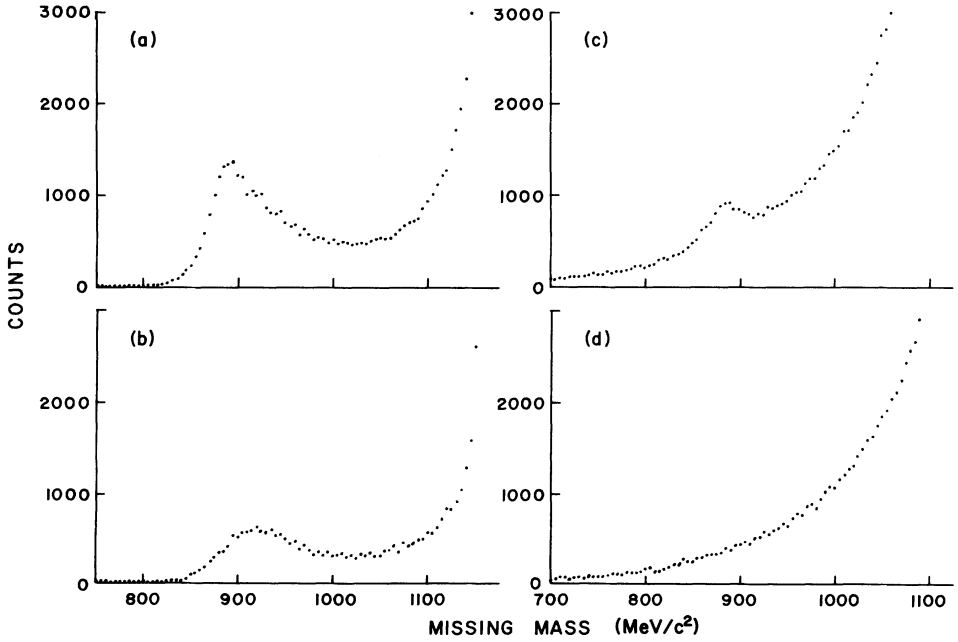

FIG. 15. Missing-mass histograms for (a) polarized target (484 MeV, $\theta_{\rm c.m.}=147.5°$–$152.5°$), (b) graphite target (484 MeV, $\theta_{\rm c.m.}=147.5°$–$152.5°$), (c) polarized target (788 MeV, $\theta_{\rm c.m.}=92.5°$–$97.5°$), and (d) graphite target (788 MeV, $\theta_{\rm c.m.}=92.5°$–$97.5°$).

were generated from the DST's. The time to analyze an event from the raw tapes was roughly a factor of 4 more than from the DST's. Therefore studies of cut positions and the extraction of the final elastic signal were all performed from the DST's.

E. Extraction of the elastic signal

The procedure employed to determine the spin-correlation parameter values is described in this section. Each $\theta_{\text{c.m.}}$ bin was handled separately to extract the number of elastic-scattering events. First, the missing-mass histograms were summed over the pertinent runs for the four combinations of beam- and target-polarization directions. Then the sum $N(+-)+N(-+)$ was normalized by the total beam to the sum $N(++)+(N--)$ by the factor α,

$$\alpha=\frac{MTOT(++)+MTOT(--)}{MTOT(+-)+MTOT(-+)} ,$$

where generally the value of α was within a few percent of 1.00. Next, an estimate of the nonelastic background was found. The carbon background shape C(MM) was multiplied by a linear function f(MM) and subtracted channel by channel from the polarized missing-mass histograms. The coefficients of the linear function were determined from data on each side of the elastic signal; see Figs. 16(a) and 16(b). After the subtraction the elastic-scattering events were clearly distinguishable as in Fig. 16(c). The asymmetry was then computed channel by channel using the background unsubtracted yields in the formula

$$\epsilon=\frac{N(++)+N(--)-\alpha[N(+-)+N(-+)]}{N(++)+N(--)+\alpha[N(+-)+N(-+)]-fC} , \tag{1}$$

and a weighted average was taken to obtain the final asymmetry. Missing-mass channels for which the fitted background counts exceeded the polarized counts were excluded from this weighted average. The error on ϵ was computed from the statistical uncertainties on N and C and from the correlated errors on the coefficients of the linear function f.

Data for the 634 MeV beam energy and a spectrometer angle of 35° were handled differently because no graphite target bead measurements were available. Three different techniques were used to estimate the nonelastic background for these results. The first method was to use "carbon" background measurements at the same angle and energy taken two years later. Various changes had been made to the spectrometer and thus the shape of the carbon missing-mass spectra might be expected to be different. The second technique used the average of the 484- and 788-MeV carbon background shapes. The third method relied on a fit to the background on either side of the elastic peak with a fifth-order polynomial. The error assigned to the final asymmetry included both statistical uncertainties and an additional estimate of the uncertainty in background shape in quadrature. This estimate was half the maximum deviation found from the three techniques above. Note that the nonhydrogen background from the polarized target included other nuclei in addition to the carbon and metal cans surrounding the beads. In particular, ^{3}He and oxygen were present in substantial quantities. The shape of the missing-mass spectra from these nuclei need not agree perfectly with that measured in the graphite bead runs. This may have been one reason that a linear form for f was required instead of a constant. Additional experimental information on this question under somewhat different kinematical conditions is presented in Ref. [219].

Data at 484 and 788 MeV and a spectrometer angle of 10° were also handled somewhat differently. For these

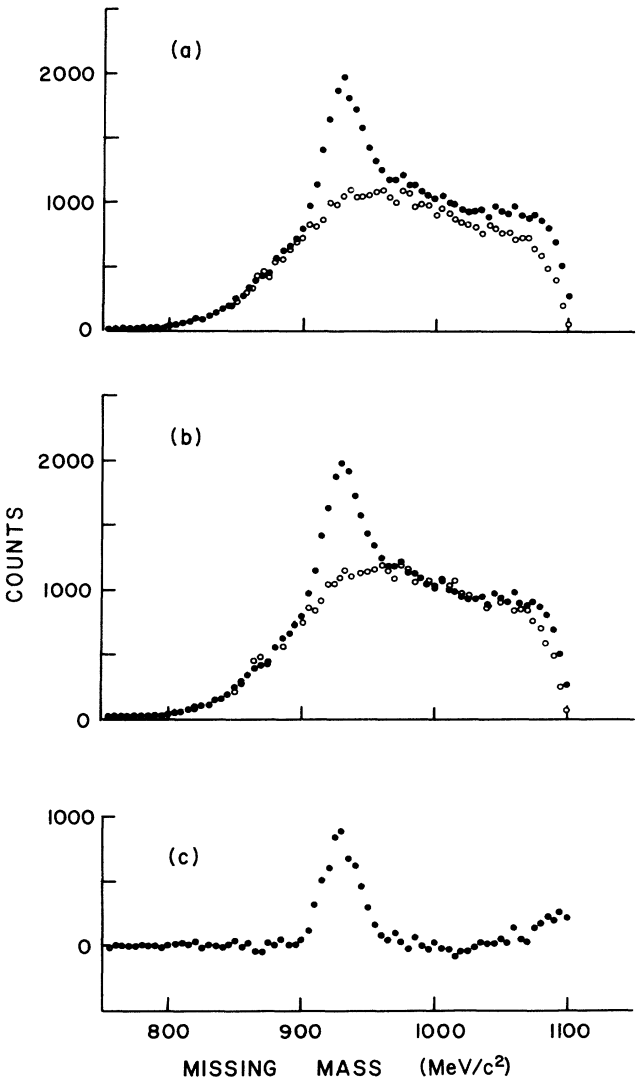

FIG. 16. Missing-mass histograms for 484-MeV peak-energy neutron beam and $\theta_{\text{c.m.}}=122.5°-127.5°$ showing the steps involved in the extraction of the elastic signal: (a) polarized-target data (solid circles) and carbon background data (open circles) multiplied by a constant to show the comparison of the shapes, (b) polarized-target data and carbon background data multiplied by the linear function f described in the text, and (c) the difference between the polarized and background spectra in (b). The elastic events are seen.

TABLE II. Measured *np* elastic-scattering spin observables C_{ij} are tabulated as a function of c.m. angle. The minimum and maximum values of the c.m. angle are denoted $\theta_{\min}$ and $\theta_{\max}$ and the average angle, weighted by the number of observed events, by $\langle \theta_{\text{c.m.}} \rangle$. The coefficients of the pure observables η and λ in Eq. (2) are also shown.

$\theta_{\min}$	$\theta_{\max}$	$\langle \theta_{\text{c.m.}} \rangle$	C_{ij}	δC_{ij}	η	λ
			Kinetic energy=484 MeV			
177.5	180.0	178.4	−1.083	0.116	0.9986	0.0269
172.5	177.5	174.9	−0.941	0.052	0.9986	0.0481
167.5	172.5	170.2	−0.891	0.048	0.9986	0.0522
162.5	167.5	165.1	−0.543	0.060	0.9986	0.0511
157.5	162.5	160.7	−0.284	0.093	0.9986	0.0506
152.5	157.5	154.0	0.306	0.093	0.9986	0.0493
147.5	152.5	150.0	0.380	0.068	0.9986	0.0499
142.5	147.5	145.2	0.676	0.100	0.9986	0.0500
137.5	142.5	140.0	0.594	0.092	0.9986	0.0500
132.5	137.5	135.1	0.582	0.102	0.9986	0.0498
127.5	132.5	130.4	1.106	0.145	0.9986	0.0499
122.5	127.5	126.6	0.525	0.516	0.9986	0.0501
177.5	180.0	178.4	−0.134	0.107	−0.1132	0.4923
172.5	177.5	174.9	0.010	0.067	−0.1132	0.9166
167.5	172.5	170.2	0.100	0.055	−0.1132	0.9918
162.5	167.5	165.1	0.000	0.075	−0.1132	0.9696
157.5	162.5	160.7	−0.204	0.116	−0.1132	0.9606
152.5	157.5	154.0	0.023	0.099	−0.1132	0.9372
147.5	152.5	150.0	0.021	0.076	−0.1132	0.9471
142.5	147.5	145.2	−0.194	0.108	−0.1132	0.9491
137.5	142.5	140.0	−0.161	0.105	−0.1132	0.9512
132.5	137.5	135.1	−0.183	0.115	−0.1132	0.9460
127.5	132.5	130.4	0.097	0.160	−0.1132	0.9481
122.5	127.5	126.6	−0.870	1.080	−0.1132	0.9522
127.5	132.5	128.6	0.821	0.350	0.9986	0.0498
122.5	127.5	124.8	0.939	0.077	0.9986	0.0499
117.5	122.5	120.0	1.001	0.078	0.9986	0.0499
112.5	117.5	115.1	0.763	0.080	0.9986	0.0499
107.5	112.5	110.1	0.711	0.088	0.9986	0.0500
102.5	107.5	105.8	0.646	0.105	0.9986	0.0502
97.5	102.5	99.1	0.456	0.104	0.9986	0.0503
92.5	97.5	95.1	0.549	0.081	0.9986	0.0505
87.5	92.5	90.1	0.474	0.087	0.9986	0.0507
82.5	87.5	85.2	0.405	0.121	0.9986	0.0509
77.5	82.5	80.5	0.461	0.265	0.9986	0.0511
127.5	132.5	128.6	0.239	1.074	−0.1028	0.9460
122.5	127.5	124.8	−0.098	0.096	−0.1028	0.9481
117.5	122.5	120.0	−0.166	0.090	−0.1028	0.9487
112.5	117.5	115.1	0.015	0.089	−0.1028	0.9492
107.5	112.5	110.1	0.000	0.103	−0.1028	0.9502
102.5	107.5	105.8	−0.168	0.117	−0.1028	0.9532
97.5	102.5	99.1	−0.215	0.153	−0.1028	0.9566
92.5	97.5	95.1	−0.181	0.102	−0.1028	0.9599
87.5	92.5	90.1	−0.188	0.113	−0.1028	0.9643
82.5	87.5	85.2	0.008	0.169	−0.1028	0.9680
77.5	82.5	80.5	0.075	0.298	−0.1028	0.9719
127.5	132.5	128.6	−0.761	0.561	−0.1132	0.9449
122.5	127.5	124.8	−0.077	0.098	−0.1132	0.9471
117.5	122.5	120.0	−0.146	0.098	−0.1132	0.9476
112.5	117.5	115.1	0.055	0.108	−0.1132	0.9481
107.5	112.5	110.1	0.060	0.114	−0.1132	0.9491
102.5	107.5	105.8	−0.292	0.156	−0.1132	0.9522
97.5	102.5	99.1	−0.458	0.129	−0.1132	0.9556
92.5	97.5	95.1	−0.201	0.107	−0.1132	0.9588

TABLE II. (*Continued*).

θ_{min}	θ_{max}	$\langle\theta_{c.m.}\rangle$	C_{ij}	δC_{ij}	η	λ
			Kinetic energy=484 MeV			
87.5	92.5	90.1	−0.113	0.119	−0.1132	0.9632
82.5	87.5	85.2	0.023	0.171	−0.1132	0.9669
77.5	82.5	80.5	−0.064	0.311	−0.1132	0.9708
			Kinetic energy=634 MeV			
177.5	180.0	178.4	−0.775	0.128	0.9969	0.0573
172.5	177.5	174.8	−0.945	0.066	0.9969	0.0733
167.5	172.5	170.2	−0.832	0.078	0.9969	0.0731
162.5	167.5	165.2	−0.089	0.086	0.9969	0.0785
157.5	162.5	160.4	0.104	0.132	0.9969	0.0781
152.5	157.5	153.9	0.377	0.162	0.9969	0.0760
147.5	152.5	150.0	0.507	0.077	0.9969	0.0761
142.5	147.5	145.2	0.585	0.083	0.9969	0.0761
137.5	142.5	140.1	0.742	0.099	0.9969	0.0761
132.5	137.5	135.1	0.773	0.114	0.9969	0.0760
127.5	132.5	130.4	0.573	0.159	0.9969	0.0761
122.5	127.5	126.3	0.567	0.320	0.9969	0.0764
177.5	180.0	178.4	−0.146	0.104	0.2317	0.8213
172.5	177.5	174.8	−0.288	0.051	0.2317	0.9715
167.5	172.5	170.2	−0.232	0.052	0.2317	0.8475
162.5	167.5	165.2	−0.134	0.077	0.2317	0.9628
157.5	162.5	160.4	0.048	0.130	0.2317	0.9724
152.5	157.5	153.9	0.119	0.109	0.2317	0.9414
147.5	152.5	150.0	0.239	0.063	0.2317	0.9431
142.5	147.5	145.2	0.153	0.085	0.2317	0.9471
137.5	142.5	140.1	0.058	0.079	0.2317	0.9455
132.5	137.5	135.1	0.252	0.084	0.2317	0.9431
127.5	132.5	130.4	0.189	0.106	0.2317	0.9439
122.5	127.5	126.3	0.035	0.293	0.2317	0.9475
127.5	132.5	128.4	0.264	0.326	0.9992	0.0387
122.5	127.5	124.9	0.624	0.167	0.9992	0.0390
117.5	122.5	120.0	0.724	0.083	0.9992	0.0390
112.5	117.5	115.1	0.815	0.098	0.9992	0.0390
107.5	112.5	110.1	0.793	0.100	0.9992	0.0390
102.5	107.5	105.4	0.618	0.099	0.9992	0.0391
97.5	102.5	99.0	0.731	0.192	0.9992	0.0391
92.5	97.5	95.0	0.640	0.133	0.9992	0.0392
87.5	92.5	90.1	0.492	0.159	0.9992	0.0393
82.5	87.5	85.1	0.571	0.118	0.9992	0.0394
77.5	82.5	80.4	0.425	0.229	0.9992	0.0395
127.5	132.5	128.4	0.007	0.279	0.2317	0.9392
122.5	127.5	124.9	0.296	0.089	0.2317	0.9451
117.5	122.5	120.0	0.400	0.079	0.2317	0.9455
112.5	117.5	115.1	0.117	0.063	0.2317	0.9455
107.5	112.5	110.1	0.198	0.084	0.2317	0.9455
102.5	107.5	105.4	0.162	0.084	0.2317	0.9467
97.5	102.5	99.0	−0.045	0.144	0.2317	0.9467
92.5	97.5	95.0	0.125	0.067	0.2317	0.9493
87.5	92.5	90.1	0.020	0.077	0.2317	0.9519
82.5	87.5	85.1	0.024	0.085	0.2317	0.9546
77.5	82.5	80.4	0.226	0.151	0.2317	0.9571
			Kinetic energy=788 MeV			
172.5	177.5	174.3	−0.313	0.185	−0.1616	0.9789
167.5	172.5	169.2	−0.031	0.219	−0.1616	0.9782

TABLE II. (*Continued*).

θ_{min}	θ_{max}	$\langle\theta_{c.m.}\rangle$	C_{ij}	δC_{ij}	η	λ
			Kinetic energy=788 MeV			
162.5	167.5	165.0	−0.103	0.154	−0.1616	0.9677
157.5	162.5	160.5	0.042	0.225	−0.1616	0.9563
152.5	157.5	154.9	0.081	0.845	−0.1616	0.9320
147.5	152.5	149.8	−0.830	0.418	−0.1616	0.9523
142.5	147.5	145.5	0.069	0.403	−0.1616	0.9575
137.5	142.5	140.1	−1.094	0.306	−0.1616	0.9638
132.5	137.5	134.8	−0.514	0.287	−0.1616	0.9697
127.5	132.5	130.1	−0.391	0.313	−0.1616	0.9635
122.5	127.5	126.5	−1.010	0.537	−0.1616	0.9656
172.5	177.5	174.3	−0.113	0.256	−0.0017	0.9907
167.5	172.5	169.2	−0.160	0.237	−0.0017	0.9970
162.5	167.5	165.0	−0.068	0.185	−0.0017	0.9143
157.5	162.5	160.5	0.136	0.232	−0.0017	0.9171
152.5	157.5	154.9	0.514	0.833	−0.0017	0.9100
147.5	152.5	149.8	0.029	0.495	−0.0017	0.9650
142.5	147.5	145.5	0.342	0.415	−0.0017	0.9711
137.5	142.5	140.1	0.094	0.515	−0.0017	0.9767
132.5	137.5	134.8	0.613	0.368	−0.0017	0.9829
127.5	132.5	130.1	0.548	0.554	−0.0017	0.9736
122.5	127.5	126.5	−1.246	1.080	−0.0017	0.9778
172.5	177.5	174.3	−0.697	0.158	0.9994	−0.0343
167.5	172.5	169.2	−0.541	0.133	0.9994	−0.0349
162.5	167.5	165.0	−0.161	0.121	0.9994	−0.0338
157.5	162.5	160.5	0.381	0.156	0.9994	−0.0335
152.5	157.5	154.9	0.324	0.446	0.9994	−0.0328
147.5	152.5	149.8	0.968	0.347	0.9994	−0.0336
142.5	147.5	145.5	0.600	0.297	0.9994	−0.0339
137.5	142.5	140.1	0.891	0.298	0.9994	−0.0340
132.5	137.5	134.8	0.768	0.251	0.9994	−0.0343
127.5	132.5	130.1	0.943	0.262	0.9994	−0.0340
122.5	127.5	126.5	0.802	0.437	0.9994	−0.0341
167.5	172.5	169.2	−0.328	0.103	0.9921	0.1210
162.5	167.5	165.0	−0.104	0.093	0.9921	0.1217
157.5	162.5	160.5	0.251	0.119	0.9921	0.1214
152.5	157.5	154.9	0.802	0.288	0.9921	0.1184
147.5	152.5	149.8	0.947	0.213	0.9921	0.1210
142.5	147.5	145.5	0.290	0.275	0.9921	0.1223
137.5	142.5	140.1	0.843	0.180	0.9921	0.1223
132.5	137.5	134.8	0.924	0.183	0.9921	0.1231
127.5	132.5	130.1	0.408	0.203	0.9921	0.1222
122.5	127.5	126.5	0.413	0.328	0.9921	0.1225
167.5	172.5	169.2	0.067	0.096	−0.2045	0.9428
162.5	167.5	165.0	0.028	0.081	−0.2045	0.9514
157.5	162.5	160.5	0.002	0.128	−0.2045	0.9502
152.5	157.5	154.9	−0.296	0.346	−0.2045	0.9233
147.5	152.5	149.8	−0.457	0.173	−0.2045	0.9473
142.5	147.5	145.5	−0.097	0.215	−0.2045	0.9568
137.5	142.5	140.1	−0.266	0.167	−0.2045	0.9560
132.5	137.5	134.8	−0.284	0.166	−0.2045	0.9615
127.5	132.5	130.1	−0.194	0.175	−0.2045	0.9542
122.5	127.5	126.5	−0.293	0.337	−0.2045	0.9575
127.5	132.5	128.1	0.183	0.528	0.9965	0.0808
122.5	127.5	125.1	0.437	0.150	0.9965	0.0814
117.5	122.5	119.6	0.562	0.116	0.9965	0.0819
112.5	117.5	114.7	0.729	0.110	0.9965	0.0817

TABLE II. (*Continued*).

θ_{min}	θ_{max}	$\langle\theta_{c.m.}\rangle$	C_{ij}	δC_{ij}	η	λ
			Kinetic energy=788 MeV			
107.5	112.5	109.8	0.772	0.122	0.9965	0.0818
102.5	107.5	105.1	0.835	0.104	0.9965	0.0818
97.5	102.5	100.2	0.732	0.241	0.9965	0.0819
92.5	97.5	94.9	0.749	0.093	0.9965	0.0822
87.5	92.5	90.2	0.838	0.115	0.9965	0.0824
82.5	87.5	85.0	0.548	0.121	0.9965	0.0825
77.5	82.5	80.3	0.547	0.214	0.9965	0.0828
72.5	77.5	75.4	−0.044	0.496	0.9965	0.0830
127.5	132.5	128.1	−0.812	0.509	−0.1633	0.9521
122.5	127.5	125.1	−0.341	0.231	−0.1633	0.9597
117.5	122.5	119.6	−0.022	0.129	−0.1633	0.9661
112.5	117.5	114.7	−0.081	0.127	−0.1633	0.9636
107.5	112.5	109.8	0.071	0.157	−0.1633	0.9643
102.5	107.5	105.1	−0.228	0.118	−0.1633	0.9639
97.5	102.5	100.2	−0.364	0.327	−0.1633	0.9661
92.5	97.5	94.9	−0.353	0.115	−0.1633	0.9688
87.5	92.5	90.2	−0.310	0.184	−0.1633	0.9710
82.5	87.5	85.0	−0.268	0.155	−0.1633	0.9728
77.5	82.5	80.3	−0.511	0.320	−0.1633	0.9757
72.5	77.5	75.4	0.027	0.796	−0.1633	0.9781
127.5	132.5	128.1	−1.188	0.741	0.9969	−0.0757
122.5	127.5	125.1	0.574	0.316	0.9969	−0.0763
117.5	122.5	119.6	0.415	0.176	0.9969	−0.0768
112.5	117.5	114.7	0.693	0.209	0.9969	−0.0766
107.5	112.5	109.8	0.560	0.183	0.9969	−0.0767
102.5	107.5	105.1	0.820	0.195	0.9969	−0.0767
97.5	102.5	100.2	−0.052	0.438	0.9969	−0.0768
92.5	97.5	94.9	0.683	0.174	0.9969	−0.0770
87.5	92.5	90.2	0.874	0.261	0.9969	−0.0772
82.5	87.5	85.0	0.268	0.226	0.9969	−0.0774
77.5	82.5	80.3	−0.170	0.285	0.9969	−0.0776
72.5	77.5	75.4	−0.737	0.785	0.9969	−0.0778
127.5	132.5	128.1	0.521	0.488	−0.0017	0.9650
122.5	127.5	125.1	0.121	0.161	−0.0017	0.9728
117.5	122.5	119.6	0.185	0.139	−0.0017	0.9792
112.5	117.5	114.7	0.226	0.138	−0.0017	0.9767
107.5	112.5	109.8	−0.291	0.144	−0.0017	0.9774
102.5	107.5	105.1	0.127	0.133	−0.0017	0.9770
97.5	102.5	100.2	0.434	0.293	−0.0017	0.9792
92.5	97.5	94.9	−0.154	0.122	−0.0017	0.9820
87.5	92.5	90.2	−0.138	0.145	−0.0017	0.9842
82.5	87.5	85.0	−0.055	0.163	−0.0017	0.9860
77.5	82.5	80.3	−0.106	0.288	−0.0017	0.9890
72.5	77.5	75.4	−0.036	0.611	−0.0017	0.9914
127.5	132.5	128.1	0.768	1.153	0.9921	0.1209
122.5	127.5	125.1	0.629	0.103	0.9921	0.1219
117.5	122.5	119.6	0.508	0.096	0.9921	0.1227
112.5	117.5	114.7	0.635	0.098	0.9921	0.1224
107.5	112.5	109.8	0.741	0.109	0.9921	0.1225
102.5	107.5	105.1	1.137	0.159	0.9921	0.1225
97.5	102.5	100.2	0.726	0.321	0.9921	0.1227
92.5	97.5	94.9	0.957	0.246	0.9921	0.1231
87.5	92.5	90.2	0.751	0.225	0.9921	0.1234
82.5	87.5	85.0	0.287	0.251	0.9921	0.1236
77.5	82.5	80.3	0.221	0.291	0.9921	0.1240
72.5	77.5	75.4	0.414	1.286	0.9921	0.1243

measurements some runs were taken with several of the most beam-left hodoscope counters removed from the trigger to reduce rates from events in the charge-exchange peak. However, the graphite target data did not have these counters removed. As a result, carbon events were rejected in software if one of the removed counters was struck. Then the carbon missing-mass spectra were multiplied by a linear function (f) and subtracted from the polarized spectra. Asymmetries measured with the counters in and with them removed were combined to give final asymmetries. No differences between the two data sets were noted outside statistical errors.

F. Determination of pure spin parameters

In order to obtain the spin-correlation parameters, the asymmetries had to be divided by the beam and target polarizations. The values of $(P_B P_T)^{-1}$ for each run were weighted by *MTOT* and the weighted average computed. Then

$$C_{ij}=\left\langle \frac{1}{P_B P_T} \right\rangle \epsilon = \eta C_{LL} + \lambda C_{SL} \ . \tag{2}$$

The results are given in Table II, along with coefficients (η,λ) of C_{LL} and C_{SL}. These coefficients were calculated from the beam-spin components at JPAN [207], corrected for the effects of the HERA magnetic field on the incoming beam and on the outgoing proton trajectories. The target-spin direction was assumed to be purely L type. Note that C_{NL} is zero by parity conservation. In some cases more than one set of data was taken at the same energy and angle, but with slightly different coefficients for C_{LL} and C_{SL}. These are listed separately in Table II.

Included in the coefficient λ of C_{SL} in Table II is a factor $\cos\langle\phi\rangle$, where $\langle\phi\rangle$ is the average value of the azimuthal angle at the target center for the detected events. The angle ϕ was corrected for the effect of the polarized-target magnetic field on the outgoing proton trajectories and on the incoming neutron-beam spin direction, using the results of the Monte Carlo program described in Sec. II D.

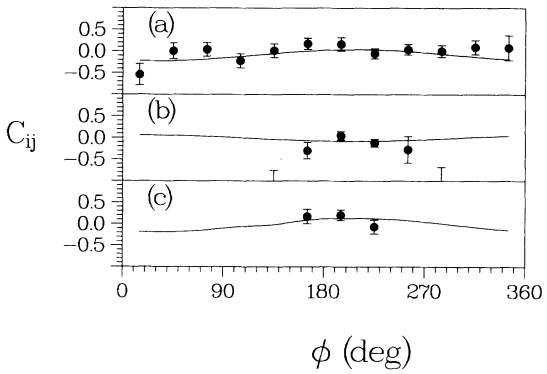

FIG. 17. Values of the mixed spin parameter C_{ij} as a function of the azimuthal angle ϕ at several scattering angles. These results are for the data with small C_{LL} component at (a) 484 MeV, $\theta_{\rm c.m.}=172.5°-177.5°$; (b) 634 MeV, $\theta_{\rm c.m.}=162.5°-167.5°$; and (c) 484 MeV, $\theta_{\rm c.m.}=157.5°-162.5°$. The curves shown were fit to these data in order to extract pure C_{LL} and C_{SL} values. The points in (b) near 130° and 290° are quite negative with large errors; see Table III.

At most angles in Table II, the range of ϕ values accepted is $\pm 6°-15°$. However, for small proton laboratory angles $\theta_{p,\rm lab}\simeq 0$, a much larger range of ϕ values was accepted by the spectrometer. Therefore, at 484 and 634 MeV, the events were separated into 30° bins in ϕ, and a fit was performed in order to derive pure C_{SL} and C_{LL} results. These data are given in Table III, and typical ϕ distributions are shown in Fig. 17. Also included in the figure are fits used to obtain the pure spin parameters. It should be noted that the pure C_{SL} and C_{LL} values obtained from the small angle data in Tables II and III are the same within the statistical errors.

At $\theta_{\rm p,lab}=0°$ or $\theta_{\rm c.m.}=180°$, the number of detected elastically scattered events as a function of ϕ was approximately constant between 0 and 2π, but there were insufficient counts in each ϕ bin to extract reliable C_{ij} values. Thus no C_{SL} results were obtained at $\theta_{\rm c.m.}=180°$. Values of C_{LL} at this angle could be derived, since the coefficient η of C_{LL} in Eq. (2) is independent of ϕ. These data are given in Table II.

The results near $\theta_{p,\rm lab}=0°$ at 788 MeV were also handled differently because many different spin conditions existed for these data, as shown in Table II. As a consequence, there were too few events in each 30° ϕ bin for the individual data sets to obtain reliable C_{ij} values. Instead, the adopted pure spin parameters were derived from the data in Table II. At 484 and 634 MeV, this procedure was shown to give good agreement with results from fits to the ϕ distributions, and this agreement is also expected at 788 MeV.

IV. RESULTS

The final results for the pure spin-correlation parameters C_{LL} and C_{SL} were derived from the values in Tables II and III. These are given in Table IV and Fig. 18. The errors shown are primarily statistical, as described above, and the uncertainties on C_{LL} and C_{SL} are correlated. In addition, there are systematic uncertainties of $\pm 7\%$ for the absolute beam [184,190] and $\pm 3.3\%$ for the absolute target polarization ($\pm 8\%$ overall). The typical uncertainty on the absolute angle is estimated to be $\delta\theta_{\rm c.m.}\sim\pm 0.25°$. Small uncertainties in normalization (see Sec. II B) in Eq. (1) would apply to each set of data in Tables II and III. There are no known angle-dependent systematic errors, such as occur in measurements of outgoing proton spin with carbon polarimeters. The values of χ^2 are also listed when more than two data sets were combined from Table II to give the pure C_{LL} and C_{SL} results.

The final data at 484 and 634 MeV differ somewhat from the preliminary results in Ref. [198], because the data analysis was refined, more events were reconstructed, and additional data runs were analyzed. Finally, in the preliminary data at 484 MeV and a spectrometer angle of 35°, some "C_{SL}" runs had been inadvertently mixed with the "C_{LL}" data. The results presented in Table IV

TABLE III. ϕ distributions of the measured C_{ij} spin observables are tabulated with the coefficients of C_{LL} and C_{SL} in Eq. (2), η and λ, respectively. These distributions are given only for the c.m. angles near 180° and for the 484- and 634-MeV measurements, as described in the text.

$\theta_{\min}$	$\theta_{\max}$	$\langle\theta_{\text{c.m.}}\rangle$	C_{ij}	δC_{ij}	η	λ
			Kinetic energy=484 MeV			
172.5	177.5	174.9	−0.770	0.248	0.9986	−0.0510
172.5	177.5	174.9	−0.617	0.194	0.9986	−0.0501
172.5	177.5	174.9	−0.908	0.238	0.9986	−0.0358
172.5	177.5	174.9	−0.644	0.141	0.9986	−0.0120
172.5	177.5	174.9	−0.830	0.146	0.9986	0.0151
172.5	177.5	174.9	−0.827	0.108	0.9986	0.0382
172.5	177.5	174.9	−0.954	0.125	0.9986	0.0510
172.5	177.5	174.9	−0.913	0.114	0.9986	0.0501
172.5	177.5	174.9	−1.013	0.121	0.9986	0.0358
172.5	177.5	174.9	−0.789	0.135	0.9986	0.0120
172.5	177.5	174.9	−0.660	0.214	0.9986	−0.0151
172.5	177.5	174.9	−0.994	0.261	0.9986	−0.0382
172.5	177.5	174.9	−0.540	0.246	0.1132	0.9673
172.5	177.5	174.9	0.006	0.183	0.1132	0.9512
172.5	177.5	174.9	0.040	0.156	0.1132	0.6801
172.5	177.5	174.9	−0.223	0.163	0.1132	0.2269
172.5	177.5	174.9	0.015	0.159	0.1132	−0.2872
172.5	177.5	174.9	0.174	0.128	0.1132	−0.7243
172.5	177.5	174.9	0.164	0.156	0.1132	−0.9673
172.5	177.5	174.9	−0.054	0.118	0.1132	−0.9512
172.5	177.5	174.9	0.039	0.121	0.1132	−0.6801
172.5	177.5	174.9	0.004	0.138	0.1132	−0.2269
172.5	177.5	174.9	0.089	0.163	0.1132	0.2872
172.5	177.5	174.9	0.078	0.286	0.1132	0.7243
167.5	172.5	170.2	−0.704	0.191	0.9986	−0.0120
167.5	172.5	170.2	−0.877	0.141	0.9986	0.0151
167.5	172.5	170.2	−0.848	0.116	0.9986	0.0382
167.5	172.5	170.2	−0.877	0.093	0.9986	0.0510
167.5	172.5	170.2	−0.887	0.099	0.9986	0.0501
167.5	172.5	170.2	−0.939	0.106	0.9986	0.0358
167.5	172.5	170.2	−0.676	0.194	0.9986	0.0120
167.5	172.5	170.2	0.597	0.390	0.1132	0.6801
167.5	172.5	170.2	0.194	0.249	0.1132	0.2269
167.5	172.5	170.2	−0.246	0.150	0.1132	−0.2872
167.5	172.5	170.2	−0.120	0.134	0.1132	−0.7243
167.5	172.5	170.2	−0.059	0.096	0.1132	−0.9673
167.5	172.5	170.2	−0.147	0.102	0.1132	−0.9512
167.5	172.5	170.2	0.078	0.116	0.1132	−0.6801
167.5	172.5	170.2	−0.150	0.214	0.1132	−0.2269
162.5	167.5	165.1	−0.522	0.342	0.9986	0.0151
162.5	167.5	165.1	−0.561	0.107	0.9986	0.0382
162.5	167.5	165.1	−0.485	0.093	0.9986	0.0510
162.5	167.5	165.1	−0.518	0.110	0.9986	0.0501
162.5	167.5	165.1	−0.744	0.445	0.9986	0.0358
162.5	167.5	165.1	0.037	0.472	0.1132	−0.2872
162.5	167.5	165.1	−0.029	0.124	0.1132	−0.7243
162.5	167.5	165.1	0.086	0.107	0.1132	−0.9673
162.5	167.5	165.1	−0.149	0.142	0.1132	−0.9512
162.5	167.5	165.1	0.528	0.481	0.1132	−0.6801
157.5	162.5	160.7	−0.225	0.136	0.9986	0.0382
157.5	162.5	160.7	−0.244	0.120	0.9986	0.0510
157.5	162.5	160.7	−0.352	0.163	0.9986	0.0501

TABLE III. (*Continued*).

θ_{min}	θ_{max}	$\langle\theta_{c.m.}\rangle$	C_{ij}	δC_{ij}	η	λ
			Kinetic energy=484 MeV			
157.5	162.5	160.7	0.172	0.168	0.1132	−0.7243
157.5	162.5	160.7	0.206	0.123	0.1132	−0.9673
157.5	162.5	160.7	−0.067	0.160	0.1132	−0.9512
			Kinetic energy=634 MeV			
172.5	177.5	174.8	−0.957	0.388	0.9969	−0.0775
172.5	177.5	174.8	−0.672	0.247	0.9969	−0.0732
172.5	177.5	174.8	−0.398	0.305	0.9969	−0.0493
172.5	177.5	174.8	−0.209	0.229	0.9969	−0.0121
172.5	177.5	174.8	−0.487	0.197	0.9969	0.0282
172.5	177.5	174.8	−1.292	0.232	0.9969	0.0611
172.5	177.5	174.8	−1.139	0.173	0.9969	0.0775
172.5	177.5	174.8	−1.088	0.159	0.9969	0.0732
172.5	177.5	174.8	−0.794	0.140	0.9969	0.0493
172.5	177.5	174.8	−0.811	0.143	0.9969	0.0121
172.5	177.5	174.8	−0.608	0.172	0.9969	−0.0282
172.5	177.5	174.8	−0.657	0.215	0.9969	−0.0611
172.5	177.5	174.8	−0.054	0.255	0.2317	−0.9611
172.5	177.5	174.8	−0.094	0.210	0.2317	−0.9076
172.5	177.5	174.8	−0.403	0.247	0.2317	−0.6109
172.5	177.5	174.8	−0.090	0.230	0.2317	−0.1505
172.5	177.5	174.8	−0.361	0.214	0.2317	0.3502
172.5	177.5	174.8	−0.273	0.169	0.2317	0.7571
172.5	177.5	174.8	−0.245	0.143	0.2317	0.9611
172.5	177.5	174.8	−0.226	0.116	0.2317	0.9076
172.5	177.5	174.8	−0.210	0.100	0.2317	0.6109
172.5	177.5	174.8	−0.341	0.126	0.2317	0.1505
172.5	177.5	174.8	−0.079	0.141	0.2317	−0.3502
172.5	177.5	174.8	−0.155	0.218	0.2317	−0.7571
167.5	172.5	170.2	−0.754	0.427	0.9969	−0.0493
167.5	172.5	170.2	−1.349	0.409	0.9969	−0.0121
167.5	172.5	170.2	−0.416	0.276	0.9969	0.0282
167.5	172.5	170.2	−0.337	0.149	0.9969	0.0611
167.5	172.5	170.2	−0.595	0.129	0.9969	0.0775
167.5	172.5	170.2	−0.606	0.116	0.9969	0.0732
167.5	172.5	170.2	−0.862	0.126	0.9969	0.0493
167.5	172.5	170.2	−0.495	0.172	0.9969	0.0121
167.5	172.5	170.2	−1.044	0.602	0.9969	−0.0282
167.5	172.5	170.2	−0.280	0.349	0.2317	−0.6109
167.5	172.5	170.2	−0.273	0.424	0.2317	−0.1505
167.5	172.5	170.2	−0.513	0.196	0.2317	0.3502
167.5	172.5	170.2	−0.344	0.166	0.2317	0.7571
167.5	172.5	170.2	−0.051	0.097	0.2317	0.9611
167.5	172.5	170.2	−0.081	0.087	0.2317	0.9076
167.5	172.5	170.2	−0.277	0.083	0.2317	0.6109
167.5	172.5	170.2	−0.301	0.102	0.2317	0.1505
167.5	172.5	170.2	−0.094	0.457	0.2317	−0.3502
162.5	167.5	165.2	0.336	0.643	0.9969	0.0282
162.5	167.5	165.2	0.053	0.165	0.9969	0.0611
162.5	167.5	165.2	−0.050	0.106	0.9969	0.0775
162.5	167.5	165.2	−0.080	0.112	0.9969	0.0732
162.5	167.5	165.2	−0.006	0.633	0.9969	0.0493
162.5	167.5	165.2	−1.376	0.624	0.2317	0.3502
162.5	167.5	165.2	−0.295	0.189	0.2317	0.7571
162.5	167.5	165.2	0.052	0.098	0.2317	0.9611
162.5	167.5	165.2	−0.119	0.089	0.2317	0.9076

TABLE III. (*Continued*).

θ_{min}	θ_{max}	$\langle\theta_{c.m.}\rangle$	C_{ij}	δC_{ij}	η	λ
			Kinetic energy=634 MeV			
162.5	167.5	165.2	−0.272	0.308	0.2317	0.6109
162.5	167.5	165.2	−1.261	0.583	0.2317	0.1505
157.5	162.5	160.4	−0.016	0.192	0.9969	0.0611
157.5	162.5	160.4	0.102	0.155	0.9969	0.0775
157.5	162.5	160.4	0.291	0.208	0.9969	0.0732
157.5	162.5	160.4	−0.072	0.278	0.2317	0.7571
157.5	162.5	160.4	−0.020	0.139	0.2317	0.9611
157.5	162.5	160.4	0.073	0.137	0.2317	0.9076

supercede the earlier data.

In Ref. [224] a consistency check between various *pp* and *np* elastic-scattering observables at $\theta_{c.m.}=90°$ was derived:

$$C_{LL}(np)=\frac{1}{2}\left\{1-C_{NN}(np)+\frac{1}{4}[C_{NN}(pp)-1+2C_{LL}(pp)]\times\frac{d\sigma/d\Omega(pp)}{d\sigma/d\Omega(np)}\right\}. \quad (3)$$

The right-hand side of the equation above, denoted $C_{LL,calc}$, was evaluated using $C_{NN}(np)$ results from Refs. [173, 225], $C_{NN}(pp)$ from Refs. [194,226–232], $C_{LL}(pp)$ from Refs. [122, 233–235]; $d\sigma/d\Omega(pp)$ from Refs. [187,236–244], and $d\sigma/d\Omega(np)$ from Refs. [159–161]. The adopted values from these experimental data and the corresponding computed results $C_{LL,calc}$ are given in Table V. The measured C_{LL} (90°) values from Table IV show fairly good agreement with $C_{LL,calc}$ at 484 and 634 MeV, but differ by over three standard deviations at 788 MeV. Furthermore, the measured data are all larger than the calculated values.

There are only two independent $I=0$ amplitudes at 90° c.m. Using the set of amplitudes and various equations from Ref. [224], the squares of the two amplitudes are

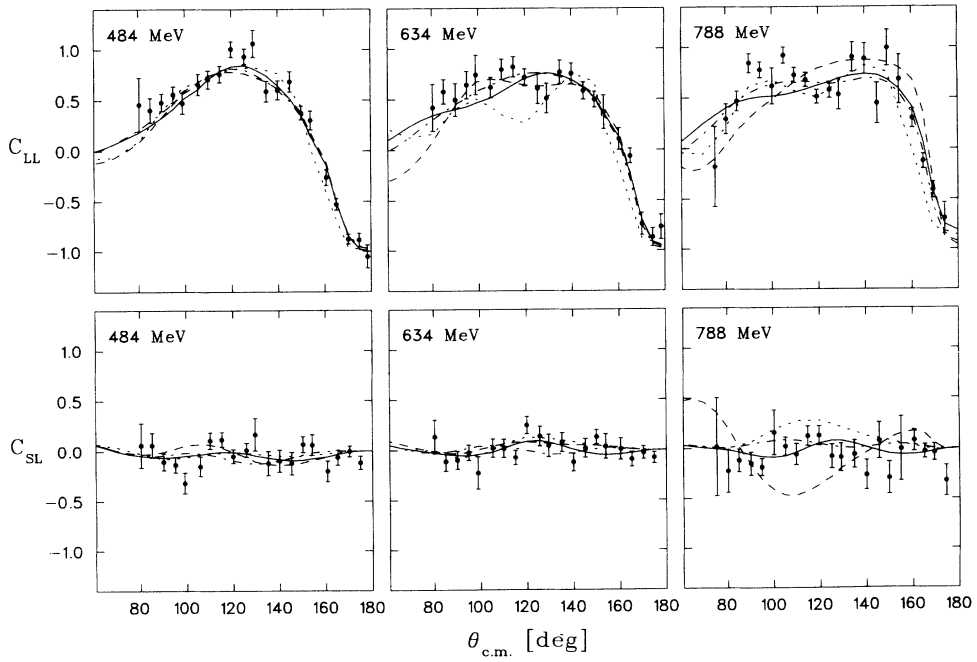

FIG. 18. Final results for the pure spin observables C_{LL} and C_{SL} at (a) 484, (b) 634, and (c) 788 MeV neutron kinetic energy as a function of c.m. scattering angle. The curves are phase shift predictions by Arndt, Hyslop, and Roper [1] (solid curve), Bystricky *et al.* [3] (dashed curve), Bugg [246] (dot-dashed curve), and Hoshizaki *et al.* [247] (dotted curve).

TABLE IV. Final values for C_{LL} and C_{SL} for *np* elastic scattering. Pure *np* elastic-scattering spin observables C_{LL} and C_{SL} were derived from the data in Tables II and III. The quoted errors are statistical uncertainties in quadrature with estimates of uncertainties in extracting the elastic events, as described in the text. The errors on C_{LL} and C_{SL} are slightly correlated, since the pure observables were derived from data with mixed spin components. The last column gives the χ^2 values when the three (five) data sets were combined at 484 (788) MeV to give the two observables C_{LL} and C_{SL}.

$\theta_{\min}$	$\theta_{\max}$	$\langle\theta_{\text{c.m.}}\rangle$	$C_{LL}\pm\delta C_{LL}$	$C_{SL}\pm\delta C_{SL}$	
		Kinetic energy=484 MeV			χ^2(1DF)
177.5	180.0	178.4	−1.051±0.115		
172.5	177.5	174.9	−0.886±0.066	−0.120±0.066	
167.5	172.5	170.2	−0.878±0.047	−0.004±0.055	
162.5	167.5	165.1	−0.530±0.059	−0.066±0.077	
157.5	162.5	160.7	−0.264±0.079	−0.203±0.102	
152.5	157.5	154.0	0.303±0.093	0.061±0.106	
147.5	152.5	150.0	0.377±0.068	0.067±0.080	
142.5	147.5	145.2	0.683±0.100	−0.123±0.114	
137.5	142.5	140.0	0.600±0.092	−0.098±0.110	
132.5	137.5	135.1	0.589±0.102	−0.123±0.121	
127.5	132.5	129.5	1.059±0.134	0.166±0.161	
122.5	127.5	125.7	0.931±0.076	0.011±0.072	0.05
117.5	122.5	120.0	1.005±0.078	−0.051±0.070	0.05
112.5	117.5	115.1	0.758±0.080	0.118±0.073	0.12
107.5	112.5	110.1	0.706±0.088	0.108±0.081	0.19
102.5	107.5	105.8	0.655±0.105	−0.150±0.098	0.36
97.5	102.5	99.1	0.473±0.104	−0.320±0.103	1.42
92.5	97.5	95.1	0.557±0.081	−0.136±0.077	0.01
87.5	92.5	90.1	0.480±0.087	−0.105±0.085	0.24
82.5	87.5	85.2	0.402±0.121	0.061±0.124	0.01
77.5	82.5	80.5	0.459±0.264	0.060±0.222	0.10
		Kinetic energy=634 MeV			
177.5	180.0	178.4	−0.766±0.123		
172.5	177.5	174.8	−0.870±0.090	−0.079±0.056	
167.5	172.5	170.2	−0.736±0.111	−0.028±0.065	
162.5	167.5	165.2	−0.061±0.073	−0.096±0.075	
157.5	162.5	160.4	0.108±0.107	0.008±0.107	
152.5	157.5	153.9	0.376±0.166	0.034±0.125	
147.5	152.5	150.0	0.499±0.079	0.131±0.071	
142.5	147.5	145.2	0.585±0.085	0.018±0.094	
137.5	142.5	140.1	0.754±0.101	−0.123±0.089	
132.5	137.5	135.1	0.769±0.117	0.078±0.095	
127.5	132.5	129.4	0.510±0.146	0.044±0.113	
122.5	127.5	125.6	0.609±0.150	0.137±0.099	
117.5	122.5	120.0	0.715±0.084	0.248±0.087	
112.5	117.5	115.1	0.819±0.099	−0.077±0.072	
107.5	112.5	110.1	0.793±0.101	0.015±0.093	
102.5	107.5	105.4	0.618±0.100	0.020±0.093	
97.5	102.5	99.0	0.741±0.194	−0.229±0.161	
92.5	97.5	95.0	0.641±0.134	−0.025±0.078	
87.5	92.5	90.1	0.496±0.161	−0.100±0.091	
82.5	87.5	85.1	0.576±0.119	−0.115±0.094	
77.5	82.5	80.4	0.420±0.231	0.134±0.169	
		Kinetic energy=788 MeV			χ^2(3DF)
172.5	177.5	174.3	−0.696±0.158	−0.323±0.154	1.00
167.5	172.5	169.2	−0.410±0.081	−0.040±0.087	2.03
162.5	167.5	165.0	−0.126±0.073	−0.030±0.071	0.73
157.5	162.5	160.5	0.297±0.094	0.080±0.106	0.60
152.5	157.5	154.9	0.678±0.241	−0.005±0.321	1.47
147.5	152.5	149.8	0.988±0.180	−0.297±0.161	1:30
142.5	147.5	145.5	0.443±0.200	0.075±0.181	1.21

TABLE IV. (*Continued*).

θ_{min}	θ_{max}	$\langle\theta_{c.m.}\rangle$	$C_{LL}\pm\delta C_{LL}$	$C_{SL}\pm\delta C_{SL}$	
		Kinetic energy=788 MeV			χ^2(3DF)
137.5	142.5	140.1	0.881±0.153	−0.267±0.147	6.66
132.5	137.5	134.8	0.899±0.147	−0.061±0.139	4.91
127.5	132.5	129.1	0.529±0.148	−0.091±0.142	4.18/6.74
122.5	127.5	125.1	0.576±0.079	−0.082±0.122	2.26/2.86
117.5	122.5	119.6	0.508±0.068	0.126±0.096	0.81
112.5	117.5	114.7	0.676±0.069	0.121±0.096	1.55
107.5	112.5	109.8	0.722±0.075	−0.063±0.108	6.16
102.5	107.5	105.1	0.918±0.079	0.019±0.091	4.18
97.5	102.5	100.2	0.615±0.177	0.156±0.223	5.04
92.5	97.5	94.9	0.773±0.078	−0.192±0.085	1.32
87.5	92.5	90.2	0.842±0.095	−0.155±0.116	0.13
82.5	87.5	85.0	0.469±0.098	−0.122±0.114	2.22
77.5	82.5	80.3	0.292±0.148	−0.227±0.216	5.23
72.5	77.5	75.4	−0.180±0.399	0.014±0.489	0.79

$$|\phi_{\tau,0}|^2=\left[C_{LL}\frac{d\sigma}{d\Omega}\right]_{I=0}(90°)$$
$$=4\left[C_{LL}\frac{d\sigma}{d\Omega}\right]_{np}(90°)-\left[C_{LL}\frac{d\sigma}{d\Omega}\right]_{pp}(90°), \quad (4)$$

$$|\phi_{5,0}|^2=\frac{1}{2}\left[(1-C_{LL})\frac{d\sigma}{d\Omega}\right]_{I=0}(90°)$$
$$=2\left[(1-C_{LL})\frac{d\sigma}{d\Omega}\right]_{np}(90°)$$
$$-\frac{1}{2}\left[(1-C_{LL})\frac{d\sigma}{d\Omega}\right]_{pp}(90°). \quad (5)$$

These quantities are given in Table VI, using numerical values from Table V as inputs. The computed $|\phi_{\tau,0}|^2$ are all positive, but $|\phi_{5,0}|^2$ are all negative or consistent with zero. Note that the requirements that $|\phi_{\tau,0}|^2$ and $|\phi_{5,0}|^2$ be non-negative or equivalently that

$$1\geq C_{LL,I=0}(90°)\geq 0$$

can be considered as a different test of consistency of the *np* and *pp* measurements. This test has failed by over three standard deviations at 788 MeV, suggesting again that the measured C_{LL} (90°) values for *np* elastic scattering are too large compared to other data.

Recent measurements [196,205] at LAMPF suggest that the true spin-transfer parameter K_{LL} values are about a factor of 1.12 larger in magnitude than those in Refs. [184,190]. A similar conclusion was reached [245,246] from an analysis of the existing *np* free- and quasifree-scattering data. However, there are some minor differences between the beam for this experiment and that for the new K_{LL} results. These include different collimator diameters and the presence or absence of a lead plug to convert γ rays in the beam. Additional measurements and calculations are planned to determine the appropriate spin-transfer parameter to use for this series of experiments.

An increase in the magnitude of K_{LL} and K_{NN} would lead to improved agreement in the consistency tests of Tables V and VI. Alternatively, the data in these tables can be used to estimate the ratio R of true K_{LL} values to the results from Refs. [184,190]. Assuming that R is independent of energy and that $|\phi_{5,0}|^2$ is zero in Eq. (5), then $\langle R\rangle=1.37\pm0.14$, compared with the value of 1.12 suggested in Refs. [196,205]. Likewise, assuming the measured and calculated C_{LL} (90°) in Eq. (3) and Table V

TABLE V. Consistency of 90° c.m. data. The values of differential cross sections and spin observables used in the consistency check of Eq. (3) are given.

	T_n=484 MeV	634 MeV	788 MeV
C_{NN} (*np*)	+0.15±0.07	+0.15±0.06	−0.05±0.09
C_{NN} (*pp*)	+0.48±0.02	+0.66±0.03	+0.67±0.02
C_{LL} (*pp*)	+0.14±0.02	+0.21±0.02	+0.19±0.02
$d\sigma/d\Omega$ (*pp*)	3.48±0.08 mb/sr	2.34±0.03 mb/sr	1.10±0.02mb/sr
$d\sigma/d\Omega$ (*np*)	1.26±0.03 mb/sr	0.83±0.04 mb/sr	0.46±0.03 mb/sr
$C_{LL,calc}$(*np*)	+0.34±0.04	+0.45±0.04	+0.54±0.05
C_{LL} (*np*)	+0.480±0.087	+0.496±0.161	+0.842±0.095

TABLE VI. Computed squares of magnitudes of $I=0$ amplitudes at 90° c.m. The squares of the two nonzero amplitudes $\phi_{\tau,0}$ and $\phi_{5,0}$ from Ref. [224] are tabulated. These results were computed using Eqs. (4) and (5) and data in Table V.

Beam energy	$\lvert\phi_{\tau,0}\rvert^2$	$\lvert\phi_{5,0}\rvert^2$
484 MeV	1.93±0.45 mb/sr	−0.19±0.23 mb/sr
634 MeV	1.16±0.54 mb/sr	−0.09±0.27 mb/sr
788 MeV	1.34±0.20 mb/sr	−0.30±0.09 mb/sr

are equal, then $\langle R \rangle = 1.43 \pm 0.16$. If the weighted average of C_{LL} over the angular range $\theta_{\text{c.m.}}$ 82.5°–97.5° was used instead of the value for $\theta_{\text{c.m.}} = 87.5°–92.5°$, then $\langle R \rangle = 1.31 \pm 0.09$ and 1.34 ± 0.11, respectively. The values of $\langle R \rangle$ are all approximately two standard deviations from 1.12, but three standard deviations from 1.00.

The pure spin observables C_{LL} and C_{SL} are compared with recent phase-shift analysis predictions in Fig. 18. These predictions include the SM89 PSA solution of Arndt, Hyslop, and Roper [1], solutions in two different energy ranges of the Saclay-Geneva group [3], and the recent solutions of Bugg [246] and Higuchi *et al.* [247]. The poorest fits are seen to occur at the highest energy, as might be expected. Values of the χ^2 per degree of freedom (χ^2/N_{DF}) for the comparison of each prediction with the data are given in Table VII. In addition, χ^2/N_{DF} is tabulated for the C_{LL} results renormalized by a factor of 1.12, corresponding to the new K_{LL} measurements [196,205]. The C_{SL} data are all too small in magnitude to have significant changes in χ^2/N_{DF} by this renormalization.

The only other published results for the spin observables measured in this experiment are for $C_{LL}(np)$ at 630 MeV [172]. A comparison of C_{LL} data from the two experiments shows excellent agreement; see Fig. 19. The prediction for C_{LL} [248] from the Argonne potential model [27] is also given in Fig. 19. The average χ^2/N_{DF} for the comparison between the prediction of this model and the C_{SL} and C_{LL} data at all three energies is 2.7, which is comparable to the average χ^2/N_{DF} for all the phase-shift analysis results given in Table VII.

TABLE VII. Values of χ^2 per degree of freedom for various phase-shift predictions compared with the data in Table IV. The Bugg solution at 634 MeV is an interpolation of the results in Ref. [246] by Arndt, Hyslop, and Roper [1].

	Arndt, Hyslop, and Roper [1]	Bugg [246]	Saclay-Geneva [3]	Hoshizaki *et al.* [247]
484 MeV				
C_{SL}	1.50	2.04	2.18	1.40
C_{LL}	1.53	1.56	1.98	2.49
$C_{LL}/1.12$	1.74	1.54	2.06	4.49
634 MeV				
C_{SL}	1.13	1.50	1.19	1.13
C_{LL}	1.43	1.26	1.29	7.25
$C_{LL}/1.12$	1.76	2.07	1.72	7.96
788 MeV				
C_{SL}	1.15	1.54	6.84	3.42
C_{LL}	3.86	2.35	9.18	4.22
$C_{LL}/1.12$	3.39	2.39	10.66	4.38

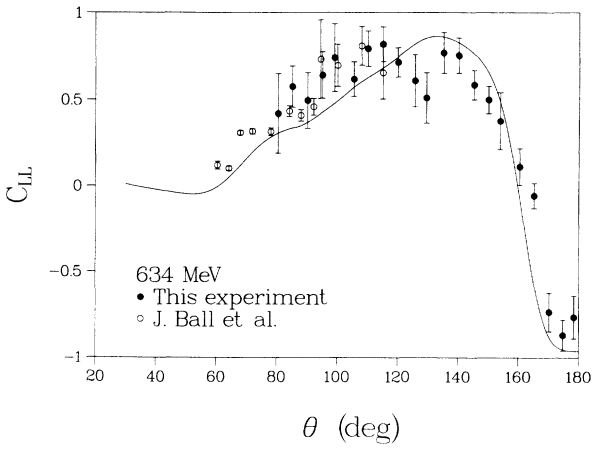

FIG. 19. Comparison of the $C_{LL}(np)$ data at 634 MeV as a function of c.m. angle from this experiment and data at 630 MeV from Ball *et al.* [172]. The curve is the prediction of Lee [248] from the Argonne potential model [27].

V. CONCLUSIONS

Final results are presented for *np* elastic-scattering spin observables C_{SL} and C_{LL} with *S*- and *L*-type polarized neutron beam incident on an *L*-type polarized proton target. The outgoing protons were detected in a large-acceptance magnetic spectrometer with momentum resolution $\delta P/P \lesssim \pm 2.0\%$ and good time-of-flight resolution. Elastic-scattering events were selected on the basis of the projected interaction point at the target and the missing mass, after estimation of backgrounds from data with carbon beads replacing the normal propanediol polarized-target material. These results include additional runs and events at 484 and 634 MeV compared to the preliminary data [198] and additional measurements at 788 MeV.

The final results for "mixed" spin observables are given in Tables II and III and for the derived pure spin parameters in Table IV and Fig. 18. The quoted uncertainties contain statistical errors in quadrature with estimates of uncertainties from the nonelastic backgrounds. In addition, there are systematic uncertainties associated with knowledge of the absolute beam (±7%) and target (±3.3%) polarization that apply to the data sets in Table II as a whole.

However, there is evidence that the beam polarization is in error by roughly 12% based on recent measurements [196,205] of the spin-transfer parameter K_{LL}. Additional experiments and calculations to determine the true beam normalization are planned. If a renormalization is necessary, the corrected results will be presented in the paper describing the final data for the measurements in Refs. [174,219].

A comparison of the pure spin observables C_{SL} and

C_{LL} to various phase-shift analysis predictions [1,3,246,247] is given in Fig. 18 and Table VII. The preliminary data from this experiment are included in the databases for these phase-shift analyses. Sizable differences are apparent, especially at 788 MeV. These results add significantly to the goal of determining the $I=0$ amplitudes up to 800 MeV.

ACKNOWLEDGMENTS

We gratefully acknowledge L. Rosen and the LAMPF staff for assistance with all aspects of this experiment. In particular, we thank D. Hagerman, O. van Dyck, M. McNaughton, and the operations staff for help with the polarized proton beam; J. Novak, N. Hoffman and the cryogenics staff for assistance with the LD_2 target, superconducting solenoid, and helium liquifier; L. Agnew, R. Werbeck, J. Gomez, and the experimental facilities staff for help with construction and operation of the experimental apparatus; G. Gonzales, G. Suazo, and the machine shop staff for assistance with construction of detector and magnet supports; R. Harrison, J. Cordova, and E. Weiler for surveying the apparatus; J. Harrison, T. Kozlowski, M. Oothoudt, and the staff at the LAMPF Data Analysis Center for assistance with on-line and off-line computing; W. Haberichter and A. Rask for assistance with the MWPC's; F. Montoya and A. Rask for help with the scintillation counters; T. Hunter for assistance with mapping the SCM105 magnetic field; and R. Sena, R. Richardson, and the LEEP staff for help with repairs of various electronic components and modules. We are especially indebted to J. E. Simmons and M. McNaughton for advice on the polarized neutron beam; T. Kasprzyk, J. Estes, W. Coulter, K. Graham, and D. Yeamans for assistance with the polarized-target operation; R. Arndt, D. Bugg, N. Hoshizaki, T. S. H. Lee, and F. Lehar for information on their phase-shift analysis results and model predictions; and D. Grosnick for a careful reading of the manuscript. This experiment was supported in part by the U.S. Department of Energy, Contracts Nos. W-31-109-ENG-38 and DE-AS05-76ER04449 and Grants Nos. DE-FG05-88ER40399 and DE-FG04-88ER40403, and by Associated Western Universities.

[1] R. A. Arndt, J. S. Hyslop, and L. D. Roper, Phys. Rev. D **35**, 128 (1987).
[2] N. Hoshizaki, Prog. Theor. Phys. **60**, 1796 (1978); **61**, 129 (1979); K. Hashimoto, Y. Higuchi, and N. Hoshizaki, *ibid.* **64**, 1678 (1980); K. Hashimoto and N. Hoshizaki, *ibid.* **64**, 1693 (1980).
[3] J. Bystricky, C. Lechanoine-Leluc, and F. Lehar, J. Phys. (Paris) **48**, 199 (1987); C. Lechanoine-Leluc, F. Lehar, P. Winternitz, and J. Bystricky, *ibid.* **48**, 985 (1987).
[4] R. Dubois, D. Axen, R. Keeler, M. Comyn, G. A. Ludgate, J. R. Richardson, N. M. Stewart, A. S. Clough, D. V. Bugg, and J. A. Edgington, Nucl. Phys. **A377**, 554 (1982).
[5] M. I. Dzhgarkava, Yu. M. Kazarinov, I. Strakhota, and M. R. Khayatov, Yad. Fiz. **35**, 65 (1982) [Sov. J. Nucl. Phys. **35**, 39 (1982)].
[6] R. A. Arndt, Phys. Rev. D **37**, 2665 (1988).
[7] F. Shimizu, Y. Kubota, H. Koiso, F. Sai, S. Sakamoto, and S. S. Yamamoto, Nucl. Phys. **A386**, 571 (1982); **A389**, 445 (1982).
[8] B. J. VerWest and R. A. Arndt, Phys. Rev. C **25**, 1979 (1982).
[9] J. Bystricky, P. LaFrance, F. Lehar, F. Perrot, T. Siemiarczuk, and P. Winternitz, J. Phys. (Paris) **48**, 1901 (1987).
[10] P. Cziffra, M. H. MacGregor, M. J. Moravcsik, and H. P. Stapp, Phys. Rev. **114**, 880 (1959).
[11] G. Breit, M. H. Hull, K. E. Lassila, and K. D. Pyatt, Phys. Rev. **120**, 2227 (1960); G. Breit, Rev. Mod. Phys. **34**, 766 (1962).
[12] A. Scotti and D. Y. Wong, Phys. Rev. **138B**, 145 (1965).
[13] A. E. S. Green and T. Sawada, Rev. Mod. Phys. **39**, 594 (1967).
[14] R. Tamagaki, Rev. Mod. Phys. **39**, 629 (1967).
[15] K. Erkelenz, Phys. Rep. C **13**, 191 (1974).
[16] R. de Tourreil, B. Rouben, and D. W. L. Sprung, Nucl. Phys. **A242**, 445 (1975).
[17] K. Holinde and R. Machleidt, Nucl. Phys. **A256**, 479 (1976); **A256**, 497 (1976).
[18] M. M. Nagels, T. A. Rijken, and J. J. de Swart, Phys. Rev. D **17**, 768 (1978); **20**, 1633 (1979).
[19] J. Fleischer and J. A. Tjon, Phys. Rev. D **21**, 87 (1980).
[20] M. H. Partovi and E. L. Lomon, Phys. Rev. D **2**, 1999 (1970); F. Partovi and E. L. Lomon, *ibid.* **5**, 1192 (1972); E. L. Lomon, *ibid.* **14**, 2402 (1976); **22**, 229 (1980).
[21] M. Chemtob, J. W. Durso, and D. O. Riska, Nucl. Phys. **B38**, 141 (1972); A. D. Jackson, D. O. Riska, and B. VerWest, Nucl. Phys. **A249**, 397 (1975).
[22] W. N. Cottingham, M. Lacombe, B. Loiseau, J. M. Richard, and R. Vinh Mau, Phys. Rev. D **8**, 800 (1973).
[23] G. E. Bohannon and P. Signell, Phys. Rev. D **10**, 815 (1974).
[24] G. N. Epstein and B. H. J. McKellar, Phys. Rev. D **10**, 1005 (1974).
[25] M. Lacombe, B. Loiseau, J.-M. Richard, R. Vinh Mau, J. Cote, P. Pires, and R. de Tourreil, Phys. Rev. D **12**, 1495 (1975); Phys. Rev. C **21**, 861 (1980).
[26] R. Machleidt, K. Holinde, and Ch. Elster, Phys. Rep. **149**, 1 (1987); Ch. Elster, W. Ferchländer, K. Holinde, D. Schütte, and R. Machleidt, Phys. Rev. C **37**, 1647 (1988).
[27] M. Betz and T.-S. H. Lee, Phys. Rev. C **23**, 375 (1981); T.-S. H. Lee, Phys. Rev. Lett. **50**, 1571 (1983); Phys. Rev. C **29**, 195 (1984); T.-S. H. Lee and A. Matsuyama, *ibid.* **32**, 1986 (1985); **36**, 1459 (1987).
[28] E. L. Lomon and H. Feshbach, Ann. Phys. (N.Y.) **48**, 94 (1968); E. L. Lomon, Phys. Rev. D **26**, 576 (1982); **31**, 1746 (1985); P. Gonzalez and E. L. Lomon, *ibid.* **34**, 1351 (1986).
[29] A. M. Green, J. A. Niskanen, and M. E. Sainio, J. Phys. G **4**, 1055 (1978); A. M. Green and M. E. Sainio, *ibid.* **5**, 503 (1979); **8**, 1337 (1982).
[30] W. Grein and P. Kroll, Nucl. Phys. **A338**, 332 (1980).
[31] W. M. Kloet and R. R. Silbar, Phys. Rev. Lett. **45**, 970 (1980); Nucl. Phys. **A338**, 281 (1980); **A426**, 625(E) (1984); **A338**, 317 (1980); **A364**, 346 (1981).
[32] M. Araki, Y. Koike, and T. Ueda, Prog. Theor. Phys. **63**,

335 (1980); Nucl. Phys. **A389**, 605 (1982); M. Araki and T. Ueda, *ibid.* **A379**, 449 (1982); T. Ueda, Phys. Lett. **141B**, 157 (1984); Phys. Lett. B **175**, 19 (1986); Prog. Theor. Phys. **76**, 729 (1986); **76**, 959 (1986).
[33] E. E. van Faassen and J. A. Tjon, Phys. Rev. C **28**, 2354 (1983); **30**, 285 (1984); **33**, 2105 (1986).
[34] I. Hulthage and F. Myhrer, Phys. Rev. C **30**, 298 (1984).
[35] W. M. Kloet and J. A. Tjon, Phys. Rev. C **30**, 1653 (1984).
[36] G. H. Lamot, J. L. Perrot, C. Fayard, and T. Mizutani, Phys. Rev. C **35**, 239 (1987); T. Mizutani, B. Saghai, C. Fayard, and G. H. Lamot, *ibid.* **35**, 667 (1987).
[37] A. Jackson, A. D. Jackson, and V. Pasquier, Nucl. Phys. **A432**, 567 (1985); A. Jackson, A. D. Jackson, A. S. Goldhaber, G. E. Brown, and L. C. Castillejo, Phys. Lett. **154B**, 101 (1985).
[38] H. Yabu and K. Ando, Prog. Theor. Phys. **74**, 750 (1985); H. Yabu, B. Schwesinger, and G. Holzwarth, Phys. Lett. B **224**, 25 (1989).
[39] R. Vinh Mau, M. Lacombe, B. Loiseau, W. N. Cottingham, and P. Lisboa, Phys. Lett. **150B**, 259 (1985).
[40] J. M. Eisenberg, A. Erell, and R. R. Silbar, Phys. Rev. C **33**, 1531 (1986); G. Kälbermann and J. M. Eisenberg, Nucl. Phys. **A500**, 589 (1989).
[41] T. Otofuji, S. Saito, M. Yasuno, T. Kurihara, and H. Kanada, Phys. Rev. C **34**, 1559 (1986).
[42] A. dePace, H. Müther, and A. Faessler, Nucl. Phys. **A457**, 541 (1986).
[43] H. Odawara, O. Morimatsu, and K. Yazaki, Phys. Lett. B **175**, 115 (1986).
[44] E. M. Nyman and D. O. Riska, Phys. Lett. B **175**, 392 (1986); **183**, 7 (1987); **203**, 13 (1988).
[45] E. Braaten, Phys. Rev. D **37**, 2026 (1988).
[46] N. S. Manton, Phys. Rev. Lett. **60**, 1916 (1988).
[47] N. Kaiser and U. G. Meissner, Phys. Lett. B **233**, 457 (1989).
[48] T. S. Walhout and J. Wambach, Phys. Rev. Lett. **67**, 314 (1991).
[49] I. Zahed and G. E. Brown, Phys. Rep. **142**, 1 (1986).
[50] W. A. Bardeen, M. S. Chanowitz, S. D. Drell, M. Weinstein, and T.-M. Yan, Phys. Rev. D **11**, 1094 (1975).
[51] T. DeGrand, R. L. Jaffe, K. Johnson, and J. Kiskis, Phys. Rev. D **12**, 2060 (1975).
[52] D. A. Liberman, Phys. Rev. D **16**, 1542 (1977).
[53] C. DeTar, Phys. Rev. D **17**, 323 (1978).
[54] D. Robson, Nucl. Phys. **A308**, 381 (1978).
[55] V. A. Matveev and P. Sorba, Nuovo Cimento A **45**, 257 (1978).
[56] I. T. Obukhovsky, V. G. Neudatchin, Yu. F. Smirnov, and Yu. M. Tchuvil'sky, Phys. Lett. **88B**, 231 (1979).
[57] C. S. Warke and R. Shanker, Phys. Rev. C **21**, 2643 (1980).
[58] M. Oka and K. Yazaki, Phys. Lett. **90B**, 41 (1980); Prog. Theor. Phys. **66**, 556 (1981); **66**, 572 (1981); Nucl. Phys. **A402**, 477 (1983); O. Morimatsu, K. Yazaki, and M. Oka, *ibid.* **A424**, 412 (1984).
[59] M. Harvey, Nucl. Phys. **A352**, 301 (1981); **A352**, 326 (1981); M. Harvey, J. LeTourneux, and B. Lorazo, *ibid.* **A424**, 428 (1984).
[60] A. Faessler, F. Fernandez, G. Lübeck, and K. Shimizu, Phys. Lett. **112B**, 201 (1982); Nucl. Phys. **A402**, 555 (1983); A. Faessler and F. Fernandez, Phys. Lett. **124B**, 145 (1983); K. Bräuer, A. Faessler, F. Fernandez, and K. Shimizu, Z. Phys. A **320**, 609 (1985); Nucl. Phys. **A507**, 599 (1990); Z.-Y. Zhang, K. Bräuer, A. Faessler, and K. Shimizu, *ibid.* **A443**, 557 (1985); Th. Pfenninger and A. Faessler, *ibid.* **A484**, 476 (1988).
[61] K. Maltman and N. Isgur, Phys. Rev. D **29**, 952 (1984).
[62] F. C. Chang, Nucl. Phys. **A432**, 555 (1985).
[63] Y. Fujiwara and K. T. Hecht, Nucl. Phys. **A444**, 541 (1985); **A451**, 625 (1986); **A456**, 669 (1986); **A462**, 621 (1987); Phys. Lett. B **171**, 17 (1986).
[64] Yu. S. Kalashnikova, I. M. Narodetskii, Yu. A. Simonov, and A. I. Veselov, Phys. Lett. **155B**, 217 (1985).
[65] P. LaFrance and E. L. Lomon, Phys. Rev. D **34**, 1341 (1986).
[66] Y. He, F. Wang, and C. W. Wong, Nucl. Phys. **A448**, 652 (1986); **A451**, 653 (1986); **A454**, 541 (1986).
[67] C. Fasano and T.-S.H. Lee, Phys. Rev. C **36**, 1906 (1987).
[68] X.-H. Yang, T.-S. Cheng, and Y.-S. Zhong, Phys. Rev. C **39**, 2036 (1989).
[69] Z.-J. Cao and L. S. Kisslinger, Phys. Rev. C **40**, 1722 (1989).
[70] J. Burger, R. Müller, K. Tragl, and H. M. Hofmann, Nucl. Phys. **A493**, 427 (1989).
[71] R. Vinh Mau, C. Semay, B. Loiseau, and M. Lacombe, Phys. Rev. Lett. **67**, 1392 (1991).
[72] F. Myhrer and J. Wroldsen, Rev. Mod. Phys. **60**, 629 (1988).
[73] L. D. Miller, Phys. Rev. Lett. **28**, 1281 (1972); Phys. Rev. C **14**, 706 (1976); L. D. Miller and A. E. S. Green, *ibid.* **5**, 241 (1972).
[74] R. Brockmann, Phys. Rev. C **18**, 1510 (1978).
[75] C. J. Horowitz and B. D. Serot, Nucl. Phys. **A368**, 503 (1981).
[76] J. D. Walecka, Ann. Phys. (N.Y.) **83**, 491 (1974).
[77] C. J. Horowitz and B. D. Serot, Phys. Lett. **109B**, 341 (1982); Nucl. Phys. **A399**, 529 (1983).
[78] M. R. Anastasio, L. S. Celenza, and C. M. Shakin, Phys. Rev. Lett. **45**, 2096 (1980); Phys. Rev. C **23**, 569 (1981); M. R. Anastasio, L. S. Celenza, W. S. Pong, and C. M. Shakin, Phys. Rep. **100**, 327 (1983).
[79] R. Brockmann and R. Machleidt, Phys. Lett. **149B**, 283 (1984).
[80] B. ter Haar and R. Malfliet, Phys. Rev. Lett. **56**, 1237 (1986).
[81] B. C. Clark, R. L. Mercer, D. G. Ravenhall, and A. M. Saperstein, Phys. Rev. C **7**, 466 (1973); L. G. Arnold, B. C. Clark, and R. L. Mercer, *ibid.* **19**, 917 (1979).
[82] A. M. Kobos, E. D. Cooper, J. I. Johansson, and H. S. Sherif, Nucl. Phys. **A445**, 605 (1985).
[83] J. A. McNeil, J. R. Shepard, and S. J. Wallace, Phys. Rev. Lett. **50**, 1439 (1983); J. R. Shepard, J. A. McNeil, and S. J. Wallace, *ibid.* **50**, 1443 (1983); J. A. McNeil, L. Ray, and S. J. Wallace, Phys. Rev. C **27**, 2123 (1983).
[84] B. C. Clark, S. Hama, R. L. Mercer, L. Ray, and B. D. Serot, Phys. Rev. Lett. **50**, 1644 (1983); B. C. Clark, S. Hama, R. L. Mercer, L. Ray, G. W. Hoffmann, and B. D. Serot, Phys. Rev. C **28**, 1421 (1983).
[85] M. V. Hynes, A. Picklesimer, P. C. Tandy, and R. M. Thaler, Phys. Rev. Lett. **52**, 978 (1984); Phys. Rev. C **31**, 1438 (1985).
[86] L. Ray and G. W. Hoffmann, Phys. Rev. C **31**, 538 (1985).
[87] M. Bawin and M. Jaminon, Nucl. Phys. **A407**, 515 (1983).
[88] E. Rost and J. R. Shepard, Phys. Rev. C **35**, 681 (1987), and references therein.
[89] E. D. Cooper, B. C. Clark, R. Kozack, S. Shim, S. Hama, J. I. Johansson, H. S. Sherif, R. L. Mercer, and B. D. Serot, Phys. Rev. C **36**, 2170 (1987).
[90] L. Ray, G. W. Hoffmann, M. L. Barlett, J. D. Lumpe, B.

C. Clark, S. Hama, and R. L. Mercer, Phys. Rev. C **37**, 1169 (1988); **39**, 2089(E) (1989).

[91] R. J. Glauber, in *Boulder Lectures in Theoretical Physics,* edited by L. G. Dunham and W. E. Brittin (Interscience, New York, 1959), p. 315.

[92] A. K. Kerman, H. McManus, and R. M. Thaler, Ann. Phys. (N.Y.) **8**, 551 (1959).

[93] W. G. Love and M. A. Franey, Phys. Rev. C **24**, 1073 (1981); M. A. Franey and W. G. Love, *ibid.* **31**, 488 (1985).

[94] J. A. Tjon and S. J. Wallace, Phys. Rev. Lett. **54**, 1357 (1985); Phys. Rev. C **32**, 267 (1985); **32**, 1667 (1985); **35**, 280 (1987); **36**, 1085 (1987); N. Ottenstein, S. J. Wallace, and J. A. Tjon, *ibid.* **38**, 2272 (1988); **38**, 2289 (1988).

[95] A. Picklesimer and P. C. Tandy, Phys. Rev. C **34**, 1860 (1986).

[96] S. J. Wallace, Annu. Rev. Nucl. Part. Sci. **37**, 267 (1987).

[97] T. Cheon and K. Takayanagi, Nucl. Phys. **A455**, 653 (1986).

[98] W. R. Coker and L. Ray, Phys. Rev. C **42**, 659 (1990).

[99] S. Shim, B. C. Clark, E. D. Cooper, S. Hama, R. L. Mercer, L. Ray, J. Raynal, and H. S. Sherif, Phys. Rev. C **42**, 1592 (1990).

[100] F. Gross, K. M. Maung, J. A. Tjon, L. W. Townsend, and S. J. Wallace, Phys. Rev. C **40**, R10 (1989).

[101] Th. Kirst, K. Amos, L. Berge, M. Coz, and H. V. von Geramb, Phys. Rev. C **40**, 912 (1989).

[102] M. F. Jiang, R. Machleidt, and T. T. S. Kuo, Phys. Rev. C **41**, 2346 (1990).

[103] C. Sorensen, Phys. Rev. D **19**, 1444 (1979).

[104] G. Alberi, M. Bleszynski, T. Jaroszewicz, and S. Santos, Phys. Rev. D **20**, 2437 (1979).

[105] W. Grein and P. Kroll, Nucl. Phys. **B157**, 529 (1979); W. Grein, A. König, and P. Kroll, Phys. Lett. **96B**, 176 (1980).

[106] I. P. Auer, W. R. Ditzler, D. Hill, H. Spinka, N. Tamura, G. Theodosiou, K. Toshioka, D. Underwood, R. Wagner, and A. Yokosawa, Phys. Rev. Lett. **46**, 1177 (1981).

[107] G. Alberi, M. Bleszynski, and T. Jaroszewicz, Ann. Phys. (N.Y.) **142**, 299 (1982).

[108] M. Haji-Saied, E. Bleszynski, M. Bleszynski, J. Carroll, G. J. Igo, T. Jaroszewicz, A. T. M. Wang, A. Sagle, J. B. McClelland, C. L. Morris, R. Klem, T. Joyce, Y. Makdisi, M. Marshak, B. Mossberg, E. A. Peterson, K. Ruddick, and J. Whittaker, Phys. Rev. C **36**, 2010 (1987).

[109] G. Igo, A. Masaike, B. Aas, D. Adams, G. Bleszynski, M. Bleszynski, M. Gazzaly, S. J. Greene, H. Hasai, S. Ishimoto, S. Isagawa, K. Jones, D. Lopiano, J. B. McClelland, F. Nishiyama, Y. Ohashi, A. Okihana, G. Pauletta, F. Sperisen, T.-H. Sun, N. Tanaka, G. S. Weston, and C. A. Whitten, Phys. Rev. C **38**, 2777 (1988).

[110] D. L. Adams, B. Aas, E. Bleszynski, M. Bleszynski, G. Igo, C. Newsom, Y. Ohashi, G. Pauletta, F. Sperisen, C. A. Whitten, H. Fujisawa, M. Gazzaly, S. J. Greene, K. Jones, J. B. McClelland, N. Tanaka, H. Hasai, K. Iwatani, S. Ishimoto, S. Isagawa, A. Masaike, A. Okihana, and S. Okumi, Nucl. Phys. **A480**, 530 (1988).

[111] V. Ghazikhanian, B. Aas, D. Adams, E. Bleszynski, M. Bleszynski, J. Bystricky, G. J. Igo, T. Jaroszewicz, F. Sperisen, C. A. Whitten, P. Chaumette, J. Deregel, J. Fabre, F. Lehar, A. deLesquen, L. van Rossum, J. Arvieux, J. Ball, A. Boudard, and F. Perrot, Phys. Rev. C **43**, 1532 (1991).

[112] See, for example, *Research Program at CEBAF (II), Report of the 1986 Summer Study Group* (CEBAF, Newport News, VA, 1987).

[113] J. R. Bergervoet, P. C. van Campen, R. A. M. Klomp, J.-L. de Kok, T. A. Rijken, V. G. J. Stoks, and J. J. de Swart, Phys. Rev. C **41**, 1435 (1990).

[114] M. Matsuda, in *Proceedings of the Workshop on the Experiments by KEK Polarized Proton and Electron Beams,* Ibaraki, Japan, 1988, edited by T. Hasegawa *et al.* (KEK, Japan, 1989), p. 181; M. Akemoto, M. Matsuda, H. Suemitsu, and M. Yonezawa, Prog. Theor. Phys. **67**, 554 (1982).

[115] H. Kanada and K. Sakai, in *Proceedings of the Workshop on the Experiments by KEK Polarized Proton and Electron Beams* [114], p. 195.

[116] O. G. Grebenyuk, E. N. Komarov, and G. M. Shklyarevskii, Yad. Fiz. **39**, 74 (1984) [Sov. J. Nucl. Phys. **39**, 44 (1984)]; V. G. Vovchenko, O. G. Grebenyuk, and O. Ya. Fedorov, *ibid.* **44**, 456 (1986) [**44**, 293 (1986)].

[117] I. P. Auer, E. Colton, D. Hill, K. Nield, B. Sandler, H. Spinka, Y. Watanabe, A. Yokosawa, and A. Beretvas, Phys. Lett. **67B**, 113 (1977).

[118] I. P. Auer, A. Beretvas, E. Colton, D. Hill, K. Nield, H. Spinka, D. Underwood, Y. Watanabe, and A. Yokosawa, Phys. Lett. **70B**, 475 (1977).

[119] H. Hidaka, A. Beretvas, K. Nield, H. Spinka, D. Underwood, Y. Watanabe, and A. Yokosawa, Phys. Lett. **70B**, 479 (1977).

[120] D. V. Bugg, in *High Energy Physics with Polarized Beams and Targets,* Proceedings of the Third International Symposium on High Energy Physics with Polarized Beams and Polarized Targets, Argonne, Illinois, 1978, edited by G. H. Thomas, AIP Conf. Proc. No. 51 (AIP, New York, 1979), p. 362.

[121] D. V. Bugg, J. Phys. G **5**, 1349 (1979).

[122] I. P. Auer, W. R. Ditzler, D. Hill, K. Imai, H. Spinka, R. Stanek, K. Toshioka, D. Underwood, R. Wagner, A. Yokosawa, E. W. Hoffman, J. J. Jarmer, G. R. Burleson, W. B. Cottingame, S. J. Greene, and S. Stuart, Phys. Rev. D **29**, 2435 (1984).

[123] E. Aprile-Giboni, J. Bystricky, J. Deregel, Ph. Drompt, C. Eisenegger, J. M. Fontaine, E. Heer, R. Hess, S. Jaccard, F. Lehar, W. R. Leo, S. Mango, S. Morenzoni, Y. Onel, F. Perrot, D. Rapid, J. Vrzal, and J. Yonnet, Nucl. Phys. **A431**, 637 (1984).

[124] J. Bystricky, P. Chaumette, J. Deregel, J. Fabre, F. Lehar, A. deLesquen, L. van Rossum, J. M. Fontaine, J. Gosset, F. Perrot, J. Ball, T. Hasegawa, C. R. Newsom, J. Yonnet, W. R. Leo, Y. Onel, A. Penzo H. Azaiez, and A. Michalowicz, Phys. Lett. **142B**, 130 (1984).

[125] J. Bystricky and F. Lehar, in *Proceedings of the Fourth International Symposium on Polarization Phenomena in Nuclear Reactions,* Zurich, Switzerland, 1975, edited by W. Gruebler and V. Koenig (Birkhauser-Verlag, Basel, 1976), p. 458.

[126] C. E. Waltham, R. Shypit, D. A. Axen, F. Entezami, M. Comyn, D. Healey, G. A. Ludgate, G. D. Wait, D. V. Bugg, J. A. Edgington, and N. R. Stevenson, Nucl. Phys. **A433**, 649 (1985).

[127] A. B. Wicklund, M. W. Arenton, D. S. Ayres, R. Diebold, E. N. May, L. J. Nodulman, J. R. Sauer, E. C. Swallow, M. M. Calkin, M. D. Corcoran, J. Hoftiezer, H. E. Miettinen, and G. S. Mutchler, Phys. Rev. D **35**, 2670 (1987).

[128] R. L. Shypit, D. V. Bugg, D. M. Lee, M. W. McNaughton, R. R. Silbar, N. M. Stewart, A. S. Clough, C. L. Hollas, K. H. McNaughton, P. Riley, and C. A. Davis, Phys. Rev. Lett. **60**, 901 (1988); **61**, 2385 (1988); R. L. Shypit, D. V.

Bugg, A. H. Sanjari, D. M. Lee, M. W. McNaughton, R. R. Silbar, C. L. Hollas, K. H. McNaughton, P. Riley, and C. A. Davis, Phys. Rev. C **40**, 2203 (1989).
[129] W. Grein and P. Kroll, Nucl. Phys. **B137**, 173 (1978).
[130] J.-L. Basdevant and E. L. Berger, Phys. Rev. D **19**, 239 (1979).
[131] M. H. MacGregor, Phys. Rev. D **20**, 1616 (1979).
[132] B. J. Edwards and G. H. Thomas, Phys. Rev. D **22**, 2772 (1980); B. J. Edwards, *ibid.* **23**, 1978 (1981).
[133] R. Bhandari, R. A. Arndt, L. D. Roper, and B. J. Ver West, Phys. Rev. Lett. **46**, 1111 (1981).
[134] S. Furuichi, K. Nakamura, and H. Suzuki, Prog. Theor. Phys. **67**, 547 (1982).
[135] W. Grein and P. Kroll, Nucl. Phys. **A377**, 505 (1982).
[136] I. I. Strakovskii, A. V. Kravtsov, and M. G. Ryskin, Yad. Fiz. **40**, 429 (1984) [Sov. J. Nucl. Phys. **40**, 273 (1984)]; I. I. Strakovsky, in *Proceedings of the Third International Symposium on Pion-Nucleon and Nucleon-Nucleon Physics,* Gatchina, U.S.S.R., 1989, edited by I. V. Lopatin and N. C. Morosova (Academy of Sciences of the U.S.S.R., Leningrad, 1989), p. 158.
[137] M. P. Locher *et al.*, in *Advances in Nuclear Physics,* edited by J. W. Negele and E. Vogt (Plenum, New York, 1986), Vol. 17, p. 47.
[138] N. Hoshizaki *et al.*, in *Proceedings of the Workshop on the Experiments by KEK Polarized Proton and Electron Beams* [114], p. 201; N. Hoshizaki, in *Proceedings of the VII International Symposium on High-Energy Spin Physics,* Protvino, U.S.S.R., 1986 (Institute of High Energy Physics, Serpukhov, 1987), Vol. 1, p. 177; N. Hoshizaki, Phys. Rev. C **45**, R1424 (1992).
[139] M. G. Ryskin and I. I. Strakovsky, Phys. Rev. Lett. **61**, 2384 (1988).
[140] T.-S. H. Lee, Phys. Rev. C **40**, 2911 (1989).
[141] N. Hiroshige *et al.*, Mod. Phys. Lett. A **5**, 207 (1990).
[142] T. Ueda, contribution to the 7th International Conference on Polarization Phenomena in Nuclear Physics, Paris, France, 1990 (unpublished).
[143] M. Beddo, G. Burleson, J. A. Faucett, S. Gardiner, G. Kyle, R. Garnett, D. P. Grosnick, D. Hill, K. F. Johnson, D. Lopiano, Y. Ohashi, T. Shima, H. Spinka, R. Stanek, D. Underwood, A. Yokosawa, G. Glass, R. Kenefick, S. Nath, L. Northcliffe, J. J. Jarmer, S. Pentillä, R. H. Jeppesen, G. Tripard, M. Devereux, and P. Kroll, Phys. Lett. B **258**, 24 (1991).
[144] F. Lehar, A. deLesquen, L. van Rossum, P. Chaumette, J. Deregel, J. Fabre, M. de Mali, J. M. Fontaine, D. Legrand, F. Perrot, J. Ball, C. D. Lac, P. Bach, G. Gaillard, R. Hess, Ph. Sormani, V. Ghazikhanian, C. A. Whitten, R. Peschina, and E. Rossle, Phys. Lett. B **189**, 241 (1987); J. M. Fontaine, F. Perrot-Kunne, J. Bystricky, F. Lehar, A. deLesquen, M. de Mali, L. van Rossum, J. Ball, Ph. Chesny, C. D. Lac, J. L. Sans, J. P. Goudour, P. Bach, G. Gaillard, R. Hess, R. Kunne, D. Rapin, Ph. Sormani, R. Binz, A. Klett, R. Peschina, E. Rossle, and H. Schmitt, Nucl. Phys. **B358**, 297 (1991).
[145] R. Binz, B. van den Brandt, R. Büchle, M. Daum, Ph. Demierre, J. Franz, G. Gaillard, N. Hamann, R. Hess, J. A. Konter, F. Lehar, C. Lechanoine-Leluc, S. Mango, R. Peschina, D. Rapin, E. Rössle, P. A. Schmelzbach, H. Schmitt, and R. Todenhagen, in *Proceedings of the Twelfth International Conference on Few Body Problems,* Vancouver, Canada, 1989, edited by H. W. Fearing [Nucl. Phys. **A508**, 267c (1990)].
[146] T. Kamae, I. Arai, T. Fujii, H. Ikeda, N. Kajiura, S. Kawabata, K. Nakamura, K. Ogawa, H. Takeda, and Y. Watase, Phys. Rev. Lett. **38**, 468 (1977); Nucl. Phys. **B139**, 394 (1978).
[147] T. Kamae and T. Fujita, Phys. Rev. Lett. **38**, 471 (1977).
[148] H. Ikeda, I. Arai, H. Fujii, T. Fujii, H. Iwasaki, N. Kajiura, T. Kamae, K. Nakamura, T. Sumiyoshi, H. Takeda, K. Ogawa, and M. Kanazawa, Phys. Rev. Lett. **42**, 1321 (1979).
[149] A. J. Hartzler and R. T. Siegel, Phys. Rev. **95**, 185 (1954); A. J. Hartzler, R. T. Siegel, and W. Opitz, *ibid.* **95**, 591 (1954).
[150] Yu. M. Kazarinov and Yu. N. Simonov, Zh. Eksp. Teor. Fiz. **31**, 169 (1956) [Sov. Phys. JETP **4**, 161 (1957)].
[151] N. S. Amaglobeli and Yu. M. Kazarinov, Zh. Eksp. Teor. Fiz. **33**, 53 (1958) [Sov. Phys. JETP **7**, 37 (1958)]; **37**, 1587 (1959) [**10**, 1125 (1960)].
[152] B. M. Golovin, V. P. Dzhelepov, Yu. V. Katyshev, A. D. Konin, and S. V. Medved, Zh. Eksp. Teor. Fiz. **36**, 735 (1959) [Sov. Phys. JETP **9**, 516 (1959)].
[153] R. R. Larson, Nuovo Cimento **18**, 1039 (1960).
[154] P. F. Shepard, T. J. Devlin, R. E. Mischke, and J. Solomon, Phys. Rev. D **10**, 2735 (1974).
[155] G. Bizard, F. Bonthonneau, J. L. Laville, F. Lefebvres, J. C. Malherbe, R. Regimbart, J. Duflo, and F. Plouin, Nucl. Phys. **B85**, 14 (1975).
[156] B. E. Bonner, J. E. Simmons, C. L. Hollas, C. R. Newsom, P. J. Riley, G. Glass, and M. Jain, Phys. Rev. Lett. **41**, 1200 (1978).
[157] R. Carlini, B. Dieterle, J. Donahue, C. Leavitt, T. Rupp, W. Thomas, D. Wolfe, L. B. Auerbach, V. L. Highland, K. F. Johnson, W. F. McFarlane, J. Pratt, and R. Bentley, Phys. Rev. Lett. **41**, 1341 (1978).
[158] W. Hürster, Th. Fischer, G. Hammel, K. Kern, M. Kleinschmidt, L. Lehmann, H. Schmitt, L. Schmitt, and D. M. Sheppard, Phys. Lett. **90B**, 367 (1980).
[159] M. L. Evans, G. Glass, J. C. Hiebert, M. Jain, R. A. Kenefick, L. C. Northcliffe, B. E. Bonner, J. E. Simmons, C. W. Bjork, P. J. Riley, H. C. Bryant, C. G. Cassapakis, B. Dieterle, C. P. Leavitt, D. M. Wolfe, and D. W. Werren, Phys. Rev. C **26**, 2525 (1982).
[160] R. K. Keeler, R. Dubois, E. G. Auld, D. A. Axen, M. Comyn, G. Ludgate, L. P. Robertson, J. R. Richardson, D. V. Bugg, J. A. Edgington, W. R. Gibson, A. S. Clough, N. M. Stewart, and B. Dieterle, Nucl. Phys. **A377**, 529 (1982).
[161] M. Jain, M. L. Evans, G. Glass, J. C. Hiebert, R. A. Kenefick, L. C. Northcliffe, B. E. Bonner, J. E. Simmons, C. W. Bjork, P. J. Riley, H. C. Bryant, C. G. Cassapakis, B. Dieterle, C. P. Leavitt, D. M. Wolfe, and D. W. Werren, Phys. Rev. C **30**, 566 (1984).
[162] Y. Terrien, J. C. Lugol, J. Saudinos, B. H. Silverman, F. Wellers, G. A. Korolev, A. V. Dobrovolsky, A. V. Khanzadeev, G. E. Petrov, E. M. Spiridenkov, and A. A. Vorobyov, Phys. Rev. Lett. **59**, 1534 (1987).
[163] P. R. Robrish, O. Chamberlain, R. D. Field, R. Z. Fuzesy, W. Gorn, C. C. Morehouse, T. Powell, S. Rock, S. Shannon, G. Shapiro, H. Weisberg, and M. J. Longo, Phys. Lett. **31B**, 617 (1970).
[164] A. S. Clough, D. R. Gibson, D. Axen, R. Dubois, L. Felawka, R. Keeler, G. A. Ludgate, C. J. Oram, C. Amsler, D. V. Bugg, J. A. Edgington, L. P. Robertson, N. M. Stewart, J. Beveridge, and J. R. Richardson, Phys. Rev. C **21**, 988 (1980).

[165] Yu. S. Bagaturiya, Yu. M. Kazarinov, M. Yu. Kazarinov, M. Yu. Liburg, V. N. Matafonov, G. G. Macharashvili, I. K. Potashnikova, I. Strakhota, M. Strakhotova, Yu. A. Usov, B. A. Khachaturov, and M. R. Khayatov, Yad. Fiz. **33**, 1237 (1981) [Sov. J. Nucl. Phys. **33**, 659 (1981)].

[166] R. D. Ransome, C. L. Hollas, P. J. Riley, B. E. Bonner, W. R. Gibbs, M. W. McNaughton, J. E. Simmons, T. S. Bhatia, G. Glass, J. C. Hiebert, L. C. Northcliffe, and W. B. Tippens, Phys. Rev. Lett. **48**, 781 (1982).

[167] G. A. Korolev, A. V. Khanzadeev, G. E. Petrov, E. M. Spiridenkov, A. A. Vorobyov, Y. Terrien, J. C. Lugol, J. Saudinos, B. H. Silverman, and F. Wellers, Phys. Lett. **165B**, 262 (1985).

[168] C. R. Newsom, C. L. Hollas, R. D. Ransome, P. J. Riley, B. E. Bonner, J. G. J. Boissevain, J. J. Jarmer, M. W. McNaughton, J .E. Simmons, T. S. Bhatia, G. Glass, J. C. Hiebert, L. C. Northcliffe, and W. B. Tippens, Phys. Rev. C **39**, 965 (1989).

[169] D. Bandyopadhyay, R. Abegg, M. Ahmad, J. Birchall, K. Chantziantoniou, C. A. Davis, N. E. Davison, P. P. J. Delheij, P. W. Green, L. G. Greeniaus, D. C. Healey, C. Lapointe, W. J. McDonald, C. A. Miller, G. A. Moss, S. A. Page, W. D. Ramsay, N. L. Rodning, G. Roy, W. T. H. van Oers, G. D. Wait, J. W. Watson, and Y. Ye, Phys. Rev. C **40**, 2684 (1989).

[170] G. Glass, T. S. Bhatia, J. C. Hiebert, R. A. Kenefick, S. Nath, L. C. Northcliffe, K. F. Johnson, H. Spinka, R. Stanek, M. W. Rawool, J. A. Faucett, R. H. Jeppesen, G. E. Tripard, and C. R. Newsom, Phys. Rev. C **41**, 2732 (1990).

[171] D. Axen, R. Dubois, R. Keeler, G. A. Ludgate, C. J. Oram, L. P. Robertson, N. M. Stewart, C. Amsler, D. V. Bugg, J. A. Edgington, W. R. Gibson, N. Wright, and A. S. Clough, Phys. Rev. C **21**, 998 (1980).

[172] J. Ball, C. D. Lac, F. Lehar, A. deLesquen, L. van Rossum, P. Chaumette, J. Deregel, J. Fabre, M. de Mali, J. M. Fontaine, F. Perrot, P. Bach, G. Gaillard, R. Hess, D. Rapin, Ph. Sormani, V. Ghazikhanian, C. A. Whitten, R. Peschina, and E. Rössle, Z. Phys. C **40**, 193 (1988).

[173] S. Nath, G. Glass, J. C. Hiebert, J. A. Holt, R. A. Kenefick, L. C. Northcliffe, D. P. Grosnick, D. Lopiano, Y. Ohashi, T. Shima, H. M. Spinka, R. Stanek, T. S. Bhatia, J. J. Jarmer, P. J. Riley, S. Sen, J. A. Faucett, G. Kyle, R. H. Jeppesen, and G. E. Tripard, Phys. Rev. D **39**, 3520 (1989).

[174] R. Garnett, M. Rawool, V. Carlson, D. Hill, K. F. Johnson, D. Lopiano, Y. Ohashi, T. Shima, H. Spinka, R. Stanek, D. Underwood, A. Yokosawa, M. Beddo, G. Burleson, J. A. Faucett, G. Kyle, H. Shimizu, G. Glass, S. Nath, L. C. Northcliffe, J. J. Jarmer, R. H. Jeppesen, and G. E. Tripard, Phys. Rev. D **40**, 1708 (1989).

[175] B. M. Golovin, V. P. Dzhelepov, V. S. Nadezhdin, and V. I. Satarov, Zh. Eksp. Teor. Fiz. **36**, 433 (1959) [Sov. Phys. JETP **9**, 302 (1959)].

[176] G. Martelli, H. B. van der Raay, R. Rubinstein, K. R. Chapman, J. D. Dowell, W. R. Fisken, B. Musgrave, and D. H. Reading, Nuovo Cimento **21**, 581 (1961).

[177] D. Cheng, B. MacDonald, J. A. Helland, and P. M. Ogden, Phys. Rev. **163**, 1470 (1967).

[178] Yu. M. Kazarinov, F. Lehar, A. F. Pisarev, and Z. Janout, Yad. Fiz. **5**, 140 (1967) [Sov. J. Nucl. Phys. **5**, 97 (1967)].

[179] S. C. Wright, D. Shawhan, L. Pondrom, S. Olsen, and R. Handler, Phys. Rev. **175**, 1704 (1968).

[180] L. M. C. Dutton and H. B. van der Raay, Phys. Rev. Lett. **21**, 1416 (1968).

[181] S. I. Bilenkaya, L. N. Glonti, Yu. M. Kazarinov, and V. S. Kiselev, Zh. Eksp. Teor. Fiz. **59**, 1049 (1970) [Sov. Phys. JETP **32**, 569 (1971)].

[182] L. N. Glonti, Yu. M. Kazarinov, and M. R. Khayatov, Zh. Eksp. Teor. Fiz. **62**, 1998 (1972) [Sov. Phys. JETP **35**, 1042 (1972)].

[183] R. Zulkarneev, Kh. Murtazaev, and V. Khachaturov, Phys. Lett. **61B**, 164 (1976).

[184] P. J. Riley, C. L. Hollas, C. R. Newsom, R. D. Ransome, B. E. Bonner, J. E. Simmons, T. S. Bhatia, G. Glass, J. C. Hiebert, L. C. Northcliffe, and W. B. Tippens, Phys. Lett. **103B**, 313 (1981).

[185] M. Sakuda, S. Isagawa, S. Ishimoto, S. Kabe, A. Masaike, K. Morimoto, K. Ogawa, M. Suetake, F. Takasaki, Y. Watase, N. Kim, S. Kobayashi, A. Murakami, A. deLesquen, K. Nakajima, S. Nakada, T. Wada, and I. Yamauchi, Phys. Rev. D **25**, 2004 (1982).

[186] T. S. Bhatia, G. Glass, J. C. Hiebert, L. C. Northcliffe, W. B. Tippens, B. E. Bonner, J. E. Simmons, C. L. Hollas, C. R. Newsom, P. J. Riley, and R. D. Ransome, Phys. Rev. Lett. **48**, 227 (1982).

[187] M. L. Barlett, G. W. Hoffmann, J. A. McGill, B. Hoistad, L. Ray, R. W. Fergerson E. C. Milner, J. A. Marshall, J. F. Amann, B. E. Bonner, J. B. McClelland, G. S. Blanpied, and R. A. Arndt, Phys. Rev. C **27**, 682 (1983).

[188] M. L. Barlett, G. W. Hoffmann, J. A. McGill, B. Hoistad, L. Ray, R. W. Fergerson, E. C. Milner, J. A. Marshall, J. F. Amann, B. E. Bonner, and J. B. McClelland, Phys. Rev. C **32**, 239 (1985).

[189] J. Bystricky, J. Deregel, F. Lehar, A. deLesquen, L. van Rossum, J. M. Fontaine, F. Perrot, J. Arvieux, T. Hasegawa, C. R. Newsom, Y. Onel, A. Penzo, H. Azaiez, A. Michalowicz, and C. Raymond, Nucl. Phys. **A444**, 597 (1985).

[190] J. S. Chalmers, W. R. Ditzler, T. Shima, H. Shimizu, H. Spinka, R. Stanek, D. Underwood, R. Wagner, A. Yokosawa, J. E. Simmons, G. Burleson, C. Fontenla, T. S. Bhatia, G. Glass, and L. C. Northcliffe, Phys. Lett. **153B**, 235 (1985).

[191] J. A. Marshall, M. L. Barlett, R. W. Fergerson, G. W. Hoffmann, E. C. Milner, L. Ray, J. F. Amann, B. E. Bonner, and J. B. McClelland, Phys. Rev. C **34**, 1433 (1986).

[192] J. Ball, V. Ghazikhanian, J. Gordon, F. Lehar, A. deLesquen, F. Perrot, and L. van Rossum, Nucl. Phys. **B286**, 635 (1987).

[193] R. Abegg, D. Bandyopadhyay, J. Birchall, C. A. Davis, N. E. Davison, P. W. Green, L. G. Greeniaus, C. Lapointe, C. A. Miller, G. A. Moss, S. A. Page, W. D. Ramsay, R. R. Tkachuk, and W. T. H. van Oers, Phys. Rev. C **38**, 2173 (1988).

[194] A. deLesquen, F. Lehar, L. van Rossum, P. Chaumette, J. Deregel, J. Fabre, J. M. Fontaine, F. Perrot, P. Bach, R. Hess, Ph. Sormani, J. Ball, C. D. Lac, D. Adams, J. Bystricky, V. Ghazikhanian, and C. A. Whitten, Nucl. Phys. **B304**, 673 (1988).

[195] M. L. Barlett, G. W. Hoffmann, L. Ray, G. Pauletta, K. H. McNaughton, J. F. Amann, K. W. Jones, J. B. McClelland, M. W. McNaughton, R. Fergerson, and D. Lopiano, Phys. Rev. C **40**, 2697 (1989).

[196] M. W. McNaughton, K. Koch, I. Supek, N. Tanaka, K. H. McNaughton, P. J. Riley, D. A. Ambrose, J. D. Johnson, A. Smith, G. Glass, J. C. Hiebert, L. C.

Northcliffe, A. J. Simon, D. L. Adams, R. D. Ransome, D. B. Clayton, H. M. Spinka, R. H. Jeppesen, and G. E. Tripard, Phys. Rev. C **44**, 2267 (1991); K. H. McNaughton, D. A. Ambrose, P. Coffey, K. Johnston, P. J. Riley, M. W. McNaughton, K. Koch, I. Supek, N. Tanaka, G. Glass, J. C. Hiebert, L. C. Northcliffe, A. J. Simon, D. J. Mercer, D. L. Adams, H. Spinka, R. H. Jeppesen, G. E. Tripard, and H. Woolverton, Phys. Rev. C **46**, 47 (1992); M. W. McNaughton, K. Koch, I. Supek, N. Tanaka, D. A. Ambrose, P. Coffey, K. Johnston, K. H. McNaughton, P. J. Riley, G. Glass, J. C. Hiebert, L. C. Northcliffe, A. J. Simon, D. J. Mercer, D. L. Adams, H. Spinka, R. H. Jeppesen, G. E. Tripard, and H. Woolverton, *ibid.* **45**, 2564 (1992).

[197] *Proceedings of the International Symposium on Polarization Phenomena of Nucleons,* edited by P. Huber and K. P. Meyer [Helv. Phys. Acta, Suppl. VI, 436 (1961)].

[198] G. R. Burleson, J. A. Faucett, C. A. Fontenla, R. W. Garnett, M. W. Rawool, W. R. Ditzler, D. Hill, J. Hoftiezer, K. F. Johnson, D. Lopiano, T. Shima, H. Shimizu, H. Spinka, R. Stanek, D. Underwood, R. Wagner, A. Yokosawa, T. S. Bhatia, G. Glass, J. C. Hiebert, R. A. Kenefick, S. Nath, L. C. Northcliffe, R. Damjanovich, J. J. Jarmer, R. H. Jeppesen, and G. E. Tripard, Phys. Rev. Lett. **59**, 1645 (1987).

[199] M. Rawool, thesis, New Mexico State University, 1988; Los Alamos National Laboratory Report No. LA-11387-T, 1988 (unpublished).

[200] C. W. Bjork, P. J. Riley, B. E. Bonner, J. E. Simmons, K. D. Williamson, M. L. Evans, G. Glass, J. C. Hiebert, M. Jain, R. A. Kenefick, L. C. Northcliffe, C. G. Cassapakis, H. C. Bryant, B. D. Dieterle, C. P. Leavitt, D. M. Wolfe, and D. W. Werren, Phys. Lett. **63B**, 31 (1976).

[201] C. W. Bjork, thesis, University of Texas at Austin, 1975; Los Alamos National Laboratory Report No. LA-6192-T (unpublished).

[202] M. W. McNaughton and E. P. Chamberlin, Phys. Rev. C **24**, 1778 (1981).

[203] M. W. McNaughton, P. R. Bevington, H. B. Willard, E. Winkelmann, E. P. Chamberlin, F. H. Cverna, N. S. P. King, and H. Willmes, Phys. Rev. C **23**, 1128 (1981).

[204] M. W. McNaughton, Los Alamos National Laboratory Report No. LA-8307-MS, 1980 (unpublished).

[205] M. W. McNaughton (private communication).

[206] C. L. Hollas, R. D. Ransome, P. J. Riley, B. E. Bonner, J. G. Boissevain, T. S. Bhatia, G. Glass, J. C. Hiebert, and W. B. Tippens, Nucl. Instrum. Methods Phys. Res. A **219**, 275 (1984).

[207] H. Spinka, Argonne National Laboratory Report No. ANL-HEP-TR-88-14, 1988 (unpublished).

[208] O. B. van Dyck (private communication).

[209] A. Abragam and M. Goldman, *Nuclear Magnetism: Order and Disorder* (Clarendon, Oxford, 1982); Rep. Prog. Phys. **41**, 395 (1978).

[210] P. Autones, J. C. Brisson, A. Boucherie, G. Cozzika, J. Deregel, J. P. Duthil, H. Desportes, Y. Ducros, A. Katz, A. deLesquen, J. P. Merlo, J. F. Mougel, J. Movchet, J. C. Raoul, B. Tsai, L. van Rossum, B. Amblard, J. M. Fontaine, M. Hansroul, and J. M. Rieubland, Nucl. Instrum. Methods **103**, 211 (1972).

[211] J. C. Raoul, P. Autones, R. Auzolle, C. Bruneton, J. Bystricky, G. Cozzika, J. Deregel, Y. Ducros, A. Gaidot, A. Katz, F. Khantine-Langlois, F. Lehar, A. deLesquen, J. P. Merlo, S. Miyashita, J. Movchet, J. Pierrard, M. Ramadier, P. Roubeau, G. Souchere, L. van Rossum, A. A. Derevschikov, N. I. Golovnya, Yu. S. Khoderev, Yu. A. Matulenko, A. P. Meschanin, S. B. Nurushev, A. I. Saraykin, V. S. Seleznev, V. V. Siskin, E. V. Smirnov, V. L. Solovyanov, V. N. Zapolsky, Yu. M. Kazarinov, M. Yu. Kazarinov, B. A. Khatchaturov, I. K. Potashnikova, and V. P. Kanavets, Nucl. Instrum. Methods **125**, 585 (1975).

[212] I. P. Auer, E. Colton, W. R. Ditzler, H. Halpern, D. Hill, H. Spinka, N. Tamura, J.-J. Tavernier, G. Theodosiou, K. Toshioka, D. Underwood, R. Wagner, Y. Watanabe, and A. Yokosawa, Phys. Rev. D **34**, 1 (1986).

[213] G. Court, Rutherford and Appleton Laboratories Report No. RL-80-080, 1980 (unpublished), p. 76.

[214] C. L. Morris, H. A. Thiessen, and G. W. Hoffmann, IEEE Trans. Nucl. Sci. **NS-25**, 141 (1978); L. G. Atencio, J. F. Amann, R. L. Boudrie, and C. L. Morris, Nucl. Instrum. Methods **187**, 381 (1981); C. L. Morris, *ibid.* **196**, 263 (1982).

[215] I. P. Auer, D. Bridges, T. Droege, D. Hill, R. Giese, R. Miller, K. Nield, P. Rynes, B. Sandler, A. Yokosawa, G. Hicks, D. Miller, and C. Wilson, Phys. Rev. D **24**, 1771 (1981).

[216] W. Haberichter and H. Spinka, Lawrence Berkeley Laboratory Report LBL-21170, 1986 (unpublished), p. 99.

[217] K. Nield and R. Daly, Argonne National Laboratory Report No. ANL-HEP-PR-77-32, 1977 (unpublished).

[218] R. Yamada, J. Dinkel, R. J. Wojslaw, and C. D. Buchanan, Nucl. Instrum. Methods **138**, 567 (1976).

[219] R. W. Garnett and G. R. Burlseon, Nucl. Instrum. Methods A **313**, 501 (1992); R. W. Garnett, thesis, New Mexico State University, 1988; Los Alamos National Laboratory Report No. LA-11491-T, 1989 (unpublished).

[220] W. Haberichter, T. Kasprzyk, H. Shimizu, H. Spinka, R. Stanek, G. Burleson, R. Garnett, and J. Tobin, Nucl. Instrum. Methods Phys. Res. A **270**, 361 (1988).

[221] G. E. Theodosiou, and J. W. Dawson, Nucl. Instrum. Methods **172**, 491 (1980).

[222] L. R. Biswell and R. E. Rajala, Los Alamos National Laboratory Report No. LA-4916-MS, 1972 (unpublished).

[223] J. F. Harrison, T. Kozlowski, R. A. Floyd, J. F. Amann, G. T. Anderson, M. A. Oothoudt, and D. G. Perry, IEEE Trans. Nucl. Sci. **NS-28**, 3724 (1981); D. G. Perry, *ibid.* **NS-26**, 4494 (1979); M. Kellogg, M. M. Minor, S. Shlaer, N. Spencer, R. F. Thomas, and H. van der Beken, Los Alamos National Laboratory Report LA-7001-M, 1978 (unpublished).

[224] H.Spinka, Phys. Rev. D **30**, 1461 (1984).

[225] T. S. Bhatia, G. Glass, J. C. Hiebert, L. C. Northcliffe, W. B. Tippens, B. E. Bonner, J. E. Simmons, C. L. Hollas, C. R. Newsom, R. D. Ransome, and P. J. Riley, in *Polarization Phenomena in Nuclear Physics—1980,* Proceedings of the Fifth International Symposium on Polarization Phenomena in Nuclear Physics, Sante Fe, New Mexico, edited by G. G. Ohlson, R. E. Brown, N. Jarmie, M. W. McNaughton, and G. M. Hale, AIP Conf. Proc. No. 69 (AIP, New York, 1981), p. 123.

[226] B. M. Golovin, V. P. Dzhelepov, and R. Ya. Zulkarneev, Zh. Eksp. Teor. Fiz. **41**, 83 (1961) [Sov. Phys. JETP **14**, 63 (1962)].

[227] D. Besset, Q. H. Do, B. Favier, R. Hausammann, E. Heer, R. Hess, C. Lechanoine-Leluc, W. R. Leo, D. Rapin, D. W. Werren, Ch. Weddigen, J. M. Cameron, S. Jaccard, and S. Mango, Nucl. Phys. **A345**, 435 (1980).

[228] D. A. Bell, J. A. Buchanan, M. M. Calkin, J. M. Clement,

W. H. Dragoset, M. Furic, K. A. Johns, J. D. Lesikar, H. E. Miettinen, T. A. Mulera, G. S. Mutchler, G. C. Phillips, J. B. Roberts, and S. E. Turpin, Phys. Lett. **94B**, 310 (1980).

[229] M. W. McNaughton, H. W. Baer, P. R. Bevington, F. H. Cverna, H. B. Willard, E. Winkelmann, E. P. Chamberlin, J. J. Jarmer, N.S. P. King, J. E. Simmons, M. A. Schardt, and H. Willmes, Phys. Rev. C **23**, 838 (1981).

[230] N. S. Borisov, V. G. Vovchenko, V. A. Efimovykh, A. A. Zhdanov, M. Yu. Kazarinov, Yu. M. Kazarinov, Yu. F. Kiselev, A. I. Kovalev, M. Yu. Liburg, B. S. Neganov, V. V. Polyakov, V. E. Popov, A. N. Prokofev, V. Yu. Trautman, Yu. A. Usov, and A. V. Shvedchikov, Zh. Eksp. Teor. Fiz. **81**, 1583 (1981) [Sov. Phys. JETP **54**, 841 (1981)].

[231] M. W. McNaughton, E. P. Chamberlin, J. J. Jarmer, N. S. P. King, H. B. Willard, and E. Winkelman, Phys. Rev. C **25**, 2107 (1982).

[232] T. S. Bhatia, G. Glass, J. C. Hiebert, R. A. Kenefick, L. C. Northcliffe, W. B. Tippens, J. G. J. Boissevain, J. J. Jarmer, J. E. Simmons, G. E. Tripard, D. Fitzgerald, J. Holt, and A. Mokhtari, Phys. Rev. Lett. **49**, 1135 (1982).

[233] I. P. Auer, A. Beretvas, E. Colton, H. Halpern, D. Hill, K. Nield, B. Sandler, H. Spinka, G. Theodosiou, D. Underwood, Y. Watanabe, and A. Yokosawa, Phys. Rev. Lett. **41**, 1436 (1978).

[234] E. Aprile, R. Hausammann, E. Heer, R. Hess, C. Lechanoine-Leluc, W. R. Leo, S. Morenzoni, Y. Onel, D. Rapin, and S. Mango, Phys. Rev. D **28**, 21 (1983).

[235] J. Bystricky, P. Chaumette, J. Deregel, J. Fabre, F. Lehar, A. deLesquen, L. van Rossum, J. M. Fontaine, F. Perrot, J. Ball, T. Hasegawa, C. R. Newsom, A. Penzo, Y. Onel, H. Azaiez, and A. Michalowicz, Nucl. Phys. **B258**, 483 (1985).

[236] M. G. Meshcheryakov, B. S. Neganov, L. M. Soroko, and I. K. Vzorov, Dokl. Akad. Nauk. SSSR **99**, 959 (1954).

[237] V. M. Guzhavin, G. K. Kliger, V. Z. Kolganov, A. V. Lebedev, K. S. Marish, M. A. Musin, Yu. D. Prokoshkin, V. T. Smolyankin, A. P. Sokolov, L. M. Soroko, and Ts'ui Wa-Ch'uang, Zh. Eksp. Teor. Fiz. **47**, 1228 (1964) [Sov. Phys. JETP **20**, 830 (1965)].

[238] M. G. Albrow, S. Andersson/Almehed, B. Bosnjakovic, C. Daum, F. C. Erne, J. P. Lagnaux, J. C. Sens, and F. Udo, Nucl. Phys. **B23**, 445 (1970).

[239] B. A. Ryan, A. Kanofsky, T. J. Devlin, R. E. Mischke, and P. F. Shepard, Phys. Rev. D **3**, 1 (1971).

[240] D. T. Williams, I. J. Bloodworth, E. Eisenhandler, W. R. Gibson, P. I. P. Kalmus, L. C. Y. Lee Chi Kwong, G. T. J. Arnison, A. Astbury, S. Gjesdal, E. Lillethun, B. Stave, O. Ullaland, and I. L. Watkins, Nuovo Cimento A **8**, 447 (1972).

[241] K. Abe, B. A. Barnett, J. H. Goldman, A. T. Laasanen, P. H. Steinberg, G. J. Marmer, D. R. Moffett, and E. F. Parker, Phys. Rev. D **12**, 1 (1975).

[242] H. B. Willard, B. D. Anderson, H. W. Baer, R. J. Barrett, P. R. Bevington, A. N. Anderson, H. Willmes, and N. Jarmie, Phys. Rev. C **14**, 1545 (1976).

[243] M. Garcon, D. Legrand, R. M. Lombard, B. Mayer, M. Rouger, Y. Terrien, and A. Nakach, Nucl. Phys. **A445**, 669 (1985).

[244] G. W. Hoffmann, M. L. Barlett, R. W. Fergerson, J. A. Marshall, J. A. McGill, E. C. Milner, L. Ray, and J. F. Amann, Phys. Rev. C **37**, 397 (1988).

[245] D. V. Bugg and C. Wilkin, Nucl. Phys. **A467**, 575 (1987).

[246] D. V. Bugg, Phys. Rev. C **41**, 2708 (1990).

[247] Y. Higuchi, N. Hoshizaki, H. Masuda, and H. Nakao, Prog. Theor. Phys. **86**, 17 (1991); N. Hoshizaki and T. Watanabe, *ibid.* **86**, 321 (1991); **86**, 327 (1991).

[248] T. S. H. Lee (private communication).

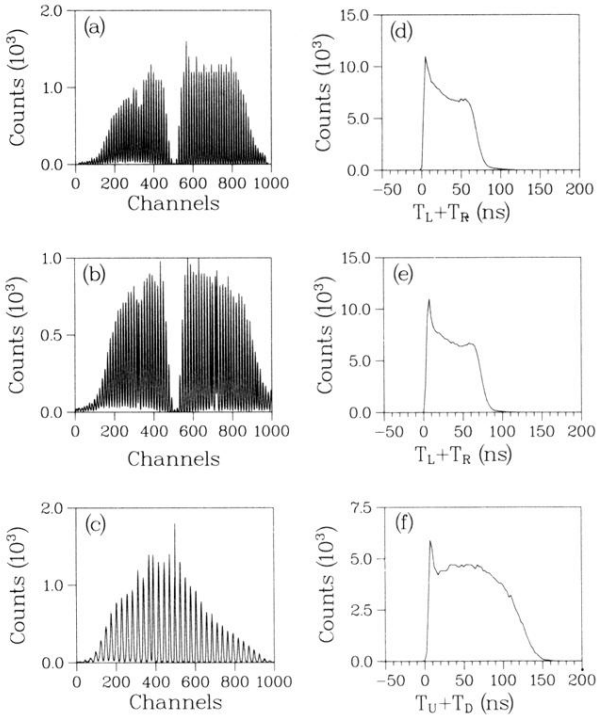

FIG. 9. Histograms of the (a)–(c) time differences and (d)–(f) sums from the delay-line ends of the X, X', and Y planes of P_1, respectively. The time differences were related to the wire number and the sums to drift time using look-up tables.